5-2019

Plasmonic Properties of Nanoparticle and Two Dimensional Material Integrated Structure

Desalegn Tadesse Debu
University of Arkansas, Fayetteville

Follow this and additional works at: https://scholarworks.uark.edu/etd

Part of the Nanoscience and Nanotechnology Commons, Nanotechnology Fabrication Commons, Optics Commons, and the Semiconductor and Optical Materials Commons

Plasmonic Properties of Nanoparticle and Two Dimensional Material Integrated Structure

A dissertation submitted in partial fulfillment
of the requirements for the degree of
Doctor of Philosophy in Physics

by

Desalegn Tadesse Debu
Dilla University
Bachelor of Science in Physics, 2004
Addis Ababa University
Master of Science in Physics, 2006

May 2019
University of Arkansas

This dissertation is approved for recommendation to the Graduate Council.

_____
Joseph B. Herzog, PhD
Dissertation Director

_____
Surendra P. Singh, PhD
Committee Member

_____
Salvador Barraza-Lopez, PhD
Committee Member

Abstract

Recently, various groups have demonstrated nano-scale engineering of nanostructures for optical to infrared wavelength plasmonic applications. Most fabrication technique processes, especially those using noble metals, requires an adhesion layer. Previously proposed theoretical work to support experimental measurement often neglect the effect of the adhesion layers. The first finding of this work focuses on the impact of the adhesion layer on nanoparticle plasmonic properties. Gold nanodisks with a titanium adhesion layer are investigated by calculating the scattering, absorption, and extinction cross-section with numerical simulations using a finite difference time domain (FDTD) method. I demonstrate that a gold nanodisk with an adhesive layer significantly shifts the plasmon resonance relative to one without adhesion material. In addition, the adhesive layer also introduces stronger damping and decay time. Next, I investigate the plasmonic properties and effects of dielectric environment of black phosphorene (BP), a newly discovered anisotropic 2D material. Results suggest that the surface plasmon properties of a black phosphorene nanoribbon could be exploited to probe the efficiency of edge plasmonic enhanced absorption. Furthermore, the enhanced absorption of periodic BP nanoribbons is affected strongly by high density free carriers in BP nanoribbon geometries from mid-infrared to high infrared regime. Also when adding a thin dielectric shielding layer, such as hexagonal boron nitride, in addition to preserving the edge mode plasmonic nature of BP, it also allows for an unprecedented control of the absorption resonance energy. Finally, I also show monolayer graphene surface plasmon hybridization with hyperbolic phonon polarization local density of state of hyperbolic ferroelectric $LiNbO_3$. The results show that the dispersion mode hybridization process is significantly regulated by a electrostatic gated single graphene and double graphene layer in addition to the ferroelectric layer size. The spontaneous emission (SE) rate the hyperbolic band contribution of $LiNbO_3$ with

graphene integrated system elucidated enhancement and inhibit spontaneous emission. Specially, the SE rate between in hybrid system is always smaller than that of the bulk in the hyperbolic band region with higher chemical potential.

Acknowledgment

First, I gratefully thank my adviser Dr. Joseph B. Herzog for all his support and work on an exciting field and accomplish this project. I would like to thank all of my committee members for dedicating their time and significant suggestions forwarded during annual review period These has helped me to look things in many possible directions and improve my research.

I would like to acknowledge Dr. Pradeep Kumar for a great number of ideas and insightful comments which improved of my research and understanding of physics.

I would also like to acknowledge my current and former lab group members, Pijush K. Gosh, Ahmad Darweesh, Stephen J. Bauman, David French, Zach Brawley and Faezeh Tork Ladani, for through discussions and many fruitful collaborations works. I would like to thank other collaborators outside the lab group, specially I want to thank Dr. Mourad Benamara and Mr. Qigeng Yan for their professional training of the nanofabrication and measurement tools.

I would like to thank all my friends at UARK; Sudip, Hemline, Harpreet, Bala, Venikat, Amanda and Doha beside sharing office with some of you and study together but also for all the good times outside work. Special thanks to Kendall making much of my time more enjoyable.

Also, I would like to thank Physics Department at the University of Arkansas for giving me the opportunity to pursue a doctoral degree and providing financial funding.

Finally, I would like to thank my family; Kidist, Ghion, the best dad Tadesse and amazing brother Abdissa, for all the love and help.

Table of contents

CHAPTER 5

List of publications

Chapter 3
D. T. Debu, P. Ghosh, D. French, and J. B. Herzog, "Surface plasmon damping effects due to Ti adhesion layer in individual gold nanodisks", Optical Materials Express, 7(1), 73-84 (2016).

Chapter 4
D. T. Debu, S. J. Bauman, D. French, Hugh O. H. Churchill, J. B. Herzog, "Tuning Infrared Plasmon Resonance of Black Phosphorene Nanoribbon with a Dielectric Interface", Scientific Reports 8(1), 3224 (2018).

Chapter 5
D. T. Debu, Faezeh Tork Ladani, David French Stephen J. Bauman and Joseph B. Herzog, "Hyperbolic plasmon-phonon dispersion for tunable spontaneous emission graphene-modulated ferroelectric substrates" (under review)

Chapter 1

Introduction

Since the past few decades, studies of plasmonics has become one of the most important flourishing optical-science in light matter interactions in both the classical and quantum fields [1]. Plasmon are quantized modes of collectively excited charge density oscillations typically occurring in charged electron gases in solids in the presence of long range coulomb interactions [2]. Commonly, the study of plasmons is attributed with the excitation of resonant oscillations of charges using light and/or beam of electrons in metallic materials [3]. Most recently, with the discovery of new materials and detection mechanisms plasmon phenomena study has expanded into heavily doped semiconductors and semimetals. Depending on the quantized oscillation behavior of charges, plasmons process have two classifications of electromagnetic (EM) field properties [4,5]. In the first case, when external electric fields of the electromagnetic radiation shined on a metallic surface and a dielectric caused polarization by displacing electrons from the equilibrium position to the excited mode around positively charged ions. The excited electrons behave as a free electron gas. The interaction between the excited electrons produces surface waves confined to the metal-dielectric interfaces. The bounded surface waves are vibrating with a well-defined frequency and propagate perpendicular to the propagation vector. These types of oscillations are called propagating surface plasmon polaritons (PSPPs) [4,5].

Contrary to propagating surface plasmon polaritons (PSPPs), when metallic material structures scaled to a few nanometers and or few micrometers curved geometries, the external light creates a free electron cloud of conduction electrons. Due to the curvature of the metallic structure, the particle of the metal induces a balancing force on the electron cloud. The electrons in such cases undergo damped harmonics oscillation. The mode of vibration is resonant in nature and is confined

within nanostructures into sub-wavelength volumes braking the diffraction limit of light. Hence, referred to as localized surface plasmon resonances (LSPRs) [5]. At the resonance frequency, the amplitude of the electric field of the oscillating charges will be much larger than away from the resonance point. Moreover, the strength of the electric field local localized near the surface of the nanostructure is highly enhanced and can be several orders of magnitude higher than that of the incident field [6]. The enhanced field strength rapidly falls off with distance from the surface of the material decay. In LSPRs' mode the resonant frequency and the confined EM field depend on the composition of the material, shape and size [7]. In addition, confined plasmon EM waves can be more localized EM fields and further enhanced by bringing two (dimer) nanostructure or ensemble of nanoparticles, within extremely small gaps (> 0.5 nm) [8, 9]. The strong enhancement EM field is due to constructive interference between the dipole or higher moments charge oscillation on neighboring nanoparticles. Moreover, dielectric environments, especially metallic adhesion layers, contributes a unique role in properties of plasmon, and has been studied in this thesis.

In the past, decayed, experimental fabrications method such as e-beam lithography and measurement using dark field microscopy elaborated noble metals plasmon. Despite immense progress, noble metal films and nanostructures plasmonic nature experience large losses due to small carrier mobilities, and very low dynamic tunability. These characteristics limited their plasmonics application in optical and near infrared electromagnetic spectrum. Such limitations have led to the search for other better plasmonic materials [10, 11], transition metal nitrides, hyperbolic natural and artificial materials, and 2D materials, mainly graphene [12], doped transition metal dichalcogenides [13], and most recently black phosphorus (BP) [14]. Both SPPs

and LSPPS generated in these materials feature low-loss, extremely sub-wavelength confined and longer propagation length. The plasmon electromagnetic produced can be dynamically tuned by chemical potential affecting the charge density and by the number of atomic layers.

Besides light and electron beam, another most exciting merit of plasmons property is the ability of highly strong light-matter interactions with quantum emitters such as a molecule (dots) to generate LSPs and confined surface plasmon polaritons (SPPs) through a near field interaction. Emission process of radiation due to local density of states of plasmonic modes is explained by Purcell factor also referred to as spontaneous emission (SE) rate [15,16]. According to the Purcell factor, the SE rate can be an efficiently controlled system providing a strongly confined mode and higher density of mode. In such context, material that supports strong confinement of surface plasmon polaritons and/or hyperbolic materials that support phonon polaritonic modes ensures efficient coupling at a given electromagnetic scale [17,18]. Hybrid surface plasmon phonon modes are coupled modes of two or more structure with plasmonic modes orignated in one material and phononic modes in the other. Controlling the hybrid electromagnetic waves bring an extra degree of freedom and might be used for new applications that couldn't be attained by ordinary metamaterials. Hence, there is a great deal of interest to modulate efficiency of the SE rate enhancement of quantum emitters. This is essential in a class of material whose optical properties can be regulated in a mid-infrared and terahertz (THz) range minimizing loss effect. In this thesis, I use a novel strategy in order to actively control SE rate in THz 2D graphene and hyperbolic layer hybrid systems without altering the geometrical surroundings.

This dissertation is divided into six chapters.

Chapter two gives an introduction of the theoretical background and concepts for understanding the Fresnel equation between polaritonics and plasmon supporting 2D material, including surface plasmon polaritons (SPPs), confined surface plasmons hyperbolic metamaterial dispersion, and point dipole spontaneous emission. Chapter three covers the finite element methods for computing adhesive integrated gold nanodisk of various sizes, ranging from 80 nm - 200 nm in diameter. The result is that FEM is extended to calculate the confined surface plasmon damping and decaying properties has also been introduced. Chapter four discusses surface plasmon properties of newly discovered 2D anisotropic black phosphorene, and absorption properties of periodic nanoribbon enhanced BP and dielectric protected BP ribbon by defining the optical conductivity from the Drude model. The underlying physical mechanisms that enhance the absorption of BP ribbon in different directions of nanoribbons has been extensively addressed. In Chapter five, mechanisms of surface plasmon and hyperbolic photon polariton hybridization in lower terahertz range is studied. The numerical result of SE rate due to a point using a graphene 2D conducting sheet with hyperbolic material is discussed. The SE rate in between hybrid systems which can give a roadmap for designing of modulated emission in THz spectral. Finally, chapter six presents the overall conclusions of this thesis work and proposes potential research directions in continuation of this work.

Reference

[1] S. I. Bozhevolnyi and N. A. Mortensen. Plasmonics for emerging quantum technologies. Nanophotonics, 6:1185–1188, January 2017.

[2] 2. Maier, S. A. Plasmonics: Fundamentals and Applications; Springer Science+Business Media LLC: New York, 2007.

[3] F. J. G. de Abajo, "Optical excitations in electron microscopy," Rev. Mod. Phys. 82, 209 (2010).

[4] Raether, H. Surface Plasmons (ed. Hohlere, G.) (Springer, Berlin, 1988).

[5] U. Kreibig, M. Vollmer, Optical Properties of Metal Clusters, Springer-Verlag, Berlin, Germany 1995.

[6] C. Saylor, E. C. Novak, D. T. Debu, and J. B. Herzog, "Investigation of maximum optical enhancement in single gold nanowires and triple nanowire arrays", Journal of Nanophotonics, 9(1), 093053 (2015).

[7] P. K. Ghosh, D. T. Debu, D. A. French, J. B. Herzog, "Calculated thickness dependent plasmonic properties of gold nanobars in the visible to near-infrared light regime", PLOS ONE 12(5), e0177463 (2017).

[8] S. J. Bauman, E. C. Novak, D. T. Debu, D. Natelson, and J. B. Herzog, "Fabrication of sub-lithography-limited structures via Nanomasking technique for plasmonic enhancement applications", IEEE Trans Nanotechnol **14** 5 (2015).

[9] Savage, K. J.; Hawkeye, M. M.; Esteban, R.; Borisov, A. G.; Aizpurua, J.; Baumberg, J. J. Revealing the Quantum Regime in Tunnelling Plasmonics Nature 2012, 491, 574– 577.

[10] Mark I. Stockman, "Nanoplasmonics: past, present, and glimpse into future," Opt. Express 19, 22029-22106 (2011)

[11] Naik, G. V.; Shalaev, V. M.; Boltasseva, A. Alternative Plasmonic Materials: Beyond Gold and Silver Adv. Mater. 2013, 25, 3264– 3294

[12] Jablan, M.; Buljan, H.; Soljacic, M. Plasmonics in graphene at infrared frequencies Phys. Rev. B 2009, 80, 245435

[13] Tabert C J and Nicol E J 2014 Dynamical polarization function, plasmons, and screening in silicene and other buckled honeycomb lattices Phys. Rev. B 89 195410

[14] T. Low, A. S.Rodin, A. Carvalho, Y. Jiang, H. Wang, F. Xia, and A. H. Castro Neto, Tunable optical properties of multilayers black phosphorus, Phys. Rev. B 90, 075434 (2014).

[15] Purcell, E. M. Spontaneous Emission Probabilities at Radio Frequencies. Phys. Rev. 69, 674– 702 (1946)

[16] M. Fox, Quantum Optics: An Introduction (Oxford Univ. Press, 2006)

[17] Xia, F., Wang, H., Xiao, D., Dubey, M. & Ramasubramaniam, A. Two-dimensional material nanophotonics. Nature Photon. 8, 899–907 (2014).

[18] Brar, V. W. et al. Hybrid surface-phonon-plasmon polariton modes in graphene/monolayer h-BN heterostructures. Nano Lett. **14**, 3876–3880 (2014).

Chapter 2

This chapter establishes the theoretical foundation required to analyze the electromagnetic interaction near a planar interface of planar interface of two and more layers. Maxwell's equations, and the electromagnetic boundary conditions needed to analyze the field produced in different layers are defined. The differential Maxwell's equation eigen solution are set based on interfaces two of uniaxial layers. The dispersion modes of the uniaxial layer explained form the momentum vector complex solutions. We derive the formulas for calculating the Fresnel coefficients between two anisotropic interface and isotropic conducting sheet in between. This was also expanded in multilayer system following transfer matrix approach and summed up for absorption, reflection and transmission value. In the subsequent section quantum dipole emitter radiation source, treated a classical electromagnetic phenomenon is addressed for a system consists of 2D material. First, the dyadic Green's tensor for the electric field is derived in Cartesian coordinate for each interface two-layered planar interface and anisotropic 2D material. This is followed by the calculation of an integral form the EM field for the possibility of controlling the SE rate of 2D layer conducting sheet driven by a point dipole radiation source. The introduced theoretical model of SE rate is finally summarized for dipole emitter polarization-dependent excitation.

2.1 Theoretical Formulation

In this subsection we present a unified theoretical perspective of practical approaches to achieve light mater interaction and response properties nanoparticles, semi-infinite buck medium and 2D materials. We first consider the nature of light across an interface formed between a 2D sheet a two semi-infinite uniaxial dielectrics medium, with dielectric permittivity of $\tilde{\varepsilon}_1$ and $\tilde{\varepsilon}_2$, as shown schematically in figure 2.1a and 2.1b. We regard 2D material (such as graphene, black

phosphorene) thickness of few atomic layers commonly is less than 1nm. In order to understand the interaction of light in such system we implement the Maxwell's EM equations [1] given as

$$\nabla \cdot \vec{D} = \rho_f \tag{2.1.a}$$

$$\nabla \cdot \vec{B} = 0 \tag{2.1.b}$$

$$\nabla \times \vec{E} = -\frac{\partial \vec{B}}{\partial t} \tag{2.1.c}$$

$$\nabla \times \vec{H} = \vec{J}_f + \frac{\partial \vec{D}}{\partial t} \tag{2.1.d}$$

In the equations, **B** is the magnetic induction, **E** is the electric field, **H** is the magnetic field ($\vec{B} = \mu_0 \vec{H}$), **D** denotes the electric displacement, ($\vec{D} = \varepsilon_0 \tilde{\varepsilon} \vec{E}$), j the current density, and ρ_f is the charge density, ε_0 and $\tilde{\varepsilon}$ is the permittivity of free space and relative permittivity of any form of medium. The electric and magnetic field salsifies the tangential and perpendicular components of Maxwell's boundary between two adjacent layers written as

$$\hat{n} \cdot (\vec{D}_1 - \vec{D}_2) = 0 \tag{2.2.a}$$

$$\hat{n} \cdot (\vec{B}_1 - \vec{B}_2) = 0 \tag{2.2.b}$$

$$\hat{n} \times (\vec{E}_1 - \vec{E}_2) = 0 \tag{2.2.c}$$

$$\hat{n} \times (\vec{H}_1 - \vec{H}_2) = \vec{J}_f \tag{2.2.d}$$

We focus on anisotropic media, the dielectric tensor of permittivity in three cartesian directions represented as

$$\tilde{\varepsilon} = \begin{pmatrix} \varepsilon_{xx} & 0 & 0 \\ 0 & \varepsilon_{yy} & 0 \\ 0 & 0 & \varepsilon_{zz} \end{pmatrix} \tag{1.3}$$

Where, ε_{xx} ε_{yy}, and ε_{yy} are. Since, the momentum space ($\vec{k}$) and the dielectric constant define the dispersion nature EM wave we represent Maxwell's Eqs. (2.1a-d) as

$$\vec{k} \times \vec{E} = -\mu_0 \omega \vec{H} \tag{2.4.a}$$

$$\vec{k} \times \vec{H} = \omega \vec{D} \tag{2.4.b}$$

Combining the above two equation we get curl form of wave equation

$$\vec{k} \times \vec{k} \times \vec{E} = -\mu_0 \omega^2 \varepsilon_0 \tilde{\varepsilon} \vec{E} \tag{2.5}$$

To gain good understanding of Eq. (2.5), we chose a plane EM wave of electric field amplitude and propagation vector represented in cartesian coordinate as

$$\mathbf{E}(\vec{r}) = (E_x \hat{x} + E_y \hat{y} + E_z \hat{z}) e^{i(k_x x + k_y y + k_z z - \omega t)} \tag{2.6}$$

The unit coordinate vectors $\hat{x}$, $\hat{y}$ and $\hat{z}$ represent the three cartesian directions, the respective component of wavevector are represented by k_x, k_y, and k_z E_x, E_y and E_y are amplitudes of electric field and c is the speed of light. The displacement vector assumes the form $\vec{D} = \tilde{\varepsilon} \vec{E} = \varepsilon_0 (\varepsilon_{xx} E_x \hat{x} + \varepsilon_{yy} E_y \hat{y} + \varepsilon_{zz} E_z \hat{z})$. From Eq. (2.5) and (2.6), the solution is a wave equation which is represented the dielectric tensor component

$$\vec{k} \times \vec{k} \times \vec{E} = -k_0^2 (\varepsilon_{xx} E_x \hat{x} + \varepsilon_{yy} E_y \hat{y} + \varepsilon_{zz} E_z \hat{z}) \tag{2.7}$$

where $k_0 = \omega/c$ is the vacuum wavenumber interms of the angular frequency. The solution to Eq. (2.7) is a matrix form given by

$$\begin{pmatrix} \varepsilon_{xx} k_0^2 - k_y^2 - k_z^2 & k_x k_y & k_x k_z \\ k_x k_y & \varepsilon_{yy} k_0^2 - k_x^2 - k_z^2 & k_y k_z \\ k_x k_z & k_y k_z & \varepsilon_{zz} k_0^2 - k_x^2 - k_y^2 \end{pmatrix} \begin{pmatrix} E_x \\ E_y \\ E_z \end{pmatrix} = 0, \tag{2.8}$$

Where the magnitude of the propagation vector $k^2 = k_x^2 + k_y^2 + k_z^2$.

2.1. 1 Dispersion nature in hyperbolic medium

To see the difference in the optical response of the different medium, we solve for the eigen solutions of the vectorwave of the electromagnetic fields in Eq. (2.8) by taking the determinant of the matrix and obtain the following,

$$\left(\frac{k_x^2+k_y^2}{\varepsilon_{zz}} + \frac{k_z^2}{\varepsilon_{xx}} - k_0^2\right)(k_x^2 + k_y^2 + k_z^2 - \varepsilon_{xx}k_0^2) = 0, \tag{2.9}$$

From the eigen solutions of the vector-wave, Eq (2.9), we obtain two roots, ordinary eigenmodes and extra-ordinary modes [2]. The ordinary eigenmode dispersion relation of the modes is given by

$$\frac{k_x^2+k_y^2+k_z^2}{\varepsilon_{xx}} - k_0^2 = 0 \tag{2.10}$$

and the extra-ordinary eigenmodes dispersion relation is solved as

$$\frac{k_x^2+k_y^2}{\varepsilon_{zz}} + \frac{k_z^2}{\varepsilon_{xx}} - k_0^2 = 0, \tag{2.11}$$

Based on the dielectric permittivity specially the part the solution in Eq. (2.10) and Eq. (2.11) we can easily classify different types of media and the result can be depicted by the isofrequency contour generated by the different components of wave vector [3,4]. If $\varepsilon_{zz} > 0$ and $\varepsilon_{xx} > 0$ then the medium is classified as dielectric, $\varepsilon_{xx} = \varepsilon_{yy} \neq \varepsilon_{zz}$, the medium is considered as uniaxial with an ellipsoid isofrequency and when $\varepsilon_{xx} = \varepsilon_{yy} = \varepsilon_{zz}$ it is isotropic with spherical isofrequency. When $\varepsilon_{zz}\,\varepsilon_{xx} < 0$ the isofrequency surface opens into an open hyperboloid and the medium behave as effective anisotropic metal. If $\varepsilon_{zz} < 0$ and $\varepsilon_{xx} > 0$ then the medium is called a type I hyperbolic and when $\varepsilon_{zz} > 0$ and $\varepsilon_{xx} < 0$ then the medium is called a type II hyperbolic with isofrequency contour opening. This means hyperbolic medium which can be in generally defined by the property $\varepsilon_{xx,}\varepsilon_{zz} < 0$ operates like a metal in one direction and a dielectric (insulator) in the other.
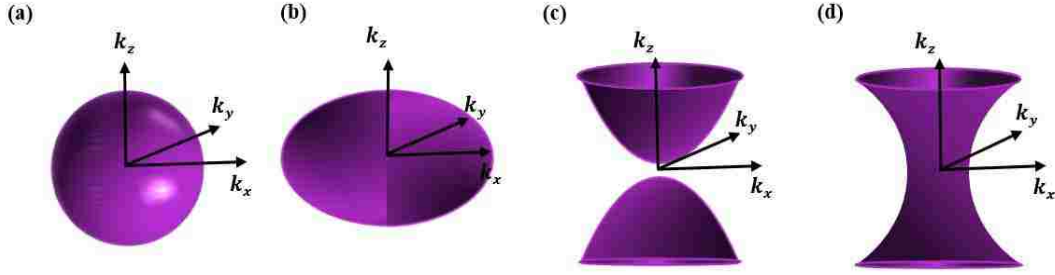
Figure 2.1 the spherical isofrequency surfaces for propagating waves in a medium with isotropic dielectric ($\varepsilon_{xx}=\varepsilon_{yy}=\varepsilon_{zz}$) (a). Anisotropic media ellipsoidal isofrequency ($\varepsilon_{xx} = \varepsilon_{yy} \neq \varepsilon_{zz}$) (b). A uniaxial hyperbolic medium with one positive and two negative components of the dielectric permittivity tensor ($\varepsilon_{xx}= \varepsilon_{yy} > 0, \varepsilon_{zz} < 0$, Type I) (c). A uniaxial hyperbolic medium with one negative and two positive components of the dielectric permittivity tensor ($\varepsilon_{xx}= \varepsilon_{yy} < 0, \varepsilon_{zz} > 0$, Type II) (d).

2.2 Light in two hyperbolic media

To investigate the properties such as propagation, dispersion, Fresnel coefficient of electromagnetic wave in different medium. We can now directly establish the magnetic field and the electric field relation in hyperbolic medium from the curl Eq. (2.7). Component by components by taking the left and right side of the electric field can be expresses in terms of the dielectric function and can be simplified to

$$[k_{jy}H_{jz} - k_{jz}H_{jy}] = -\varepsilon_0\varepsilon_{xx,j}E_{jx} \tag{2.12.a}$$

$$[k_{jz}H_{jx} - k_{jx}H_{jz}] = -\varepsilon_0\varepsilon_{yy,j}E_{jy} \tag{2.12.b}$$

$$[k_{jx}H_{jy} - k_{jy}H_{jx}] = -\varepsilon_0\varepsilon_{zz,j}E_{jz} \tag{2.12.c}$$

Now since we established the connection of electric and magnetic field in any medium (j), we considered two hyperbolic media labeled as 1and 2, and that includes a two-dimensional (2D) thin layer represented in figure 2.2a and 2.2b. In the schematic setting the anisotropic mediums lies in the $x - y$ plane. The first medium above $z = 0$ and the second hyperbolic bellow $z = 0$ and the two 2D material at $z = 0$. We also assume the anisotropic mediums are non-magnetooptical

10

($\mu_1 = \mu_2 = 1$) for simplicity. In the above electromagnetic waves are expressed as linear superposition of TE and TM waves, based on direction choice we will describe in the next two sections.
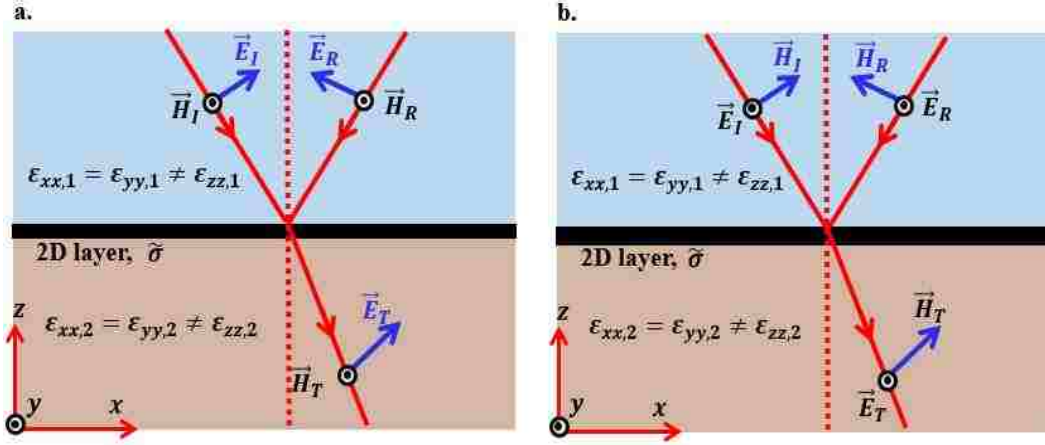
Figure 2.2 shows the electromagnetic field direction of TE (s) polarization (a) and TM polarization in top hyperbolic material ($z > 0$), bottom hyperbolic material ($z < 0$) and a 2D material characterized by an anisotropic conductivity (σ) included at $z = 0$ for the system in under consideration.

2.2.1 TM-polarized light reflection

Here we assume $x - z$ being plane of incidence as shown in figure (2.a) as such the incidence propagation vector in the first medium, $\boldsymbol{k_{1I}}$, and the incident TM mode magnetic field, $\vec{\mathbf{H}}_{\mathbf{I}}$, with an amplitude of H_I is represented as

$$\boldsymbol{k_{1I}} = k_{1x}\hat{x} + k_{1z}\hat{z} \tag{2.13}$$

$$\vec{\mathbf{H}}_{\mathbf{I}} = H_I \hat{y} e^{i(k_{1x}\hat{x}+k_{1z}\hat{z}-\omega t)}, \tag{2.14}$$

The electric field associated with the magnetic field from Eq. (2.12) is

$$(k_{1x}\hat{x} + k_{1z}\hat{z}) \times \vec{\mathbf{H}}_{\mathbf{I}} = -\varepsilon_0\tilde{\varepsilon}\vec{\mathbf{E}}_{\mathbf{I}} = -\varepsilon_0\varepsilon_{xx,1}E_{Ix}\hat{x} - \varepsilon_{zz,1}E_{Iz}\hat{z} \tag{2.15}$$

Where E_{Ix} and E_{Iz} the incident field electric field amplitude in the x and z direction. Similarly, the reflected magnetic field, $\vec{H}_R$, which propagating back with a momentum vector $\boldsymbol{k_{1R}} = k_{1x}\hat{x} - k_{1z}\hat{z}$ from the 2D interface at $z = 0$ with an amplitude of, H_R, is

$$\vec{H}_R = H_R\hat{y}e^{i(k_{1x}\hat{x}-k_{1z}\hat{z}-\omega t)}, \tag{2.16}$$

Similarly, the electric field reflected will be

$$(k_{1x}\hat{x} - k_{1z}\hat{z}) \times \vec{H}_R = -\varepsilon_0\tilde{\varepsilon}\vec{E}_R = -\varepsilon_0\varepsilon_{xx,1}E_{Rx}\hat{x} - \varepsilon_0\varepsilon_{zz,1}E_{Rz}\hat{z}, \tag{2.17}$$

The transmitted magnetic in the second medium below $z = 0$ with a propagation $\boldsymbol{k_2} = k_{2x}\hat{x} + k_{2z}\hat{z}$ is

$$\vec{H}_T = H_T\hat{y}e^{i(k_{2x}\hat{x}+k_{2z}\hat{z}-\omega t)}, \tag{2.18}$$

With the corresponding electric field

$$(k_{2x}\hat{x} + k_{2z}\hat{z}) \times \vec{H}_T = -\varepsilon_{xx,2}E_{Tx}\hat{x} - \varepsilon_0\varepsilon_{zz,2}E_{Tz}\hat{z} \tag{2.19}$$

At $z = 0$, the normal component of the electric field satisfies continuity boundary condition Maxwell's Eqs. (2.2), that is

$$\hat{n} \times (\vec{E}_1 - \vec{E}_2) = 0 \tag{2.20}$$

Where $\vec{E}_1$ is the total electric field in the first hyperbolic medium, $\vec{E}_1 = \vec{E}_I + \vec{E}_R$, and $\vec{E}_T$ is the electric field in the second medium $\vec{E}_2 = \vec{E}_T$. The normal unit vector point in the z direction, $\hat{n} = \hat{z}$, thus, the equation of the electric can be written as,

$$\hat{z} \times (\vec{E}_I + \vec{E}_R - \vec{E}_T) = 0, \tag{2.21}$$

The normal vector cross product with the electric field from Eq. (2.15), Eq. (2.17) and Eq. (2.19) leads to the following results

$$\hat{z} \times \left(\frac{k_{1x}}{\omega\varepsilon_0\varepsilon_{zz,1}}\hat{z} + \frac{k_{1z}}{\omega\varepsilon_0\varepsilon_{xx,1}}\hat{x}\right)H_Ie^{ik_{1x}x} = \hat{y}\frac{k_{1z}}{\omega\varepsilon_0\varepsilon_{xx,1}}H_Ie^{ik_{1x}x} \tag{2.22.a}$$

$$\hat{z} \times \left(\frac{k_{1x}}{\omega\varepsilon_0\varepsilon_{zz,1}} \hat{z} - \frac{k_{1z}}{\varepsilon_0\omega\varepsilon_{xx,1}} \hat{x} \right) H_{\mathrm{R}} e^{ik_{1x}x} = \hat{y} \frac{-k_{1z}}{\omega\varepsilon_0\varepsilon_{xx,1}} H_{\mathrm{R}} e^{ik_{1x}x} \qquad (2.22.\mathrm{b})$$

$$\hat{z} \times \left(\frac{k_{2x}}{\omega\varepsilon_0\varepsilon_{zz,2}} \hat{z} + \frac{k_{2z}}{\omega\varepsilon_0\varepsilon_{xx,2}} \hat{x} \right) H_{\mathrm{T}} e^{ik_{2x}x} = \hat{y} \frac{k_{2z}}{\omega\varepsilon_0\varepsilon_{xx,2}} H_{\mathrm{T}} e^{ik_{2x}x} \qquad (2.22.\mathrm{c})$$

The time dependent exponential factor, $e^{-i\omega t}$, is a common denominator for the EM field in both medium and excluded in the expression as it is not affected by the boundary conditions. Which we will do in other part of derivations in the dissertation when it is convenient. By combining the above three equations in to Eq. (2.21), after few algebras leads to a reduced equation form of,

$$\frac{k_{1z}}{\varepsilon_{xx,1}} H_{\mathrm{I}} - \frac{k_{1z}}{\varepsilon_{xx,1}} H_{\mathrm{R}} - \frac{k_{2z}}{\varepsilon_{xx,2}} H_{\mathrm{T}} = 0, \qquad (2.23)$$

In the tangential direction, $x - y$ plane, the components of the magnetic field and the electric field induces a surface currents in the 2D conducting sheet. The boundary condition of Eq (2.2d) related by Ohm's law, $\hat{n} \times (\vec{\mathbf{H}}_1 - \vec{\mathbf{H}}_2) = \vec{J}_f = \tilde{\sigma}\vec{\mathbf{E}}_t$. Where the electric field $\vec{\mathbf{E}}_t$ is the tangential field at the interface of the two media. The solution of the boundary condition can be achieved depending on the nature of $\tilde{\sigma}$. We chose 2D material without static magnetic bias (Hall effect) of an anisotropic conductivity represent by a matric tensor form,

$$\tilde{\sigma} = \begin{pmatrix} \sigma_{xx} & 0 \\ 0 & \sigma_{yy} \end{pmatrix} \qquad (2.24)$$

Few good examples of realistic 2D material that follows similar conductivity model are; graphene, $\sigma_{xx} = \sigma_{yy}$, which is isotropic 2D material and black phosphorene, $\sigma_{xx} \neq \sigma_{yy}$, anisotropic 2D material. Monolayer (one-atom-thick) or a few layers systems, which are scaled as two-dimensional material, are characterized by a two-dimensional sheet conductivity than volume conductivity. However, there relationship connecting this conductivity can be obtained as follows.

Since we only surface current density, $\vec{J}_s = J_x\hat{x} + J_y\hat{y}$, in $x - y$ plane is due to the excitation of electron on the surface by the external electric field. The volume current density, J_f, is related with the surface current by the expressed $\vec{J}_f = \vec{J}_s(x, y)\delta(z)$. This also applies to the volume, (ρ_f), and surface charge density (ρ_s), i.e. $\rho_f = \rho_s(x, y)\delta(z)$. In case of incident light with a wavelength extremely larger than the thickness, t, of the conducting sheet the electric field is approximately constant with the 2D layer [5]. Therefore, 2D current density traversing a line element across the thickness t is $\int \vec{J}_f dz = \int \vec{J}_s(x, y)\delta(z)dz = \int \tilde{\sigma}E(z)dz \approx \tilde{\sigma}t\vec{E}(\vec{r})$. Such that equivalent representation of to a 2D sheet conductivity and the 3D conductive in general are connected by the thickness, in a simple form $\tilde{\sigma}_s = \tilde{\sigma}_f t$ [6].

We can use the above assertion to implement it in Maxwell's boundary condition, hence Eq. (2.2d) becomes

$$\hat{n} \times (\vec{H}_1 - \vec{H}_2) = \vec{J}_f = \sigma_{xx}\hat{x}(\vec{E}_I)_x + \sigma_{yy}\hat{y}(\vec{E}_I)_y + \sigma_{xx}\hat{x}(\vec{E}_R)_x + \sigma_{yy}\hat{y}(\vec{E}_R)_y \qquad (2.25)$$

Where $\vec{H}_1 = \vec{H}_I + \vec{H}_R$ **and** the directional surface current and the respective conductivity of the 2D layer is $J_x = \sigma_{xx}E_{1x}$ and $J_y = \sigma_{yy}E_{1y}$. Since there is no y component electric field $J_y = 0$. The expression of the right side of Eq. (2.25) leads to

$$\hat{z} \times \vec{H}_I = (\hat{z} \times \hat{y})H_I e^{i(k_{1x}x)} = -\hat{x}H_I e^{i(k_{1x}x)}, \qquad (2.26.\text{a})$$

$$\hat{z} \times \vec{H}_R = (\hat{z} \times \hat{y})H_R e^{i(k_{1x}x)} = -\hat{x}H_R e^{i(k_{1x}x)}, \qquad (2.26.\text{b})$$

$$\hat{z} \times \vec{H}_T = (\hat{z} \times \hat{y})H_T e^{i(k_{2x}x)} = -\hat{x}H_T e^{i(k_{2x}x)} \qquad (2.26.\text{c})$$

Combining Eqs. (2.26a-d) and (2.25) after some algebraic manipulation we arrive to

$$H_I + H_R - H_T = \frac{\sigma_{xx}k_{1z}}{\omega\varepsilon_0\varepsilon_{xx,1}}[H_I - H_R] \qquad (2.27)$$

Using Eq. (2.27) in Eq. (2.23) we get the final equation of Fresnel reflection coefficient (r_{12}^p) of two-dimensional material included between two semi-infinite hyperbolic layers as,

$$r_{12}^p = \frac{H_R}{H_I} = \frac{\varepsilon_{xx,2}k_{1z} - \varepsilon_{xx,1}k_{2z} + \frac{\sigma_{xx}k_{1z}k_{2z}}{\omega\varepsilon_0}}{\varepsilon_{xx,2}k_{1z} + \varepsilon_{xx,1}k_{2z} + \frac{\sigma_{xx}k_{1z}k_{2z}}{\omega\varepsilon_0}} \tag{2.28}$$

2.2.3 TE polarized mode

Similarly, the Fresnel coefficient in the case for TE polarization can be obtained defining the electric field wave propagating parallel to the interface in the two medium is given by

$$\vec{E}_I = E_I \hat{y} e^{i(k_{1x}x + k_{1z}z - \omega t)} \tag{29.a}$$

$$\vec{E}_R = E_R \hat{y} e^{i(k_{1x}x - k_{1z}z - \omega t)} \tag{29.b}$$

$$\vec{E}_T = E_T \hat{y} e^{i(k_{2x}x + k_{2z}z - \omega t)} \tag{29.c}$$

The magnetic field in the y direction is zero hence the corresponding to the above field the magnetic fields are,

$$\vec{H}_I = (H_{Ix}\hat{x} + H_{Iz}\hat{z}) e^{i(k_{1x}x + k_{1z}z - \omega t)} \tag{30.a}$$

$$\vec{H}_R = (H_{Rx}\hat{x} + H_{Rz}\hat{z}) e^{i(k_{1x}x - k_{1z}z - \omega t)} \tag{30.b}$$

$$\vec{H}_T = (H_{Tx}\hat{x} + H_{Tz}\hat{z}) e^{i(k_{2x}x + k_{2z}z - \omega t)} \tag{30.c}$$

We use the Maxwell's Eq. (2.4.a) the only electric field that survive are attained as follows.

$$K \times E_I \hat{y} e^{i(k_{1x}x + k_{1z}z)} = -\omega\mu_0 (H_{Ix}\hat{x} + H_{Iz}\hat{z}) e^{i(k_{1x}x + k_{1z}z)} \tag{2.31}$$

This gives us,

$$-\omega\mu_0 (H_{Ix}\hat{x} + H_{Iz}\hat{z}) = k_{1x}E_I\hat{z} + k_{1z}E_I\hat{x} \tag{2.32}$$

Splitting perpendicular and parallel components of the magnetic field in each medium we get

$$H_{Ix} = \frac{k_{1z}E_I}{\omega\mu_0} \tag{2.33.a}$$

$$H_{Rx} = -\frac{k_{1z}E_R}{\omega\mu_0} \tag{2.33.b}$$

$$H_{Tx} = \frac{k_{2z}E_T}{\omega\mu_0} \tag{2,33.c}$$

15

And the perpendicular component of H is

$$H_{\text{Iz}} = -\frac{k_{1x}E_I}{\omega\mu_0} \tag{2.34.a}$$

$$H_{\text{Rz}} = \frac{k_{1x}E_R}{\omega\mu_0} \tag{2.34.b}$$

$$H_{\text{Tz}} = -\frac{k_{2x}E_T}{\omega\mu_0} \tag{2.34.c}$$

At the boundary $z = 0$ the perpendicular component of the magnetic field is continuing. The parallel compote of the electric field is continuing and matching the solutions for $z < 0$ and $z > 0$ using these boundary conditions of continuity, the normal component magnetic field ($\boldsymbol{\mu_1 H_{1z}} = \boldsymbol{\mu_2 H_{\text{Iz}}}$) we get

$$\frac{k_{1x}E_I}{\omega\mu_0} + \frac{k_{1x}E_R}{\omega\mu_0} = \frac{k_{2x}E_T}{\omega\mu_0} \tag{2.35}$$

The same result also can be achieved from the electric field tangent component for TE mode we have the following from the first boundary condition Eq. (2.2a)

$$E_I + E_R = E_T \tag{2.36}$$

And from the second boundary condition which is tangent to the electric field the x compote of the magnetic field

$$H_{Ix} + H_{Rx} - H_{Tx} = \omega\mu_0\sigma_{yy}[E_I + E_R] \tag{2.37}$$

Combining Eq. (2.36) and Eq. (2.37) after taking the electric field amplitude ratio of reflected and incident field we arrive to the reflection coefficient given by

$$k_{1z}E_I - k_{1z}E_R - k_{2z}[E_I + E_R] = \omega\mu_0\sigma_{yy}[E_I + E_R] \tag{2.38}$$

$$r_{12}^s = \frac{E_R}{E_I} = \frac{k_{1z}-k_{2z}-\omega\mu_0\sigma_{yy}}{k_{1z}+k_{2z}+\omega\mu_0\sigma_{yy}} \tag{2.39}$$

In the case where there is no 2D material between the two hyperbolic interface we can set the conductivity to be zero ($\tilde{\sigma} = 0$). The expression in Eq. (2.28) and Eq. (2.39) recovers a well-known

reflection and transmission coefficient between two hyperbolic mediums. Doing so the modified Fresnel reflection coefficients becomes,

$$r_{12}^p = \frac{\varepsilon_{xx,2}k_{1z} - \varepsilon_{xx,1}k_{2z}}{\varepsilon_{xx,2}k_{1z} + \varepsilon_{xx,1}k_{2z}} \tag{2.40}$$

And

$$r_{12}^s = \frac{k_{1z} - k_{2z}}{k_{1z} + k_{2z}} \tag{2.41}$$

It is important to notice that the reflection coefficient also gives indirect information field that are confined at the interface, surface confined plasmons. For example, a light shined for two media with dielectric constant ε_1 and ε_2 (dielectric and gold) the surface plasmon propagating, k_{SP}, at the interface can be obtained from poles of the imaginary part of this reflection coefficient r_{12}^p. Straightforward calculations by setting $k_{1z} = k_{2z} = k_{sp}$ result in the dispersion equations for TM mode [7],

$$k_{SP} = \omega/c\sqrt{\varepsilon_1\varepsilon_2/(\varepsilon_1 + \varepsilon_2)} \tag{2.42}$$

2.3 Transfer matrix approach in layered medium

Having provided the general theory of light mater interaction in hyperbolic medium, we now consider a scenario where two 2D material layers which are separated by a dielectric slab of hyperbolic layer with a thickness of t displayed model figure 2.3.
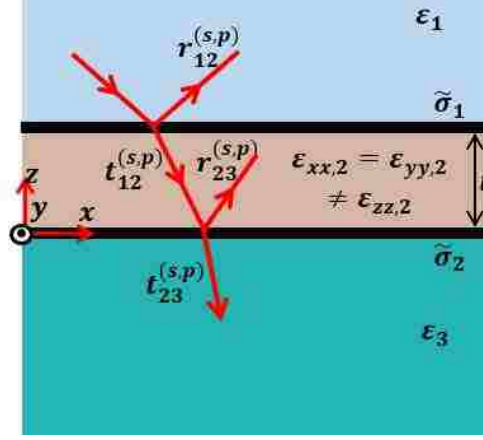
Figure 2.3. Schematic illustration of the system for Fresnel coefficient calculation. First 2D conducting sheets characterized by surface conductivity $\tilde{\sigma}_1$ at $z = 0$, second conducting sheet of conductivity $\tilde{\sigma}_2$ at $z = t$, separated by anisotropic hyperbolic slab of thickness t, the top and bottom semi-infinite of optical constant ε_1 and ε_3, respectively.

The three mediums are labeled as 1, 2 and 3. Medium 1 above 2D conducting represented by dielectric constant, ε_1, above $z > t$, first 2D material given by conductivity $\tilde{\sigma}_1$ (placed at $z = t$), the hyperbolic layer film ($0 < z < t$) region medium 2 sandwiched between the top 2D material and bottom 2D material with conductivity $\tilde{\sigma}_2$ (placed at $z = 0$), the bottom region bellows the second 2D material as medium 3 semi-infinite dielectric,ε_3, material acting as substrate. In Order to determine the total Fresnel transmission and reflection coefficient of a such multilayer hybrid system it is essential to get the propagation vector of light in intermediate layers. While, the electric or magnetic fields can be related to inside the medium is between the two conducting sheets can be connected by propagation matrix. Based on the two conditions and with the knowledge of dielectric permittivity of each layer, we will employ well-known formalism, the transfer matrix ($\tilde{M}_j$) [8], for multilayer slabs to relate the reflection and transmission coefficients from each interface j between layers j and $j + 1$ (outermost semi-infinite layers to lower most semi-infinite layer). Therefore, we can easily calculate the optical response, total reflection, total transmission and total absorption 2D material material including multilayer system. Since the Fresnel

reflection coefficient would be different for s- and p-polarized excitation of incident light for anisotropic medium the transfer matrix elements are also different. Explicitly, for s- polarization and p-polarization state of a three-layer system transfer matrix is written as $\widetilde{M}_j^{(s,p)} = \widetilde{M}_1^{(s,p)} \cdot \widetilde{M}_2^{(s,p)}$ and the matrix elements are given by

$$\widetilde{M}_1^{(s,p)} = \frac{1}{t_{12}^{(s,p)}} \begin{pmatrix} e^{-ik_{2z}^{(s,p)}t} & r_{12}^{(s,p)}e^{ik_{2z}^{(s,p)}t} \\ r_{12}^{(s,p)}e^{-ik_{2z}^{(s,p)}t} & e^{ik_{2z}^{(s,p)}t} \end{pmatrix} \qquad (2.43)$$

$$\widetilde{M}_2^{(s,p)} = \frac{1}{t_{23}^{(s,p)}} \begin{pmatrix} 1 & r_{23}^{(s,p)} \\ r_{23}^{(s,p)} & 1 \end{pmatrix} \qquad (2.44)$$

$$\widetilde{M}^{(s,p)} = \frac{1}{t_{12}^{(s,p)}} \begin{pmatrix} e^{-ik_{2z}^{(s,p)}t} & r_{12}^{(s,p)}e^{ik_{2z}^{(s,p)}t} \\ r_{12}^{(s,p)}e^{-ik_{2z}^{(s,p)}t} & e^{ik_{2z}^{(s,p)}t} \end{pmatrix} \cdot \frac{1}{t_{23}^{(s,p)}} \begin{pmatrix} 1 & r_{23}^{(s,p)} \\ r_{23}^{(s,p)} & 1 \end{pmatrix} \qquad (2.45)$$

Where $t_{12}^{(s,p)}$ and $r_{12}^{(s,p)}$ represents the Fresnel transmission and reflection of medium 1 and 2 respectively; $t_{23}^{(s,p)}$ and $r_{23}^{(s,p)}$ represents the Fresnel transmission and reflection of medium 2 and 3, respectively; and $k_{2z}^{(s,p)}$ is the propagation vector in medium 2. The superscript s and p stands for s-polarization and for p-polarization direction of light, respectively. The total reflection coefficient in the such multilayer system is calculated the final product of matrix element of Eq. (2.45)

$$r_{123}^{(s,p)} = \frac{\widetilde{M}_{21}^{(s,p)}}{\widetilde{M}_{11}^{(s,p)}} \qquad (2.46)$$

The simplified for of the above equation yields the well-known solution

$$r_{123}^{(s,p)} = \frac{r_{12}^{(s,p)} + r_{23}^{(s,p)} e^{2ik_{1z}^{(s,p)}t}}{1 + r_{12}^{(s,p)} r_{23}^{(s,p)} e^{2ik_{1z}^{(s,p)}t}} \tag{2.47}$$

The total transmission coefficient is obtained from Eq. (2.47) matrix element,

$$t_{123}^{(s,p)} = \frac{1}{\tilde{M}_{11}^{(s,p)}} \tag{2.48}$$

From the simplified for of equation (above), we get

$$t_{123}^{(s,p)} = \frac{t_{12}^{(s,p)} t_{23}^{(s,p)} e^{ik_{1z}^{(s,p)}t}}{1 + r_{12}^{(s,p)} r_{23}^{(s,p)} e^{2ik_{1z}^{(s,p)}t}} \tag{2.49}$$

This theoretical approach thus allows us to calculate the another relevant quantities total reflectance ($R_{123}^{(s,p)}$) and the transmittance, ($T_{123}^{(s,p)}$), from the multilayer system that includes 2d material at each interface, $R_{123}^{(s,p)} = |r_{123}^{(s,p)}|^2$ and $T_{123}^{(s,p)} = |t_{123}^{(s,p)}|^2$, respectively. The absorbance can also be evaluated directly from $A_{123}^{(s,p)} = 1 - R_{123}^{(s,p)} - T_{123}^{(s,p)}$.

2.4 Green function formalism point dipole for spontaneous emission

The Fresnel coefficients from the transfer matrix obtained have significant theoretical input to study interaction of point dipole emitters in 2D material, hyperbolic material and semi-conductor metallic materials. In this section, we will develop a theoretical model for the spontaneous emission (SE) rate implementing well-developed technique; the Green's tensor formalism [9]. This method has been implicated to study point dipole, finite-size, two-dimensional array or three dimensional nano-emitters embedded in metal-dielectric multilayer system. Taking these points

in mind, we will derive SE rate due to a point dipole placed in vacuum above a 2D conducting sheet on a dielectric substrate. Then, we carry out a straightforward extension of this analysis to calculate the decay rate of an emitter in a system of consisting more than one 2D conducting layer and a thin film of hyperbolic layer; identical to previous section multilayer system.

First, the Maxwell's curl equations Eq. (2.1b) and Eq. (2.1d) are described of electric and magnetic field in the presence of source currents, $\mathbf{J_f}$, are modified as

$$\nabla \times \mathbf{E}(\vec{r}, \omega) = i\omega\mu_0\mathbf{H}(\vec{r}, \omega) \tag{2.50}$$

$$\nabla \times \mathbf{H}(\vec{r}, \omega) = i\omega\mu_0\mu\varepsilon_0\tilde{\varepsilon}\mathbf{E}(\vec{r}, \omega) + \mathbf{J_f}(\vec{r}, \omega) \tag{2.51}$$

Combining Eq (2.50) and Eq. (2.51) leads to complete electromagnetic wave equation including a source current density as

$$\nabla \times \nabla \times \mathbf{E}(r, \omega) = -\mu_0\mu\varepsilon_0\tilde{\varepsilon}\frac{\partial^2 E(\vec{r},\omega)}{\partial t^2} - \mu_0\mu\frac{\partial J_f(\vec{r},\omega)}{\partial t} \tag{2.52}$$

The electric field produced by the current source in any medium can be given through the Green's function which is also a solution to Eq. (2.52). The electric field in terms of the Green's function and the current source related by

$$\mathbf{E}(\vec{r}, \omega) = i\omega\mu_0\mu\varepsilon_0\tilde{\varepsilon} \int dr' \mathbf{G}(\vec{r}, \vec{r}_0, \omega) \cdot \mathbf{J_f}(\vec{r}, \vec{r}_0, \omega) \tag{2.53}$$

Where, $\mathbf{G}(\vec{r}, \vec{r}_0, \omega)$ is the Green's function, the vector $\boldsymbol{r}$ denotes the location of the point source of frequency ω and $\boldsymbol{r_0}$ is point of observation. From the current density of homogeneous wave Eq. (2.51) and combining Eq. (2.53), we obtain a solution of Maxwell's equation in the form,

$$\nabla \times \nabla \times \mathbf{G}(\vec{r}, \vec{r}_0, \boldsymbol{\omega}) - k_0^2\tilde{\varepsilon}\mathbf{G}(\vec{r}, \vec{r}_0, \omega) = \mathbf{I}\delta(\vec{r}, \vec{r}_0,) \tag{2.54}$$

where $\mathbf{I}$ is 3 by 3 is the unit dyadic matrix tensor and δ is Dirac delta function. Solving for all the matrix components of the green tensor leads to the equation for the primary field emitted by the oscillating dipole and for the field produced by surrounding medium characteristics to a given the

point source orientation. In order to address Eq. (2.53) using the Green's function Eq. (2.54) we considered a point dipole situated between two planar interfaces speared by a 2D conducting layer, figure 2.4a-b. According to the schematics given, figure 2.4a, the dipole is positioned at a distance $z = d$ above the 2D layer in medium 1. We focus for now on figure 2.4a regard both medium 1 and medium 2 as semi-infinite layer, infinitely large in the z direction. The interfaces of the layers are configured parallel to the $x - y$ plane.
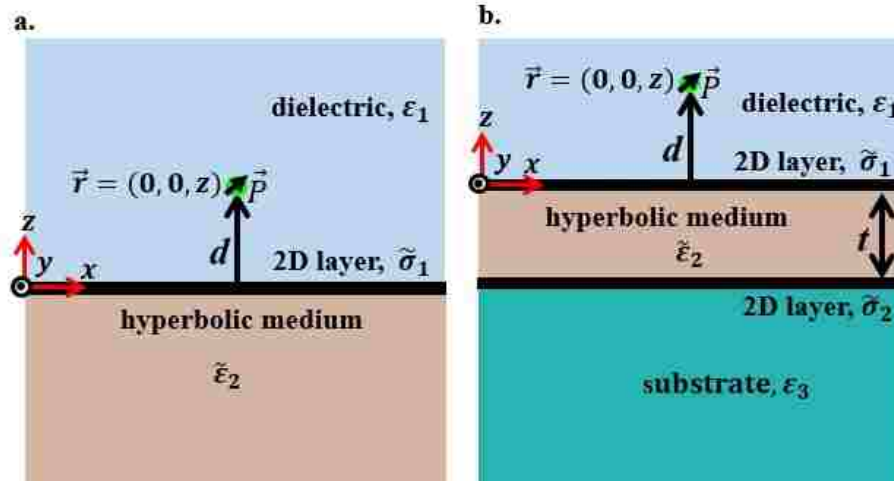
Figure 2.4, Schematic representation of the geometry considered for SE rate calculation. An emitter of dipole moment **P** at z =d (a) from a 2D conducting sheet (z =0) inside a dielectric medium, and (b) from a 2D conducting sheet (z =0) inside a dielectric medium a second 2D layer and hyperbolic medium of thickness t.

The electric current density of the electric dipole with electric dipole moment $\vec{P}$ placed at $\vec{r}$ is

$$je(\vec{r}) = -i\omega\vec{P}\,\delta(\vec{r} - \vec{r}_0) \tag{2.55}$$

The dipole considered in this study is nonmagnetic. The electric dipole moment in the respective x, y and z direction is denoted as $\vec{P} = P_x\hat{x} + P_y\hat{y} + P_z\hat{z}$. P_x, P_x, and P_x are the electric dipole moment components in the x, y and z direction, respectively. The total electric fields resulting from a point dipole source with current moment is above the interface medium is the superposition of field radiated by a point dipole, $\mathbf{E_0}$, and the electric field reflected from the first interface in the

same region where the dipole is embedded, $\mathbf{E_R}$, $\vec{\mathbf{E_T}} = \vec{\mathbf{E_I}} + \vec{\mathbf{E_R}}$. This electric field in the upper half-space (z > 0) includes the sum of the primary Greens function in the dipole region and the reflected Greens function from the first 2D interface as

$$\mathbf{E_T}(\vec{r},\vec{r}_0,\omega) = \omega^2 \mu_0 \mu_1 [\mathbf{G_0}(\vec{r},\vec{r}_0,\omega) + \mathbf{G_R}(\vec{r},\vec{r}_0,\omega)] \cdot \vec{\mathbf{P}} \qquad (2.56)$$

The first term is the field directly radiated by the dipole to the observation point through free space Green's function, $\mathbf{G_0}$ contribution. Which is given by

$$\mathbf{E_I} = \omega^2 \mu_0 \mu_1 [\mathbf{G_0}(\vec{r},\vec{r}_0,\omega)] \cdot \vec{\mathbf{P}} \qquad (2.57)$$

The free space Green's function that satisfies as a solution to Eq. (2.54) is a spherical wave equation [1] of the form,

$$\mathbf{G_0}(\vec{r},\vec{r}_0) = \frac{e^{\pm ik|\vec{r}-\vec{r}_0|}}{4\pi|\vec{r}-\vec{r}_0|}, \qquad (2.58)$$

Where + (-) denotes a spherical wave propagating outward (towards) of a point source. The second term in Eq. (2.56) represents the field radiated after reflection from the interface and the reflected (scattered) Green's function, $\mathbf{G_R}$, to the observation point. In multilayer system GR also accounts for the multiple reflections and transmissions taking place at the interfaces. Moreover, for (z < 0) the transmitted field, $\mathbf{E}_t$, bellow the interface, inside the medium 2, is also represented in terms of the transmitted Green's function, $\mathbf{G_t}$, as

$$\mathbf{E}_t(\vec{r},\vec{r}_0,\omega) = \omega^2 \mu_0 \mu_2 \mathbf{G_t}(\vec{r},\vec{r}_0,\omega) \cdot \vec{\mathbf{P}} \qquad (2.59)$$

Both the reflected and transmitted Green's function can be obtained from $\mathbf{G_0}$. The explicit form of dyadic Green's function as a solution of Eq. (2.54) is

$$\mathbf{G}(\vec{r},\vec{r}_0) = (\mathbf{I} + \frac{1}{k^2}\nabla\nabla)\mathbf{G_0}(\vec{r},\vec{r}_0), \qquad (2.60)$$

Now, we can calculate the amount of power radiated, W, at position $\boldsymbol{r}$ from the various electric field contribution, once the it is calculated from $\mathbf{G}$. According to Poynting theorem, the time–

averaged radiated power by a dipole with a harmonic time dependence source is represented in terms of the electric field and the source current density [10]

$$W = -\frac{1}{2} \oiiint Re\{\vec{J}_e^* \cdot \vec{\mathbf{E}}_T\} \, dV \tag{2.61}$$

where V encloses the source and $\mathbf{J_f}$ represents the source density current. Introducing the value of the current density Eq. (2.55) in to Eq. (2.61), the power evaluated at position $\vec{r}_0$ is

$$W = \frac{\omega}{2} Im\{\vec{P}^* \cdot \vec{\mathbf{E}}_T(\vec{r}_0)\} \tag{2.62}$$

When the optical emitter is only in free space, the radiated power, W_0, is

$$W_0 = \frac{\omega}{2} Im\{\vec{P}^* \cdot \vec{\mathbf{E}}_I(\vec{r}_0)\}, \tag{2.63}$$

Substituting Eq. (2.57) in Eq. (2. 63) we get the expression of the power radiated by the incident field in free space

$$W_0 = \frac{\omega^3 \mu_0 \mu_1}{2} Im\{\vec{P}^* \cdot [\mathbf{G}_0(\vec{r}, \vec{r}_0, \omega)] \cdot \vec{P}\}, \tag{2.64}$$

Thus, SE can be calculated by taking the power radiative ratio of the point dipole in dielectric surrounding with that of the power radiated in a vacuum space. This SE defined by the power ratio is also analogous to the Purcell effect [11] and given as

$$\frac{\Gamma}{\Gamma_0} = \frac{W}{W_0} = 1 + \frac{2}{\Gamma_0 \hbar} Im\{\vec{P}^* \cdot \vec{\mathbf{E}}_R\} \tag{2.65}$$

Where, Γ is the SE rate for the excitation lying in the vicinity of a neighborhood dielectric, Γ_0 is the SE rate of the dipole emitter in a free space, $\Gamma_0 = 4\omega^3|P|^2/3\hbar c^3$, and $\hbar$ the reduced Planck constant. Since the most essential element in Eq. (2.60) is the full expression of the reflected electric field that can evaluated from dyadic Green's function. To do so, we regard the Green's function as a superposition of two s and p polarization mode and an expanded as a summation of plane waves. According to the Weyl's identity [9, 12] plane wave expanded form of Green's function into an angular spectrum

$$G_R(\vec{r}, \vec{r}_0, \omega) = \frac{i}{8\pi^2} \iint_{-\infty}^{\infty} \frac{\{M_R^S + M_R^p\} e^{i[k_x(x-x_0)+k_y(y-y_0)+k_z(z-z_0)]}}{k_{1z}} dk_x dk_y \qquad (2.66)$$

Where the quantities M_R^S and M_R^p are given by the wavevector and the reflection coefficients of for each polarization between the between the two dielectric mediums. It is essential to notice that the effect of 2D conducting sheet contribution is included in the wave vector dependent reflection coefficient. The form of M_R^S and M_R^p can be found is

$$M_R^S = \frac{r^s(k_x, k_y)}{k_{1z}(k_x^2 + k_y^2)} \begin{bmatrix} k_y^2 & -k_x k_y & 0 \\ -k_x k_y & k_x^2 & 0 \\ 0 & 0 & 0 \end{bmatrix} \qquad (2.67)$$

$$M_R^p = \frac{r^p(k_x^2, k_y^2)}{k_1^2(k_x^2 + k_y^2)} \begin{bmatrix} k_x^2 k_{1z} & -k_x k_y k_{1z} & k_x(k_x^2 + k_y^2) \\ -k_x k_y k_{1z} & k_y^2 k_{1z} & k_y(k_x^2 + k_y^2) \\ -k_x(k_x^2 + k_y^2) & k_y(k_x^2 + k_y^2) & -\frac{(k_x^2 + k_y^2)}{k_{1z}} \end{bmatrix} \qquad (2.68)$$

Similarly, the green functions in the transmitted medium or in the ferroelectric layer can also be expressed in terms of the transmission Fresnel coefficients of the t^p and t^s polarization as follow

$$M_t^S = \frac{t^s(k_x, k_y)}{k_{1z}(k_x^2 + k_y^2)} \begin{bmatrix} k_y^2 & -k_x k_y & 0 \\ -k_x k_y & k_x^2 & 0 \\ 0 & 0 & 0 \end{bmatrix} \qquad (2.69)$$

$$M_t^p = \frac{t^p(k_x^2, k_y^2)}{k_1 k_2(k_x^2 + k_y^2)} \begin{bmatrix} k_x^2 k_{2z} & -k_x k_y k_{2z} & k_x(k_x^2 + k_y^2)/k_{1z} \\ -k_x k_y k_{1z} & k_y^2 k_{2z} & k_y(k_x^2 + k_y^2)/k_{1z} \\ -k_x(k_x^2 + k_y^2) & k_y(k_x^2 + k_y^2) & -\frac{(k_x^2 + k_y^2)}{k_1} \end{bmatrix} \qquad (2.70)$$

Where, ($r^{(s,p)}$ and $t^{(s,p)}$) are the total Fresnel reflection and transmission coefficients for the fields of incoming s- and p-polarization plane wave, respectively.

The convenient way to evaluate the integral of the Green's matrix function Eq. (2.65) is to transform the coordinates from cartesian to cylindrical coordinate. Hence, the spontaneous

25

emission rate can be obtained as an integral over the parallel wave vector, k_ρ, and azimuthal angle of polar coordinate, φ, covering the $x - y$ plane. We define $k_{x1} = k_\rho cos\varphi$, $k_{y1} = k_\rho sin\varphi$, φ is the angle between k_ρ and x axis, $dk_{x1}dk_{y1} = dk_\rho k_\rho d\rho$, where $k_\rho = \sqrt{k_{1x}^2 + k_{1y}^2}$ is the wavevector parallel to the interface between the dipole medium and the semi finite layers. In this case the reflected Green's tenors form of s and p is summarized as follows,

$$\mathbf{G_R}(\vec{r},\vec{r}_0,\omega) = \frac{i}{8\pi^2} \int_0^\infty k_\rho dk_\rho \, e^{ik_x(x-x_0)+k_y(y-y_0)+k_z(z-z_0)}$$

$$\left[\frac{r^p}{k_{z1}} \begin{pmatrix} k_\rho^2 & 0 & 0 \\ 0 & k_\rho^2 & 0 \\ 0 & 0 & -2k_\rho^2 \end{pmatrix} - \frac{2r^s k^2}{k_{z1}} \begin{pmatrix} 1 & 0 & 0 \\ 0 & 1 & 0 \\ 0 & 0 & 0 \end{pmatrix} \right] \tag{2.71}$$

For example, in Eq. (2.71), the component $\mathbf{G}_{R,xx}^s(\vec{r},\vec{r}_0,\omega)$ and $\mathbf{G}_{R,xx}^p(\vec{r},\vec{r}_0,\omega)$ denotes the x-component of the reflected. In the case where the measurement it is taking place away from the dipole source the integral leads to Bessel's function or spherical harmonics solution as conducted using Sommer field approach. The main simple approach to solve the above integral is in the angular direction is to simply it in such a way that the dipole emitter in our set to be above the origin of the $x - y$ plane, $\vec{r} = (0,0,z = d)$. For instance, the s polarization component of the reflected Greens can be given as

$$G_{xx}^S(\vec{r},\vec{r}_0,\omega) = -\frac{i}{8\pi^2} \int_{-\infty}^\infty \int_0^{2\pi} \frac{r_{12}^S k_\rho dk_\rho d\varphi}{k_{1z}} e^{ik_{z1}z'} e^{i\rho k_\rho cos\varphi} sin^2\varphi \tag{2.72}$$

The integral expressions in Eq. (2.71), Eq. (2.72) and Eq. (2.64) we get the final expression of the reflected field as

$$\mathbf{E}_R = \omega^2 \mu_0 \mu_1 \left\{ \frac{i\pi}{8\pi^2} \int_0^\infty k_\rho dk_\rho \, e^{ik_{z1}z'} \left[\frac{r_{12}^p}{k_{z1}} \begin{pmatrix} k_\rho^2 & 0 & 0 \\ 0 & k_\rho^2 & 0 \\ 0 & 0 & -2k_\rho^2 \end{pmatrix} - \right.\right.$$

$$\left.\left. \frac{2r_{12}^s k^2}{k_{z1}} \begin{pmatrix} 1 & 0 & 0 \\ 0 & 1 & 0 \\ 0 & 0 & 0 \end{pmatrix} \right] P \right\} \qquad (2.73)$$

This equation of the reflected field gives the SE rate for any dipole emitter orientation. We can split based on the dipole orientation to gain a simplified model equation. For the normalized SE rate, we consider to orientation; a dipole oriented perpendicular, $\frac{\Gamma_\perp}{\Gamma_0}$, (oriented in the z direction), and parallel, $\frac{\Gamma_\parallel}{\Gamma_0}$, (oriented along $x - y$ plane) with respect the interface medium. Substituting Eq (2.73) in Eq. (2.64) we achieve a simplified separate equation. Hence, the SE rate can be written as,

$$\frac{\Gamma_\perp}{\Gamma_0} = 1 + \frac{3}{2k_0^3} Re \left(\int_0^\infty \frac{r_{12}^p e^{2ik_{1z}d} k_\rho^3 dk_\rho}{k_{z1}} \right), \qquad (2.74)$$

$$\frac{\Gamma_\parallel}{\Gamma_0} = 1 + \frac{3}{4k_0^3} Re \left(\int_0^\infty \frac{k_\rho dk_\rho}{k_{z1}} e^{2ik_{1z}d} \left[k_0^2 r_{12}^s e^{2ik_{1z}d} - k_{1z}^2 r_{12}^p \right] \right) \qquad (2.75)$$

It is essential to notice that in Eq. (2.74) and (2.74) the first term is normalized dipole in medium 1, with a unit value. The second integral term the includes the possible contributions originate from f propagation wave vector when k_{1z} is real and evanescent field radiated when k_{1z} imaginary value. Further importance of Eq. (2.74) and Eq. (2.75) is their direct applicability for several multilayer systems, even though, we showed for a system of dielectric-2D layer-dielectric system. To use the equation in multilayer system, see figure 2.4b; first, we determine the fields across various interface of each multilayer from the Green's tensor. This gives the different electric and magnetic field in each intermedia layer since it is only the decided by the location of the source of electromagnetic field. Then the fields at each interface can be connected by the boundary condition

to evaluate reflection coefficient and transmission coefficient. Then straightforward employ the transfer matrix to obtain the total reflection and transmission coefficient of the system. Finally substitute it in Eq. (2.74) and Eq. (2.75). Based on the schematics in figure 2.4b, the reflection coefficient for s- and p- polarization radiation we have showed in the previous section. Therefore, to evaluate the normalized SE rate of a double 2D conducting sheet and hyperbolic medium we only need to replace r_{12}^p and r_{12}^s by r_{123}^p and r_{123}^s, respectively.

References

[1] J. D. Jackson, Classical Electrodynamics. New York: Wiley, 2nd edn. (1975).

[2] P. Yeh, Optical Waves in Layered Media, Wiley-Interscience, Hoboken, New Jersey (2005).

[3] C.L. Cortes, W. Newman, S. Molesky, Z. Jacob, J. Opt. 14 (2012) 063001.

[4] D.R. Smith, D. Schurig, Electromagnetic Wave Propagation in Media with Indefinite Permittivity and Permeability Tensors, Phys. Rev. Lett. 90 (2003) 077405.

[5] P. A. D. Goncalves and N. M. M. R. Peres, An Introduction to Graphene Plasmonics (World Scientific, 2016).

[6] Rodríguez-Fortuño, F. J. & Zayats, A. V. Repulsion of polarised particles from anisotropic materials with a near-zero permittivity component. Light: Science & Applications 5, e16022 (2016).

[7] Maier SA. 2007 *Plasmonics: fundamentals and applications*. New York, NY: Springer Science+Business Media.

[8] Markoš, P. & Soukoulis, C. M. Wave Propagation: From Electrons to Photonic Crystals and Left-Handed Materials (Princeton University Press, Princeton, NJ, 2008).

[9] L. Novotny and B. Hecht, Principles of Nano-Optics (Cambridge University Press, Cambridge, 2006).

[10] G. W. Ford and W. H. Weber, "Electromagnetic interactions of molecules with metal surfaces," Phys. Rep. 113, 195–287 (1984).

[11] Purcell, E. M. Spontaneous Emission Probabilities at Radio Frequencies. Phys. Rev. 69, 674–702 (1946).

[12] Mandel L and Wolf E Optical Coherence and Quantum Optics 1995 (New York: Cambridge University) 1995.

Chapter 3

Material used in this chapter is compiled from Debu et al. previously published work [65].

Abstract

The adhesion layer used in nanofabrication process of metallic nanostructures affects the surface plasmon modes. We characterize the localized surface plasmon resonances (SPR) of gold nanodisks of various diameters and heights while varying the Ti adhesion layers thickness. Scattering, absorption, and extinction coefficient calculations show a significant dependence of the SPR on the size of nanostructures and the adhesion layer thickness. Comparisons of peak resonance wavelengths of different Ti adhesion layer thicknesses indicate a significant red shift and a reduction in amplitude as the Ti thickness increases. A comparison of spectral broadening of the plasmon mode indicates a linear increase with Ti thickness and percentage. In addition, the decay time of the plasmon mode decreased significantly as the adhesion layer size increases. These observations aid in understanding size dependent adhesion layer effects and optimized fabrication of single nanoplasmonic structures.

3.1 Introduction

When an electromagnetic wave is incident on a metal nanostructure, it induces collective coherent oscillations of conduction electrons on the surface of the metal, called surface plasmon resonances (SPRs). To support surface plasmons, the metal must have a dielectric constant with a negative real part and a small, positive imaginary part [1]. Materials that support SPRs in the visible and near infrared range of electromagnetic spectrum include copper, gold, and silver [2–4]. The surface plasmon resonance and the electric field enhancement have shown strong dependence on nanoparticle size [5–8], shape [6- 9], gap between dimers [7, 10–12], electromagnetic frequency

range [13, 14], and types of materials [15]. The surface plasmon modes show the decaying process that emerges from different sources that include radiative damping [16-17], nonradiative damping [16-18], surface scattering [19-22], and chemical interface/environment [23-24].

Fabrication of nanostructures made of noble metals using electron beam lithography on a glass substrate requires an adhesion layer such as Ti [26-29], Cr [25-29], or their oxide forms [30-32]. Significant effort has been made to understand the effects of adhesion layers on plasmon resonance as a source of chemical interface damping with an emphasis on periodic [32-33] or thin film structures [34]. Measurements of reflectance for gold split-ring periodic structures have indicated a red-shift in the resonance frequency due to the thin Ti adhesion layer [32]. Comparison of surface Raman resonance of periodic gold nano-cylinders with and without various adhesion layers (Ti, Cr, TiO_2, ITO, Cr_2O_3 and MPTMS) at a constant thickness indicates a reduction of the amplitude in the extinction spectra and in Surface Raman enhancement when adding these adhesion layers [35]. Analysis of the Au – Ti single nanorod demonstrated a drastic decrease in field enhancement and an increase of decaying time (dephasing time) in comparison with a pure gold nanorod [36]. The presence of a Ti adhesion layer has been shown change nonlinearly the line broadening, and peak wavelength as a function of Ti% and also reduce the acoustic vibration damping time in Au nanodisks using single-particle transient extinction spectroscopy [37].

There are few studies that investigate adhesion layer damping of plasmon resonances in single nanoparticles from a simulation perspective. In this paper, we use a finite element simulation method to demonstrate surface plasmon damping changes due to thickness and percentage change of Ti adhesion layer on single Au nanodisks of various sizes. Results from this work expand on previously explanations of layer interfaces altering resonance positions and broadening spectra.

We also use the results to model the dependence of the plasmon linewidth as a function of adhesion layer thickness and percentage in order to quantitatively describe dephasing time.

3.2 Finite element method

1. Method

Finite element method (FEM) [38, 39] simulations were conducted to solve the wave vector form of the time-dependent harmonics electric field [40]:

$$\nabla \times \left(\frac{1}{\mu_r}\nabla \times \boldsymbol{E}\right) - k_0^2 \varepsilon_r \boldsymbol{E} = 0, \tag{3.1}$$

Where $\boldsymbol{E} = E_x \hat{x} + E_y \hat{y} + E_z \hat{z}$ is the electric field, $k_0 = 2\pi/\lambda$ is the incident electric field propagation wave vector of wavelength λ, and ε_r and μ_r are relative permittivity and permeability, respectively. In the simulation, near-field and far-field results of a gold nanodisk with a thin titanium adhesion layer of the same diameter surrounded by an effective medium are determined. For the far field, the normalized scattering efficiency, Q_{scat} is obtained by integrating the time averaged power flow on a surface far from the nanoparticles as [41, 42]

$$S_{scat} = \frac{1}{2}\text{Re}\{\boldsymbol{E}_{scat} \times \boldsymbol{H}_{scat}^*\} \tag{3.2}$$

$$Q_{scat} = \frac{\iint S_{scat} d\boldsymbol{A}}{\pi r^2 |I_0|} \tag{3.3}$$

Where $\boldsymbol{E}_{scat}$ and $\boldsymbol{H}_{scat}$ are the scattered electric field and magnetic field, respectively. Q_{scat} is the normalized scattering efficiency, r is the radius of the nanodisk, A is an arbitrary boundary surrounding the gold nanodisk, $|I_0| = 1/2c\varepsilon_0\varepsilon_r E_0^2$ is the intensity of the incident wave $\boldsymbol{E}_0$, and c is

the speed of light. The normalized absorption efficiency, Q_{scat}, is determined from the fraction of integrated resistive heating over the nanodisk volume V divided by the incident power density:

$$Q_{abs} = \frac{2}{\pi r^2 |I_0|} \iint \mathrm{Re}(\boldsymbol{J}_{tot} \cdot \boldsymbol{E}_{tot}^* + i\omega \boldsymbol{B}_{tot} \cdot H_{tot}^*) d\boldsymbol{V} \tag{3.4}$$

where J_{tot} is the total electrical current density. Inside the integral, the first part of the sum represents resistive loss (Joule heating) and the second part represents the magnetic loss. The summation of Q_{scat}, and Q_{abs}, is defined as the extinction efficiency, $Q_{ext} = Q_{abs} + Q_{scat}$.

To investigate the adhesion layer, we considered gold nanodisks with diameter D ranging from 75 − 200 nm. The thickness of the gold nanodisk, t_{Au}, varied from 10 − 15 nm, which is below the skin depth in the optical and infrared region. We also modeled some disks to have a Ti adhesion layer with a thickness, t_{Ti}, ranging from 1 − 5 nm. As data for the dielectric constants as a function of wavelength are not available for all wavelengths of light used in this paper, interpolated dielectric constants of gold and titanium obtained from [43, 44] were used. The incident light amplitude was set to 1 V/m, polarized in the x-direction, and propagating parallel to the axis of the nanodisk placed in the x-y plane. Fabricated nanostructure usually includes base substrates such as glass. The top half part of the simulation is considered air and the bottom half space is considered glass. The surrounding dielectric environment is treated by effective relative dielectric constant [45], $\varepsilon_{eff} \approx (\varepsilon_{air} + \varepsilon_{glass})/2 = 1.25$. Q_{scat} from the far field is evaluated on an imaginary spherical surface at a distance larger than half of the wavelength of the incident field enclosing the nanostructures. A perfectly matched layer (PML) surface of thickness 250 nm enclosing the imaginary surface was used as an outer boundary to avoid any backscattering.

3.2 Results and discussions

Next, to understand more the effect of the Ti adhesion layer the smallest nanodisk (75 nm) based figure 3.1, the results are plotted in figure 2, is considered. A fixed diameter of 75 nm was used,

with t_{Ti} changing from $0 - 5$ nm with an increment of 1 nm. The total thickness, t_{tot}, varies from 15 to 20 nm as t_{Ti} increases since $t_{tot} = t_{Au} + t_{Ti}$. The disks in 2(a) indicate what ideal nanofabricated structures looks like.
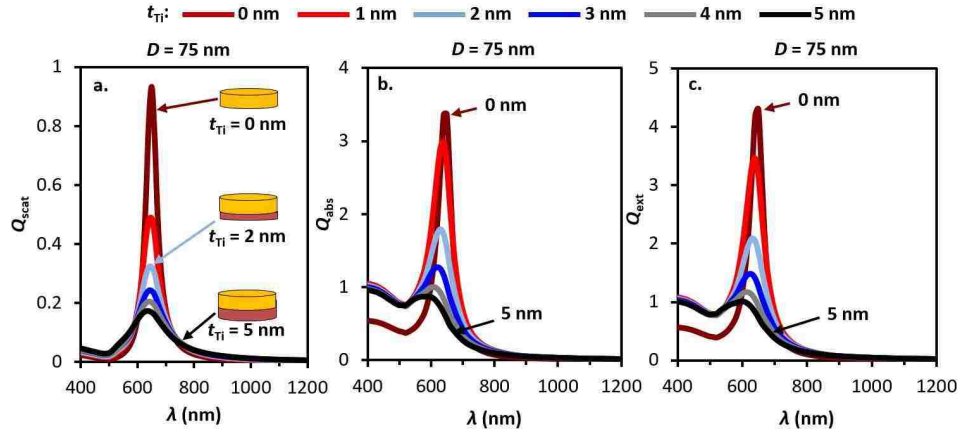

Fig. 3.1. Spectrum for various t_{Ti} when $t_{Au} = 15$ nm $D = 75$ nm. (a) Calculated scattering spectra. Calculated (b) absorption spectra and (c) extinction spectra for the same parameters as in (a) [65].

The peak position of the Q_{scat} spectra in 3.2(a) does not change, but it does slightly broaden and the amplitude decreased as t_{Ti} increases. Comparing the amplitude of the spectra, the absorption Q_{abs} is the dominant source for the extinction. For some structures, the amplitude of the efficiency reaches values that are larger than one. This is possible since the plasmonic nanodisks draw in light from an area significantly larger than their surface area [46]. This effect occurs due to a strong resonant interaction between the collective oscillations of electrons in the nanostructure and the incident light. These results demonstrate that the surface plasmon resonance wavelength, as well as the extent of the plasmon enhancement, is highly dependent on the size and shape of the structure [47-50]. Increasing t_{Ti} blue shifts Q_{abs} and Q_{ext} by about 50 nm, a trend not shared by the Q_{scat} resonance figure 3.2(a). This difference arises because scattering integrates the far field signal that predominantly originates from the surface of the Au while absorption measures the near field contribution that comes from both from Au and Ti [51]. This can be explained by the effective

33

medium determined by the real and imaginary part of the dielectric constant of Au and Ti. At resonant wavelength when $t_{Ti} = 0$ nm and $t_{Au} = 15$ nm, $\varepsilon_{Au} = -11.26 + 1.33i$ and $\varepsilon_{Ti} = -5.06 + 12.52i$. Approximate regarding Au and Ti nanodisk effective medium by the volume aspect ratio. $\varepsilon_{Ti+Au} = \varepsilon_{Ti} t_{Ti} + \varepsilon_{Au} t_{Au}/(t_{Ti} + t_{Au})$. The significant increase in effective dielectric constant as shown in figure 2(b-c) results in the resonance shift of the absorption and extinction efficiency.
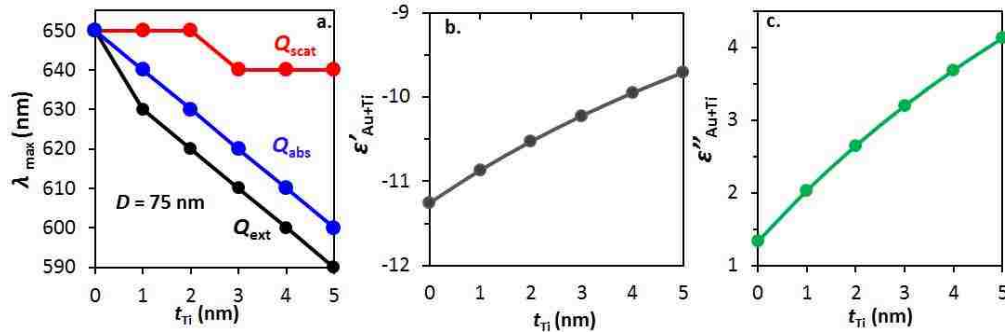
Fig. 3.2. (a) Peak resonance wavelength for scattering, absorption and extinction spectra for $D = 75$ nm disk with $t_{Au} = 15$ nm as a function of t_{Ti}. Effective (b) real and (c) imaginary dielectric calculated from the volume fraction of Au and Ti [65].

In addition, increasing t_{Ti} results in significant broadening of the spectra as well as a decrease in the amplitudes. These results are useful in understanding the role of the absorptive adhesion layer on the impact on the surface plasmonic response of noble metals, thus allowing for easy optical tunability.

34

Fig. 3.3. Comparison of the peak amplitude of spectra for various disk diameters with $t_{Au} = 15$ nm. Maximum (a) absorption coefficient, (b) scattering coefficient and (c) extinction coefficient as a function of t_{Ti}. (d-f) are similar results from above but include more values for D [65].
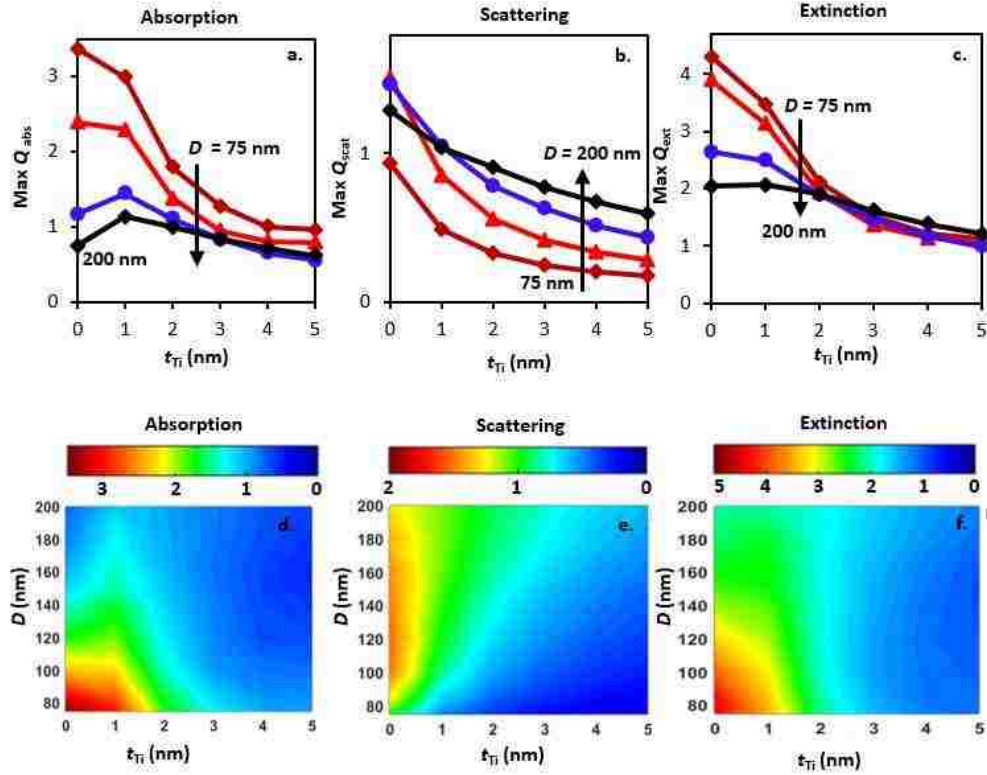
The graph in figure 3.3 shows the maximum values of Q_{abs}, Q_{scat} and Q_{ext} for four diameters (75, 100, 140, and 200 nm) as a function of t_{Ti}. These results indicate that the Q_{scat} peak value, which is a measure of the enhancement factor [52], decreases independently of the size as t_{Ti} increases. Such a reduction of the near-field amplitude has been reported; the presence of a Ti or Cr adhesion layer results in a reduced fluorescence signal enhancement [30] and dark-field scattering measurements [36]. Q_{abs} peak amplitude shows strong decrement for the same t_{Ti} as the diameter changes. Small Au nanodisks have larger amplitude peak values than the bigger Au nanodisks. This trend is the opposite in the maximum amplitude of the Q_{scat} spectra. Result from amplitude of Q_{ext} shows similar trend as Q_{abs}. In particular, the peak value is strongly affected for t_{Ti} up to 2 nm. Results for each diameter in this study are included in the interpolated color plot figure 3.3

(d), (e) and (f). The values obtained in figure 3.3 (d), (e) and (f) are generally consistent with the four selected diameter figure 3.3 (a), (b) and (c), indicating that, in addition to peak broadening, the plasmonic scattering, absorption, and extinction peak amplitude response is also highly influenced by the thickness of Ti adhesive layer.

The peak resonance wavelength (λ_{max}) from the simulated Q_{scat} spectra for Au nanodisks of $D =$ 75, 100, 140, 160, and 200 nm and t_{Ti} ranging from 0 to 5 nm are illustrated in figure 3.4 (a). For a nanodisk with a $t_{Au} = 15$ nm and a fixed t_{Ti}, the resonance peak blue-shifts as D decreases as shown in figure 3.4(a). As t_{Ti} increases, for $D = 75$ nm and $D = 100$ nm the peak resonance dropped by ~ 50 nm. But for $D = 140$ nm, 160 nm, and 200 nm, the peak position was not altered independently of the Ti layer. Thus, as the particles become smaller, the effect of the Ti layer becomes more pronounced on the peak resonance.
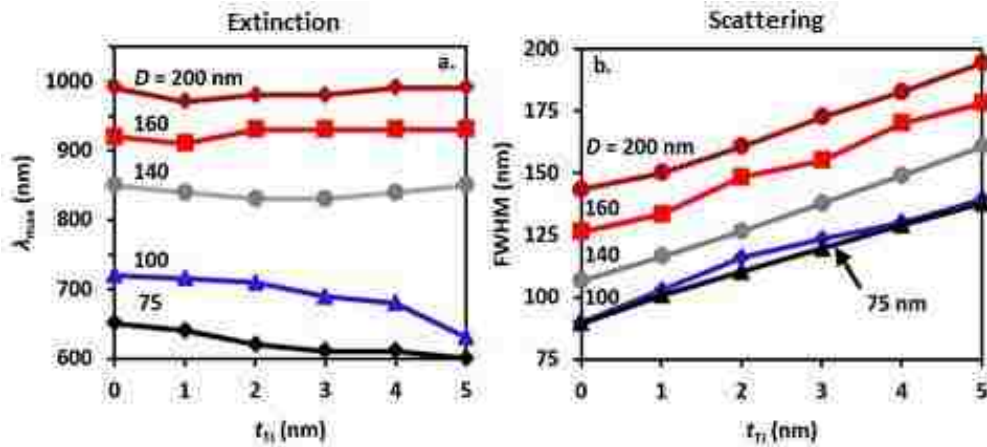

Fig. 3.4. The comparison of peak resonance mode and linewidth of gold nanodisks as a function of t_{Ti}. (a) The comparison of the peak resonance of five diameters obtained from extinction efficiency spectra. (b) FWHM calculated from the Q_{scat} spectra as a function of t_{Ti}. Linewidths of the gold nanodisks are extracted by fitting Gaussian functions to the scattering spectra [65].

3.3.1 Spectral broadening

In order to characterize the profiles of the spectra, we now consider the plasmon resonance width, an important parameter in fully characterizing the behavior of an oscillatory system at the resonance position. The plasmon resonance width is the full width at half maximum (FWHM) of the spectrum. The shape of the peaks of the spectrum unveils the plasmon mode damping characteristics. Larger damping is manifested as a broad Lorentzian peak that follows the Lorentz-Drude profile of the dielectric constant. The exact information on plasmon broadening is obtained by fitting a Gaussian profile from the Q_{scat} spectra [53-55]. This width is plotted versus t_{Ti} for various diameters in figure 3.4(b); the width increases linearly as t_{Ti} increases. A simple empirical model fits a linear equation obtained from the graph, $\Delta\lambda_{res} = \Delta\lambda_0 + mt_{Ti}$, where $\Delta\lambda_{res}$ is the change in the FWHM for a given nanodisk diameter, $\Delta\lambda_0$ is the FWHM without Ti, and m is the proportionality constant. The major result from the fitting is that m is almost constant at $m = \sim 10.2$, independent of D. Narrower linewidth is obtained without the adhesion layer and broader width when there is an adhesion layer. The FWHM is as small as 80 nm for nanodisks with diameters of $\sim$ 85 nm, and 140 nm for a nanodisk with $D = 200$ nm with no adhesion layer. This shows the FWHM increases with the D, for each t_{Ti}. Overall, these results show that the Ti adhesion layer greatly affects the surface plasmon resonance bandwidths of nanostructures. Thus, the Ti adhesion layer can significantly broaden the surface plasmon resonance bandwidth due to the additional absorption in the Ti layer.
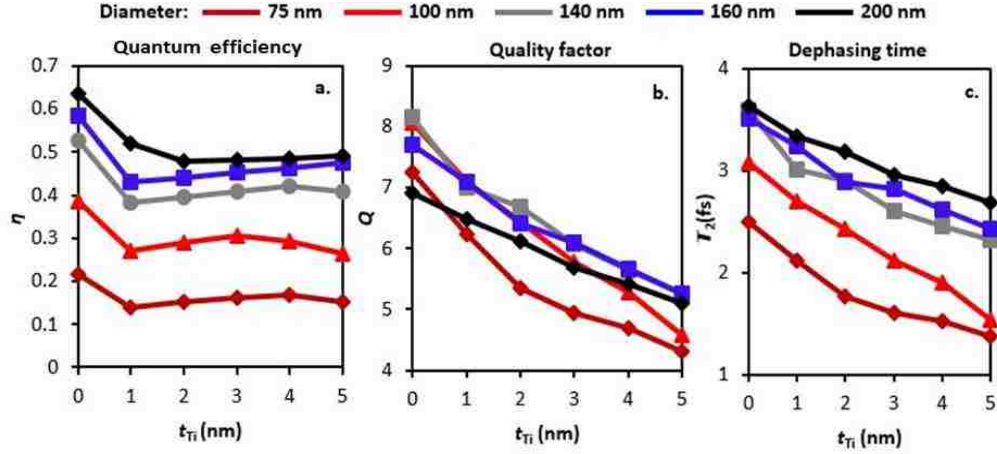
Fig. 3.5. Calculated broadening and damping parameters of nanodisks with t_{Au} = 15 nm as a function of t_{Ti} for all considered diameters. (a) quantum efficiency (yield), (b) quality factor, and (c) plasmon modes dephasing (decay) time [65].

The quantum efficiency (η), which is defined as the ratio of Q_{scat} to Q_{ext} at their respective resonance wavelengths, increases with increasing diameters for each t_{Ti} as shown in figure 3.5 (a). Without a Ti layer, the efficiency is ~ 0.217 for D = 75 nm and 0.635 when D = 200 nm. This increase of the quantum efficiency is due to increases in the absorption efficiency for the larger size resulting from the increases of the imaginary part of the dielectric constant of Au since the larger D results in a larger resonance wavelength. According to [56-60], studies of multiple nanoparticles showed that η depends on geometrical parameters such as aspect ratios and sizes of gold nanoparticles. The result of η for t_{Ti} = 0 ranges from 0.2 – 0.65. This matches well with other results for Au nanostructures [56-60]. The major impact is that adding 5 nm of Ti decreases η by ~0.1 for all diameters. This is due to the imaginary part of the dielectric of Ti causing additional absorption.

3.3.2   Plasmon spectra quality factor and dephasing time

Another parameter that is commonly used to quantify the damping of surface plasmon resonance is the quality factor, or Q-factor. The quality factor is defined as the energy E stored

38

in an oscillator, divided by the energy dissipated per solid-angle radian of the integration space. In terms of the peak wavelength's resonance energy, E_{res}, and the energy of full-width of the plasmon peak at half its maximum amplitude, Γ, the quality factor is given as ($Q = E_{res}/\Gamma$). Besides determining the number of oscillations until the oscillation is damped Q further elaborates, indirectly, the effect of an adhesion layer on the field enhancement. Figure 3.5(b) shows the quality factor as a function of the t_{Ti} for five selected diameters Q decreases by ~3 when the t_{Ti} increases from 0 to 5 nm.

So far, the qualitative approach implemented to analyze the decay mechanism has relied on characteristics without explanation of specific details of the physics behind the possible decay dynamics and sources. Several factors contribute to plasmon dephasing; it can reasonably be assumed that each term of the line broadening effects is independent and hence the aggregate impacts are quantified by writing the plasmon linewidth Γ as a sum of several plasmon damping terms contributions as [24, 61-62]

$$\Gamma = \gamma_b + \Gamma_{rad} + \Gamma_{e-surf} + \Gamma_{interface} \tag{3.5}$$

where γ_b, Γ_{rad}, and Γ_{e-surf}, $\Gamma_{interface}$ correspond to bulk damping, radiation damping, damping due to electron surface scattering, and damping due to interfacial effects, respectively. The bulk damping term γ_b originates from electron scattering in the metal and is characteristic of the material. It is well described by the complex dielectric function of the metal and is therefore frequency dependent. The second term in Eq. 3.5 describes the energy loss mechanism due to the coupling of the plasmon oscillation to the radiation field, also known as radiation damping. The Γ_{e-surf} shows significant dependence on the size of the Au nanodisks. As smaller sized nanodisks become shorter than the electron mean free path, the predominant damping contribution comes from electron surface scattering. The last term in Eq (3.5), $\Gamma_{interface}$, is solely dependent on the

surrounding environment of the dielectric metal. In our case this is the Ti adhesion layer contributing in the form of chemical interface damping which leads to a dephasing time T_2, which includes all the possible parameters of surface plasmon resonance damping sources. The effect of the dielectric substrate, in this study the effective medium (air+quartz), is negligible when the permittivity doesn't have a loss factor. Finite-difference time-domain (FDTD) calculations and experimental values of linewidth for gold nanorods on quartz in [62] showed consistent results; interface damping due to charge interactions between the gold nanorods and quartz is ruled out as an additional contribution to the plasmon linewidth, in agreement with the results from the quasi-static model. T_2 is the period in which the plasmon amplitude has decayed to $1/e$ times its maximum value. From the individual Au nanodisk homogeneous linewidth (Γ) obtained from the spectra, the dephasing time is obtained using the relation $T_2 = 2\hbar/\Gamma$ [63-64]. According to figure 3.5(c), there are two important outcomes to be noticed. First, for a fixed diameter the dephasing time decreases as t_{Ti} gets larger. The smaller Au nanodisks show significantly larger changes in comparison to the larger Au nanodisks. In addition, as D gets above 140 nm, the dephasing time for t_{Ti} up to 2 nm shows nearly equal values. The second result is that for the same t_{Ti} the value of T_2 for larger nanodisks is greater than that of small nanodisks. This is a good indication of how the Ti adhesion layer affects the oscillations, increasing the absorption of the enhanced plasmon field as well as the field that did not get attenuated in the Au disk.

In order to gain more insight into the effects of the adhesion layer, we followed a second approach wherein we gradually increase the percentage of titanium, Ti%, from 0% to 33%, while the total thickness is fixed, $t_{tot} = t_{Au} + t_{Ti} = 15$ nm. According to Figure 6(a), λ_{max} gradually shifts to a longer wavelength when the Ti% increases from 0% to 33% while such consistency has not been observed in case of a fixed Au thickness, Figure 3.2(a). This indicates the resonance wavelength varies with

the thickness of the Au for nanodisks. Calculations show that plasmon resonance linewidth broadens as the Ti% increases, as illustrated in Figure 3.6(b); these results are similar to those in Figure 2(b).
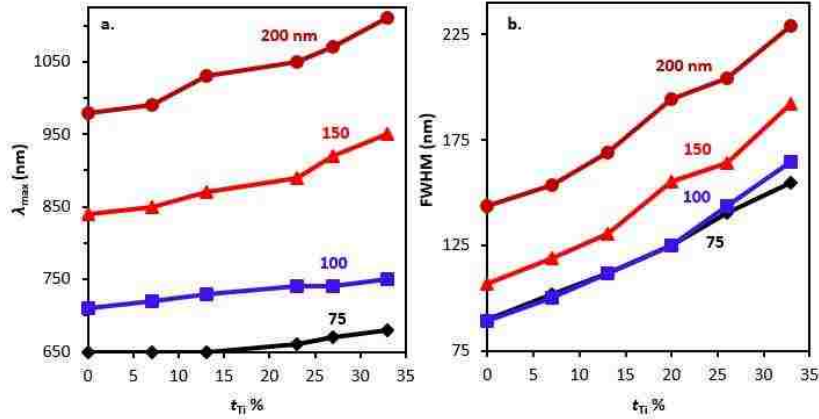
Fig. 3.6. Calculated peak plasmon resonance wavelength (a) and the full width at half maxima (FWHM) (b) of nanodisks as a function of Ti% for four selected diameters, 75 nm, 100 nm, 150 nm and 200 nm [65].
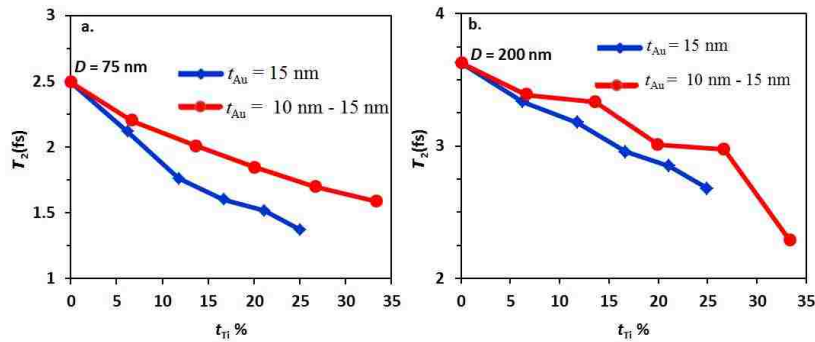
Fig. 7. Calculated dephasing time of nanodisks of diameter of 75 nm (a) and 200 nm (b) as a function of Ti% [65].

Figure 3.7 shows the dephasing time of Au nanodisks of diameter 75 nm and 200 nm for the two cases. In the first case, which is indicated in blue for both figures, the thickness of gold was kept constant at t_{Au} = 15 nm. The Ti thickness was increased from 1 – 5 nm, thereby varying the percentage from 5% to 25%. In both conditions, the dephasing time decreases up to ~ 40%

41

with the increase of Ti%. These results illustrate the addition of Ti layer facilitates the decaying of the SPRs mode faster as a chemical interface damping source.

3.4 Conclusions

Surface plasmon resonances of individual Au nanodisks were investigated as a function of t_{Ti} from a simulation perspective. Results from our techniques characterize the values η, Q, and T_2 as a function of t_{Ti} allowing one to control these parameters by adjusting t_{Ti}. We observed a strong dependence of the surface plasmon resonance on the size of the particles. Strong spectral broadening and reduced field enhancement when using titanium adhesion layers were observed as well. The broadening reveals that there is a linear relation with the thickness or percentage of the adhesion layer. Field enhancement evaluated from the quality factor deteriorates as Ti% increases. The imaginary component of permittivity for Ti contributes more significantly to the loss factor than that of Au. The spectral decaying mode that is related to the dephasing time decreases significantly with t_{Ti}. These are due to charge interactions between the Ti layer and Au nanodisk electron screening process, which creates chemical interface damping. The results in this work provide a useful tool for optimizing a nanofabrication process that includes adhesion layers on a dielectric substrate with controlled size and shape.

References

1. K. A. Willets and R. P. Van Duyne, "Localized surface plasmon resonance spectroscopy and sensing," Annu. Rev. Phys. Chem. **58**(1), 267–297 (2007).

2. E. Hutter, J. H. Fendler, and D. Roy, "Surface plasmon resonance studies of gold and silver nanoparticles linked to gold and silver substrates by 2-aminoethanethiol and 1,6-hexanedithiol," J. Phys. Chem. B **105**(45), 11159–11168 (2001).
3. K. T. Yong, Y. Sahoo, M. T. Swihart, P.N. Prasad, "Synthesis and plasmonic properties of silver and gold nanoshells on polystyrene cores of different size and of gold–silver core–shell nanostructures," Colloids and Surfaces A: Physicochemical and Engineering Aspects **290**(1), 89–105 (2006).

4. J. E. Millstone, S. J. Hurst, G.S. Métraux, J. I. Cutler, C. A. Mirkin, Colloidal gold and silver triangular nanoprisms, Small, **5** (6), 646–664 (2009).

5. P. Mühlschlegel, H. Eisler, O. Martin, B. Hecht, and D. Pohl, "Resonant optical antennas," Science **308**(5728), 1607–1609 (2005).

6. H. Fischer and O. J. Martin, "Engineering the optical response of plasmonic nanoantennas," Opt. Express **16**(12), 9144–9154 (2008).

7. T. Hanke, G. Krauss, D. Träutlein, B. Wild, R. Bratschitsch, and A. Leitenstorfer, "Efficient nonlinear light emission of single gold optical antennas driven by few-cycle near-infrared pulses," Phys. Rev. Lett. **103**(25), 257404 (2009).

8. J. C. Prangsma, J. Kern, A. G. Knapp, S. Grossmann, M. Emmerling, M. Kamp, and B. Hecht, "Electrically connected resonant optical antennas," Nano Lett. **12**(8), 3915–3919 (2012).

9. C. S̈onnichsen, T. Franzl, T. Wilk, G. von Plessen, J. Feldmann, O. Wilson, and P. Mulvaney, "Drastic reduction of plasmon damping in gold nanorods," Phy. Rev. Lett. **88**(7), 77402 (2002).

10. D. Fromm, A. Sundaramurthy, P. Schuck, G. Kino, and W. Moerner, "Gap-dependent optical coupling of single bowtie nanoantennas resonant in the visible," Nano Lett. **4**(5), 957–961 (2004).

11. P. Schuck, D. Fromm, A. Sundaramurthy, G. Kino, and W. Moerner, "Improving the mismatch between light and nanoscale objects with gold bowtie nanoantennas," Phys. Rev. Lett. **94**(1), 17402 (2005).

12. J. Merlein, M. Kahl, A. Zuschlag, A. Sell, A. Halm, J. Boneberg, P. Leiderer, A. Leitenstorfer, and R. Bratschitsch, "Nanomechanical control of an optical antenna," Nat. Photonics **2**(4), 230–233 (2008).

13. J. Rivas, M. Kuttge, P. Bolivar, H. Kurz, and J. S´anchez-Gil, "Propagation of surface plasmon polaritons on semiconductor gratings," Phys. Rev. Lett. **93**(25), 256804 (2004).

14. A. P. Hibbins, B. R. Evans, and J. R. Sambles, "Experimental verification of designer surface plasmons," Science **308**(5722), 670–672 (2005).
15. F. Wang and Y. Shen, "General properties of local plasmons in metal nanostructures," Phys. Rev. Lett. **97**(20), 206806 (2006).

16. A. Wokaun, J. Gordon, and P. Liao, "Radiation damping in surface-enhanced Raman scattering," Phys. Rev. Lett. **48**, 957–960 (1982).

17. N. I. Grigorchuk, "Radiative damping of surface plasmon resonance in spheroidal metallic nanoparticle embedded in a dielectric medium," J. Opt. Soc. Am. B **29**(12), 3404-3411 (2012).

18. K. Kolwas and A. Derkachova, "Damping rates of surface plasmons for particles of size from nano- to micrometers; reduction of the nonradiative decay," J. Quant. Spectrocs. Radiat. Transfer **114**, 45–55 (2013).

19. R. Carmina Monreal, S. Peter Apell, and T. Antosiewicz, "Surface scattering contribution to the plasmon width in embedded Ag nanospheres," Opt. Express **22**(21), 24994-25004 (2014).

20. K. Fuchs, "The conductivity of thin metallic films according to the electron theory of metals," Proc. Cambridge Philos. Soc. **34**, 100–108 (1938).

21. P. Apell, R. Monreal, and F. Flores, "Effective Relaxation-Time in Small Spheres: Diffuse Surface Scattering," Solid State Commun. **52**(12), 971– 973 (1984).

22. H. Hövel, S. Fritz, A. Hilger, U. Kreibig, and M. Vollmer, "Width of cluster plasmon resonances: bulk dielectric functions and chemical interface damping," Phys. Rev. B **48**, 18178 (1993).

23. C. Hendrich, J. Bosbach, F. Stietz, F. Hubenthal, T. Vartanyan, and F. Trager, "Chemical interface damping of surface plasmon excitation in metal nanoparticles: A study by persistent spectral hole burning," Appl. Phys. B **76**, 869–875 (2003).

24. P. Zijlstra, P. M. R. Paulo, K. Yu, and M. Orrit, "Chemical interface damping in single gold nanorods and its near elimination by tip-specific functionalization," Angew. Chem. Int. Ed. **51**, 8352-8355 (2012).

25. B. Lahiri, S. G. McMeekin, R. M. De La Rue, and N. P. Johnson, "Resonance hybridization in nanoantenna arrays based on asymmetric split-ring resonators," Appl. Phys. Lett. **98**, 153116 (2011).

26. B. Lahiri, R. Dylewicz, R. M. D. L. Rue, and N. P. Johnson, "Impact of titanium adhesion layers on the response of arrays of metallic split-ring resonators (SRRs)," Opt. Express **18**(11), 11202–11208 (2010).

27. B. Lahiri, A. Z. Khokhar, R. M. De La Rue, S. G. McMeekin, and N. P. Johnson, "Asymmetric split ring resonators for optical sensing of organic materials," Opt. Express **17**(2), 1107–1115 (2009).

28. S. J. Bauman, E. C. Novak, D. T. Debu, D. Natelson, and J. B. Herzog, "Fabrication of sub-lithography-limited structures via nanomasking technique for plasmonic enhancement applications," IEEE Trans. Nanotechnol. **14**, 790–793 (2015).

29. S. J. Bauman, D. T. Debu, and J. B. Herzog, "Plasmonic structures fabricated via nanomasking sub-10 nm lithography technique", Proc. SPIE **9556**, 95560M (2015).

30. H. Aouani, J. Wenger, D. Gerard, H. Rigneault, E. Devaux, T.W. Ebbesen, F. Mahdavi, T. Xu, and S. Blair "Crucial role of the adhesion layer on the plasmonic fluorescence enhancement," ACS Nano **3**, 2043–2048 (2009).

31. X. Jiao, J. Goeckeritz, S. Blair, and M. Oldham, "Localization of near-field resonances in bow-tie antennae: influence of adhesion layers," Plasmonics **4**, 37–50 (2009).

32. C. Jeppesen, N. A. Mortensen, and A. Kristensen, "The effect of Ti and ITO adhesion layers on gold split-ring resonators," Appl. Phys. Lett. **97**(26), 263103 (2010).

33. Y. Chen, Z. Li, Q. Xiang, Y. Wang, Z. Zhang, and H. Duan, "Reliable fabrication of plasmonic nanostructures without an adhesion layer using dry lift-off," Nanotechnology **26**(40), 405301 (2015).

34. P. Jahanshahi, M. Ghomeishi and F. R. M. Adikan, "Adhesive layer effect on gold-silica thin film interfaces for surface plasmon resonance modeling," *2012 IEEE 3rd International Conference on Photonics*, Penang, 2012, pp. 89-92.

35. Colas Florent, Barchiesi D., Kessentini S., Toury T., De La Chapelle M. Lamy, "Comparison of adhesion layers of gold on silicate glasses for SERS detection," Journal Of Optics, **17**(11), 1-7 (2015).

36. T. G. Habteyes, S. Dhuey, E. Wood, D. Gargas, S. Cabrini, P. J. Schuck, A. P. Alivisatos, and S. R. Leone, "Metallic adhesion layer induced plasmon damping and molecular linker as a nondamping alternative," ACS Nano **6**(6), 5702–5709 (2012).

37. W. Chang, F. Wen, D. Chakraborty, M. Su, Y. Zhang, et al. "Tuning the acoustic frequency of a gold nanodisk through its adhesion layer" *Nat. Commun.,***6***, 7022 (2015).*

38. J. Jin, *The Finite Element Method in Electromagnetics* (John Wiley and Sons, New York, 2002).

39. K. L. Wustholz, A. I. Henry, J. M. McMahon, R. G. Freeman, N. Valley, M. E. Piotti, M. J. Natan, G. C. Schatz, and R. P. Van Duyna, "Structure-Activity Relationships in Gold Nanoparticle Dimers and Trimers for Surface-Enhanced Raman Spectroscopy," J. Am. Chem. Soc. **132**(31), 10903-10910(2010).

40. COMSOL, "COMSOL Multiphysics version 4.4," (COMSOL RF, 2014).

41. C. F. Bohren and D. R. Huffman, *Absorption and Scattering of Light by Small Particles* (Wiley, New York, 1983).

42. V. Giannini, A. I. Fernández-Domínguez, S. C. Heck, and S. A. Maier, "Plasmonic nanoantennas: fundamentals and their use in controlling the radiative properties of nanoemitters," Chem. Rev.**111**, 3888–3912 (2011).

43. P. B. Johnson and R. W. Christy, "Optical constants of noble metals," Phys. Rev. B **6**, 4370–4379 (1972).

44. E. D. Palik, *Handbook of Optical Constants of Solids* (Academic Press, New York, 1985).

45. D. Barchiesi, S. Kessentini, N. Guillot, M. L. de la Chapelle, and T. Grosges, "Localized surface plasmon resonance in arrays of nano-gold cylinders: inverse problem and propagation of uncertainties," Opt. Express **21**(2), 2245–2262 (2013).

46. R. K. Harrison and A. Ben-Yakar, "Point-by-point near-field optical energy deposition around plasmonic nanospheres in absorbing media," J. Opt. Soc. Am. **A 8**(32), 1523-1535 (2015).

47. U. Kreibig and M. Vollmer, Optical Properties of Metal Clusters (Springer, New York, 1995).

48. M. J. Feldstein, C. D. Keating, Y. H. Liau, M. J. Natan, and N. F. Scherer, "Electronic relaxation dynamics in coupled metal particle," J. Am. Chem. Soc. **119**, 6638-6646 (1997).

49. Grant, A. M. Schwartzberg, T. J. Norman and J. Z. Zhang, "Ultrafast electronic relaxation and coherent vibrational oscillation of strongly coupled gold nanoparticle aggregates," J. Am. Chem. Soc. **125**, 549–553 (2003).

50. J. Turkevich, P. C. Stevenson, and J. Hillier, "A study of the nucleation and growth processes in the synthesis of colloidal gold," Discuss. Faraday Soc. **11**, 55–75 (1951).

51. T. Okamoto, "Near-field spectral analysis of metallic beads," Topics Appl. Phys. **81**, 97–123 (2001).
52. B. J. Messinger, K. U. Vonraben, R. K. Chang, and W. P. Barber, "Local-Fields at the Surface of Noble-Metal Microspheres," Phys. Rev. **B** 24, 649– 657 (1981).

53. D.u Zhu, A. Tang, H. Ye, M. Wang, C. Yang and F. Teng , ''Tunable near-infrared localized surface plasmon resonances of djurleite nanocrystals: effects of size, shape, surface-ligands and oxygen exposure time,'' J. Mater. Chem. C, **3**, 6686-6691 (2015).

54. R. G. Hobbs, V. R. Manfrinato, Y. Yang, S. A. Goodman, L. Zhang, E. A. Stach, and K. K. Berggren, ''High-Energy Surface and Volume Plasmons in Nanopatterned Sub-10 nm Aluminum Nanostructures,'' *Nano Letters* **16** (7), 4149-4157 (2016).

55. B. S. Dennis, D. A. Czaplewski, M. I. Haftel, D. Lopez, G. Blumberg, and V. Aksyuk, "Diffraction limited focusing and routing of gap plasmons by a metal-dielectric-metal lens," Opt. Express **23**(15), 21899-21908 (2015).

56. J. Balbus, R. Denison, K. Florini, and S. Walsh, "Getting Nanotechnology Right the First Time," Issues in Science and Technology 65-71 (2005).

57. I. El-Sayed, X. Huang, and M. El-Sayed "Selective laser photo-thermal therapy of epithelial carcinoma using anti-EGFR antibody conjugated gold nanoparticles," Cancer Lett. 239, 129–35 (2006).

58. J. M. Stern, J. Stanfield, W. Kabbani, J.-T. Hsieh, and J. A. Cadeddu, "Selective prostate cancer thermal ablation with laser activated gold nanoshells," J. Urol. **179**(2), 748–753 (2008).

59. C. C. Chen, Y. P. Lin, C. W. Wang, H. C. Tzeng, C. H. Wu, Y. C. Chen, C. P. Chen, L. C. Chen, and Y. C. Wu, "DNA-gold nanorod conjugates for remote control of localized gene expression by near infrared irradiation," J. Am. Chem. Soc. **128**(11), 3709–3715 (2006).

60. K. S. Lee and M. A. El-Sayed, "Dependence of the enhanced optical scattering efficiency relative to that of absorption of gold metal nanorods on aspect ratio, size, end-cap shape, and medium refractive," J. Phys. Chem. B **109**, 20331–20338 (2005).

61. G. V. Hartland, "Optical studies of dynamics in noble metal nanostructures," Chem. Rev. **111**(6), 3858–3887 (2011)

62. A. Hoggard, L.-Y. Wang, L. Ma, Y. Fang, G. You, J. Olson, Z. Liu, W.-S. Chang, P. M. Ajayan, and S. Link, "Using the plasmon linewidth to calculate the time and efficiency of electron transfer between gold nanorods and graphene," ACS Nano **7**, 11209–11217 (2013).

63. S. Link and M. A. El-Sayed, "Spectral properties and relaxation dynamics of surface plasmon electronic oscillations in gold and silver nanodots and nanorods," J. Phys. Chem. B **103** 8410–26 (1999).

64.M. Bosman, E. Ye, S. F. Tan, C. A. Nijhuis, J. K. W. Yang, R. Marty, A. Mlayah, A. Arbouet, C. Girard, and M. Y. Han, "Surface Plasmon Damping Quantified with an Electron Nanoprobe," Sci. Rep. **3**, 1312 (2013).

65.D. T. Debu, P. Ghosh, D. French, and J. B. Herzog, "Surface plasmon damping effects due to Ti adhesion layer in individual gold nanodisks", Optical Materials Express, 7(1), 73-84 (2016).

Chapter 4 Tuning Infrared Plasmon Resonance of Black Phosphorene

Material used in this chapter is compiled from Debu et al. previously published work [64].

Abstract

We report on the tunable edge-plasmon-enhanced absorption of phosphorene nanoribbons supported on a dielectric substrate. Monolayer anisotropic black phosphorous (phosphorene) nanoribbons are explored for light trapping and absorption enhancement on different dielectric substrates. We show that these phosphorene ribbons support infrared surface plasmons with high spatial confinement. The peak position and bandwidth of the calculated phosphorene absorption spectra are tunable with low loss over a wide wavelength range via the surrounding dielectric environment of the periodic nanoribbons. Simulation results show strong edge plasmon modes and enhanced absorption as well as a red-shift of the peak resonance wavelength. The periodic Fabry-Perot grating model was used to analytically evaluate the absorption resonance arising from the edge of the ribbons for comparison with the simulation. The results show promise for the promotion of phosphorene plasmons for both fundamental studies and potential applications in the infrared spectral range.

4.1 Introduction

Studies of the light-matter interaction have been conducted for many materials, commonly focusing on noble metal films and nanostructures. Noble metals (gold, silver, etc.) support strong surface plasmon confinement. Surface plasmons are collective wave modes of conduction band electron oscillations at the interface between two materials; the waves are coherent with an incident oscillating electromagnetic field [1-4]. Strong locally confined fields can lead to enhanced light

absorption and Raman scattering. The response of plasmonic metals is predominantly limited to the spectral range from ultraviolet to near-infrared (NIR). Beyond this spectral range, plasmons generate weak field confinement, have narrow spectral resonance due to large negative permittivity [5], and exhibit very limited tunability due to high losses [4-6].

As an alternative, two-dimensional (2D) materials such as graphene have demonstrated low attenuation of surface plasmon resonance, which is attributed to a unique band structure and high carrier mobility [7,8]. Graphene plasmons typically occur for the spectral range spanning mid-IR to low terahertz [8, 9]. This has been achieved experimentally through a wide range of tuning mechanisms – higher doping levels, reduced structure dimensions, and gate modulation [9-12]. Fabricating graphene requires a substrate and a dielectric environment, which causes the plasmon-phonon modes to split into two hybrid modes. The dielectric environment surrounding graphene plasmonic structures can also cause weak dispersion and short lifetimes. The coupling between phonons and the plasmon damping effect hinder the utilization of graphene for enhanced light absorption in the low terahertz to mid-IR range [12-14].

Very recently, black phosphorus (BP), a layered semiconductor with a two-dimensional "puckered" hexagonal structure in each monolayer (known as phosphorene), has gained attention in the scientific community as a potential candidate to study surface plasmon polaritons [15-20]. Theoretical and simulation results have revealed that properties of black phosphorous surface plasmons include polarization dependence when exposed to an electromagnetic field [21, 22], dependence on the size of the monolayer [23], a quantized magnetic field indicated by discretized anisotropic magneto-excitons [24], and damping point defects and potential for long-range disorder [25]. These features are attributed to its high mobility and highly tunable, layer-dependent, direct bandgap (0.3 eV in bulk to 2 eV in a monolayer) [26-28], as well as its highly

anisotropic in-plane electronic and optical properties [28]. In addition, these desirable properties make BP suitable for other optical material applications such as hyperspectral imaging, thermal imaging, photodetectors in silicon photonics, and terahertz transistors [29-32]. To date, these opto-electronic properties have been limited to fewer applications due to the instability of BP in ambient conditions [33-37].

In this paper, we explore BP as an alternative 2D material to address the challenges faced by metals and graphene for surface plasmon resonance responses to incident light in the mid- to far-infrared spectral range. First, we focus on a theoretical analysis of the dispersion relation and the confinement strength of surface plasmon modes excited by a linearly-polarized plane wave on an infinite phosphorene sheet, taking the surrounding dielectric media into account. Next, we expand the theoretical work to periodic monolayer BP nanoribbons using finite element simulations. We select a design that can be easily realized in experiments and use numerical simulations to describe the tunable resonance and enhanced absorption of the plasmonic modes for capping layers and substrates of different dielectric values. Further, a theoretical periodic grating model is implemented to determine the wavelength of the resonant absorption peak by calculating the phase of the reflected wave at the edge of the nanoribbon. We also extend the numerical simulation to study BP nanoribbons enhancing absorption in different directions based on the optical conductivity change and ribbon width. Finally, we study mechanisms of preserving phosphorene from oxidation effects while maintaining edge plasmon enhanced absorption. Although phonon-related damping pathways for BP plasmons remain unknown, this work highlights several attractive features of tunable mid- to far-infrared BP plasmons.

4.2 Monolayer Black Phosphorene Conductivity Model

Anisotropic, angular frequency (ω) dependent, dynamical, 2D surface local conductivity of BP can be described by the semi-classical Drude model expression [21].

$$\sigma_{jj} = \frac{i\hbar D_j}{\pi(\hbar\omega + i\eta)} \tag{4.1}$$

Here, j denotes the position along the arm-chair direction (x) and zigzag direction (y). $D_j = \pi N e^2/m_j$ is the Drude weight, which is dependent on the electron charge, e, anisotropic effective electron mass, m_j, and electron density, N. $\eta = 1/\tau$ is the scattering rate (τ is the carrier relaxation time, related to finite damping). The anisotropic effective mass for monolayer or bulk BP gives rise to anisotropic conductivity. Along a plane near the Γ-point in the BP band diagram, the effective electron mass along the x- and y-directions are $m_{cx} = \hbar^2/\left(\frac{2\gamma^2}{\Delta} + \eta_c\right)$ and $m_{cy} = \hbar^2/2v_c$ [21, 38]. Values of the conduction band parameters for monolayers include the following: $\eta_c = \hbar^2/0.4m_0$, $v_c = \hbar^2/1.4m_0$, $\Delta = 2$ eV, and $\gamma = 4\,a/\pi$ eVm, where $a = 0.223$ nm and π/a is the width of the Brillouin Zone in the x-direction [21, 38]. These are chosen such that they yield the known conduction band effective masses $m_{cx} \approx 0.15m_0$ and $m_{cy} \approx 0.7m_0$ of monolayer BP. It is worth mentioning that the band parameters are highly sensitive to the number of BP layers; any small change explicitly affects anisotropic effective masses [38]. We choose the electron carrier density to be from $N = 10^{12}$ to 5×10^{13} cm^{-2}, and a scattering rate of $\eta = 10$ meV that accounts for the finite damping [21]. These N values are within the range reported in *ab initio* studies, giving this scattering rate [39, 40]. Monolayer phosphorene is an ultra-thin film with a thickness of $t_{BP} \approx 0.7$ nm [27]. Although the monolayer thickness extracted from bulk black phosphorus is 0.5 nm [39], we choose a slightly larger value consistent with the measured height

of most samples [18] because this is the one most likely to be realized in experiments and the one that will determine observed plasmonic effects. We can introduce a phosphorene layer with volumetric anisotropic permittivity [41] converting the 2D surface conductivity into a 3D conductivity using the relation $\sigma_{2D} = t_{BP}\sigma_{3D}$ [42]. Hence, the 3D complex anisotropic dielectric function for monolayer BP from Eq. (1) is

$$\varepsilon_{jj} = \varepsilon_r + \frac{i\sigma_{jj}}{\omega\varepsilon_0 t_{BP}} \tag{42}$$

where $\varepsilon_r = 5.65$ is the relative permittivity for monolayer BP [43]. This approach has been previously used in the investigation of surface plasmons in BP [23] and graphene 2D films and nanoribbons [44].

4.3 Plasmon dispersion model equation

The theoretical dispersion calculation of the plasmonic wave for the transverse magnetic (TM) and transverse electric (TE) modes in a continuous BP monolayer was performed following the method outlined by Ju et al. and Grigorenko et al. [45, 46]. A BP layer is situated in the x-y plane, sandwiched between semi-infinite dielectric materials of relative permittivity ε_1 (above) and ε_2 (below). Accordingly, calculations for TM mode and TE mode, propagating perpendicular to the interface between the dielectric medium, are

$$\varepsilon_1/k_{z1} + \varepsilon_2/k_{z2} = -i\sigma_{jj}/\varepsilon_0\omega \tag{4.3a}$$

$$k_{z1} + k_{z2} = i\sigma_{jj}\mu_0\omega \tag{4.3b}$$

where ε_0 is the vacuum permittivity, μ_0 is the vacuum permeability, $k_{z1} = \sqrt{k_{jj,1}^2 - \varepsilon_1 k_0^2}$ and

$k_{z2} = \sqrt{k_{jj,2}^2 - \varepsilon_2 k_0^2}$ are wave vectors above and below the BP layer and k_0 is the vacuum wave

vector. A rough measure of the plasmon mode confinement comes from the real part of Eq. (4.3a) and (4.3b). This can be attained when $k_{jj,1}^2 \gg \varepsilon_1 k_0^2$ and $k_{jj,2}^2 \gg \varepsilon_2 k_0^2$, leading to $k_{z1} = i(\varepsilon_1 + \varepsilon_2)\varepsilon_0\omega/\sigma_{jj}$ for the TM mode and $k_{z1} = i\sigma_{jj}\mu_0\omega/2$ for the TE mode. Accordingly, the surface plasmon confinement factor, n_{eff}, for the infinite BP sheet is related to the free-space wave vector by $n_{eff} = k_{z1}/k_0$. The real part of n_{eff} is directly related to the degree of confinement, and the imaginary component corresponds to the propagation length. Fig. 4.1(a) plots analytical results of TM mode light dispersion for four selected dielectric substrates with n_1 taken to be air. The confinement strength indicates a directly proportional effect of the dielectric constant of the materials surrounding the infinite BP layer. The plasmon confinement strength is on the order of a hundred over the IR range, being comparable to that of graphene [47], while the value for noble metals is close to one. It can be noted that TE mode confinement is barely possible, as the imaginary part of the conductivity, σ_{jj}, in Eq. (4.3b) is positive over the infrared range of the spectrum, corresponding to high loss. It is worth noting that the surface plasmon dispersion can be controlled by the optical conductivity of phosphorene via N. Doing so enables switching between surface plasmon modes that are strongly IR-supported and those that are not.

An alternate way to realize strong coupling and extreme field confinement with localized plasmons is by decreasing a BP sheet to finite nanoscale in-plane dimensions [23]. Finite size BP can add exotic edge states and lateral confinement in the main band gap [48]. For ideal edges and sub 10 nm scale structures, these would need to be addressed to take into account the quantum effects on the plasmonic resonance. However, atomic resolution scanning tunneling spectroscopy of exfoliated black phosphorus reveals only a trivial modification of the band gap at the sample edges [49]. In addition, monolayer black phosphorus nanoribbon widths below a few nanometers are required to significantly modify the band gap [48, 49]. In this study we focus on properties of

plasmonic responses for periodic nanoribbons with a minimum width of 100 nm and minimum gap of 25 nm. Due to this geometry, the spectral range of the plasmonic resonances studied here is substantially greater than the Fermi wavelength of BP nanoribbons [48]. Because of the aforementioned conditions, the quantum effects can be neglected. From here forward, we focus on properties of plasmonic responses for such reduced periodic arrays of BP ribbons. We have investigated these using a classical model with optical constants of infinite 2D monolayers of black phosphorus, Eq. (4.1) and Eq. (4.2).

A 3D schematic view of the structure designed for the study of localized surface plasmon polaritons (LSPPs) supported by BP is depicted in Fig. 4.1(b), with a corresponding 2D cross-sectional view shown in Fig. 4.1(c). The arrays of monolayer BP nanoribbons are periodically arranged in the *x-y* plane (z = 0). To confine the enhanced light, an optically thick gold reflector surface was added to the bottom of the model. In the z-direction, nanoribbons are separated from this reflector surface by a dielectric spacer with refractive index $n_2 = \sqrt{\varepsilon_2}$, (z < 0). A top dielectric medium with refractive index $n_1 = \sqrt{\varepsilon_1}$, (z > 0), covers the BP nanoribbon arrays. Data from Palick et al. for wavelength-dependent optical constants of gold were applied to the simulation [50].

4.4 Simulation method:

Two-dimensional FEM simulations [51] were performed to calculate electromagnetic field distributions and absorption spectra on nanoribbon cross-sections that assume infinite length in the *y*-direction. The 2D simulations can accurately approximate calculations of 3D structures so long as the length of the ribbon is large enough compared to the propagation and coupling length of the surface plasmon wavelengths. Periodic boundary conditions were applied along the left and right edges of the model (along the *x*-direction). Perfectly matched layers (PMLs) were added above

and below this structure to eliminate the back scattering of electromagnetic waves from the model boundaries. A plane wave polarized in the x-direction illuminates the ribbons from above, normal to the substrate surface, in the TM case for the periodic structure. The top boundary was set as the input port and the bottom as the output. A non-uniform mesh was adopted, and the minimum mesh size inside the BP layer equals 0.01 nm, gradually increasing to 50 nm outside the dielectric region.

The electric field intensity distributions obtained from a finite element electromagnetic simulation [51] are shown in Fig. 4.1(d – f) for the simulated illumination via plane wave at downward normal incidence for three different wavelengths. The width (w) of the BP ribbon was set to 150 nm, the period (P) to 250 nm, and the gap (g) between each ribbon was $g = P - w = 100$ nm. The ribbon width and period were selected so that the tunable range for wavelength went through the far-IR region of the electromagnetic spectrum. The ribbon was modeled to be surrounded by air ($n_1 = 1.0$) on the top surface and a dielectric substrate ($n_2 = 1.71$) of thickness 5 μm beneath. The dielectric substrate was made greater than $\lambda/2$ to avoid any coupling effects of the local fields near the BP ribbon and the gold surface. The field distribution reveals that the surface plasmon is highly confined at the edges of the nanoribbon and the confinement strength of the localized field is highly dependent on the excitation wavelength.
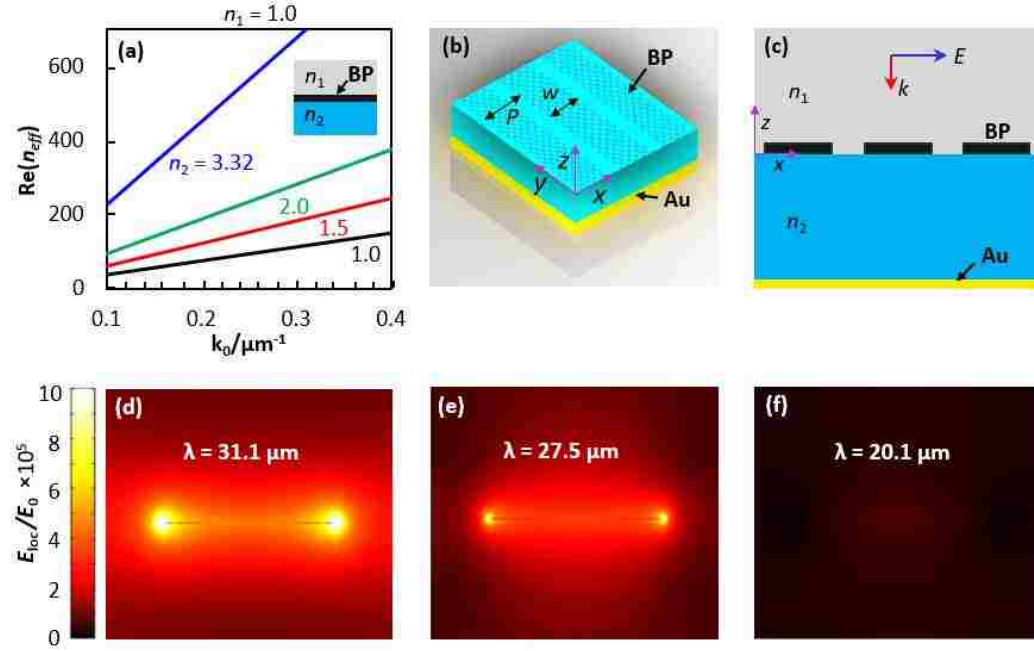
Figure 4. 1. Simulation of the electromagnetic response of illuminated BP. **(a)** Plot of the real part of the SPP modes supported by a BP infinite sheet for four different dielectric media as measured by its vacuum wave vector. **(b)** 3D schematic of periodically patterned phosphorene nanoribbons on a dielectric layer (light blue) atop a gold reflective surface. Period, P, and ribbon length, w, are labeled. **(c)** Cross-sectional view of **(b)** with the BP, Au, two dielectric layers, n_1 and n_2, and light propagation and polarization directions, E and k, labeled. **(d)** – **(f)** Calculated distributions of the electric field enhancement, which is defined as the ratio of the local electric field amplitude, E_{loc}, to that of the incident light, E_0. The modeled parameters include $w = 150$ nm, $P = 250$ nm, $n_1 = 1.0$, and $n_2 = 1.71$, $N = 10^{13}$ cm^{-2}, at $\lambda =$ **(d)** 31.1, **(e)** 27.5, and **(f)** 20.1 µm.

Strong field enhancement and localization of plasmon modes in the two-dimensional structure leads to enhanced spectral absorption depending on the shape and the selection of appropriate surrounding dielectric material [52]. Fig. 4.2(a) displays simulated normal-incidence absorption spectra of the BP nanoribbons for $w = 150$ nm and $P = 250$ nm. Here, the top medium was set to the refractive index, n_1, of air, and the absorptive substrate was swept from $n_2 = 1.0$ to 3.32. Some of the selected indices of refraction, n_2, values chosen match materials such as Al$_2$O$_3$ (1.71) [53], KBr (1.43) [54], PMMA (polymethyl methacrylate, 1.45 [55]), PS (polystyrene, 1.50) [55], and Si

(3.32) [50]. Fig. 4.2(b) is a plot of the resonant wavelengths (those with absorption peaks) versus the n_2 values at which they occur, and Fig. 4.2(c) shows the absorption values at these peaks.
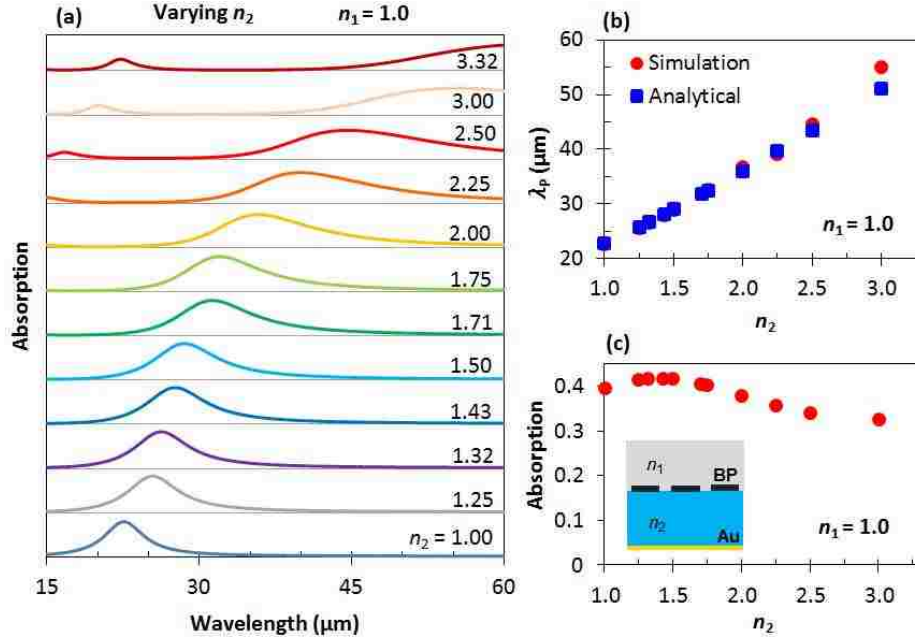

Figure 4.2. Calculated results showing the effects of varying n_2 on the absorption spectrum with n_1 held constant. **(a)** Simulated normal-incidence TM mode electric field absorption spectra for BP nanoribbons surrounded by air ($n_1 = 1.0$) and different substrate materials with refractive indices, n_2, and a BP electron density of $N = 10^{13}$ cm^{-2}. **(b)** Absorption peak resonant wavelength of the fundamental mode ($m = 1$) with respect to the refractive index of the substrate dielectric layer (n_2). The red dots are from the finite-element method (FEM) simulations, and the blue dotes are calculated from the theoretical model described in Eq. (4). **(c)** Peak absorption amplitude as a function of n_2.

As n_2 is increased, the absorption peak position shifts to higher infrared wavelengths, Fig. 4.2(b), and broadens; and the amplitude generally decreases, as plotted in Fig. 4.2(c), indicating increased damping. Following grating theory, the peak absorption wavelengths, matching the resonant conditions of periodic BP nanoribbon, can be obtained from Eq. (4.4) under irradiation of light at normal incidence,

$$\lambda_p = \pi c \sqrt{\frac{2P\varepsilon_0(\varepsilon_1 + \varepsilon_2)m_j}{m\pi N e^2}}. \tag{4.4}$$

Here, λ_p is the resonance wavelength of the BP plasmons, c is the speed of light, P is the period, ε_0 is free space permittivity, e is the charge of a single electron, and m is a positive integer ($m = 1$, 2, 3, …) representing the order of the dispersion of the mode confinement diffraction. The resonance wavelengths of the analytical solution, Eq. (4.4), obtained via the periodic grating approach, do not consider the near-field interaction between the BP ribbons when the period is much smaller than the surface plasmon resonance wavelength, and disregards nonlocal effects. Due to coupling of plasmon waves between nearby BP nanoribbons and multiple anomalous reflections between the two edges of the ribbon, the reflected plasmon waves can form an interference process that incorporates a phase factor other than π. The surface plasmon at the resonance point undergoes constructive interference with the reflected wave between the edge, satisfying $2wRe(k_{z1}) + 2\phi = 2m\pi$ [56, 57]. Here, w is the ribbon width, ϕ is the reflection phase at the edge, and m is an integer for the peak resonance order. The value of ϕ can be obtained analytically by fitting the simulated data of a given ribbon surrounded by *an arbitrary* dielectric medium using Eq. (4.5),

$$\phi/\pi = m - \frac{\varepsilon_0(\varepsilon_1+\varepsilon_2)w}{D_{xx}}\left(\frac{2\pi c}{\lambda_p}\right)^2.$$ (4.5)

Fig. 4.2(b) and (c) illustrate the absorption resonance wavelength for different values of n_2 obtained both via simulation and theoretical calculation via Eq (4.5). It is found that primary mode red shift linearly as the dielectric constant increases of the resonance wavelength consistent result in both theory and simulation. To further elucidate the effect of the surrounding dielectric, Fig. 4.3(a) and (b) show calculated and simulated absorption spectra for a range of n_1 from 1 to 1.71 for fixed $n_2 = 1.71$. The first-order phase factor was calculated using Eq. (4.5) for ranges between 0.41π and 0.46π, depending on the dielectric environment. Although similar situations are

observed, the spectral broadening and resonance wavelength shifts are much weaker compared to the case of changing n_2. The absorption peak wavelengths are only for dipolar modes and stay between 27% to 41% with the change of the top dielectric environment, Fig. 4.3(c).

The resonance properties in the absorption spectra intensity and line width are also influenced by the optical loss in the BP ribbons, which is mainly characterized by the real part of the conductivity.
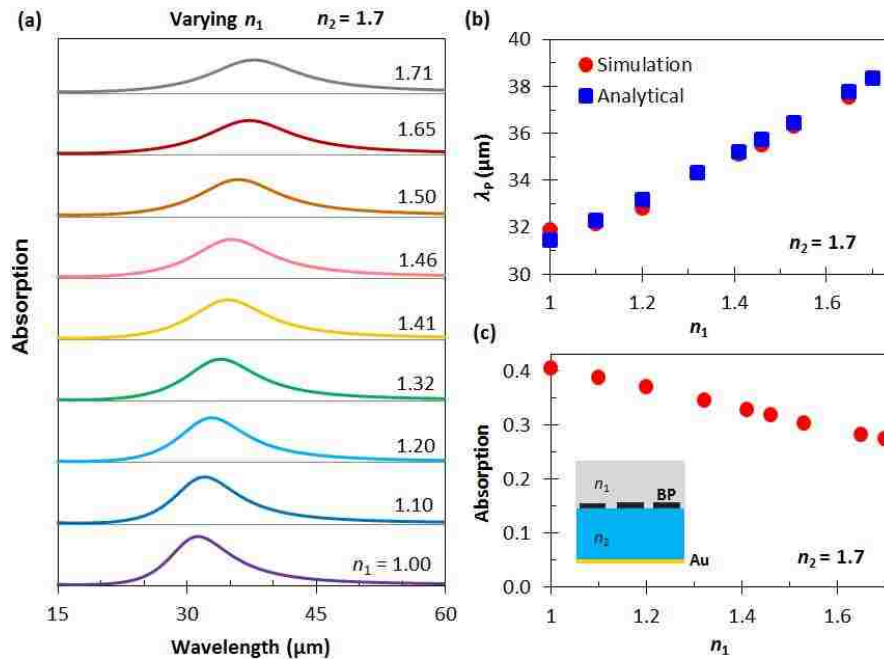

Figure 4.3. Calculated results showing the effects of varying n_1 on the absorption spectrum with n_2 held constant. **(a)** Simulated normal-incidence TM mode electric field absorption spectra for BP nanoribbons surrounded by different materials with refractive indices, n_1, on a substrate with $n_2 = 1.7$ (Al$_2$O$_3$) and a BP electron density of $N = 10^{13}$ cm^{-2}. (b) Absorption peak resonant wavelength of the fundamental mode ($m = 1$) with respect to the refractive index of the surrounding dielectric layer (n_1). The red dots are from the FEM simulations, and the blue dotes are calculated from the theoretical model described in Eq. (4). **(c)** Peak absorption amplitude as a function of n_1.

4.5 Phosphorene supported absorption enhancement

The theoretical model predictions of enhanced infrared absorption and plasmonic resonance depend on the effective mass and density of carriers in the BP ribbons. The wavelength of the

plasmon resonance in phosphorene nanoribbons scales proportionally with $N^{-1/2}$, the same as in conventional semiconductors but contrary to graphene nanoribbons, which show a proportionality of $N^{-1/4}$ [45]. According to Eq. (4.5), decreasing the anisotropic effective mass, which is dependent on the BP layer thickness, results in a blueshift and strong plasmon localization, while increasing the electron carrier density causes a redshift. The electron (carrier) density, related to the carrier mobility, is controlled by the chosen type of dielectric interface, [58, 59] the introduction of doping, or gated-modulation [21]. To understand the tunability of the plasmon resonance and therefore the absorption wavelength in BP ribbons, it is instructive to inspect the significance of altering the conductivity and the ribbon geometry.

The armchair and zigzag directions of phosphorene are shown in Fig. 4.4(a) and (b), respectively. We would like to achieve higher absorption enhancement for light polarized in each direction. Here, optical constants of $n_1 = 1.0$ and $n_2 = 1.71$ and a reflective gold layer, as in Fig. 4.1(b), were considered. According to Eq. (4.5), one can tune the absorption spectra by changing the number density and the width of BP ribbons. To better quantitatively understand this tunability, absorption simulation results were obtained for the situation where the number density $N = 5 \times 10^{12}$, 7.5×10^{12}, and 2.5×10^{13} cm^{-2}, and the period was constant at $P = 250$ nm over a range of w from 100 nm to 225 nm. Fig. 4.4(c) and (d) show plots of absorption spectra for light polarized in the armchair and zigzag directions, respectively, for the simulated range of w values for $N = 2.5 \times 10^{13}$ cm^{-2}. The results for $N = 5 \times 10^{12}$ and 7.5×10^{12} cm^{-2} are provided in supplementary Fig. S (C. 5.)

The peak absorption wavelength position is highly sensitive to w due to the resonance condition of the localized surface plasmons, and it is also affected by the ribbon spacing, $g(w) = P - w$, due to strongly coupled resonances between neighboring ribbons. With a constant period of 250 nm, the gap between ribbons becomes small for large w, increasing the strength of the coupling effect.

Shown in Fig.4. 4(c), the absorption is minimal for light polarized in the armchair direction when w is small (and the gap is large) – due to weak plasmon localization and less field confinement at the edges. As w increases, so does the absorption, up to 0.83 for $w = 225$ nm, corresponding also to the smallest spacing value ($g = 25$ nm), since the coupling between neighboring ribbons increases. For the larger widths, the absorption peak also redshifts as w increases due to both width-dependent plasmon resonances and gap-dependent coupling between ribbons. In the zigzag direction, Fig. 4.4(d), the resonant wavelength redshifts from ~25 μm to 47 μm over the range $w = 100 – 225$ nm. In both the armchair and zigzag orientations, the peak shift shows that the ribbon width and spacing play important roles in tuning the BP ribbon plasmon resonance. The difference in the peak position and amplitude for the same values of w between zigzag and armchair directions is due to each atomic orientation having different anisotropic masses, which leads to different imaginary parts of the dielectric function; see Eq. (4.1) and (4.2).
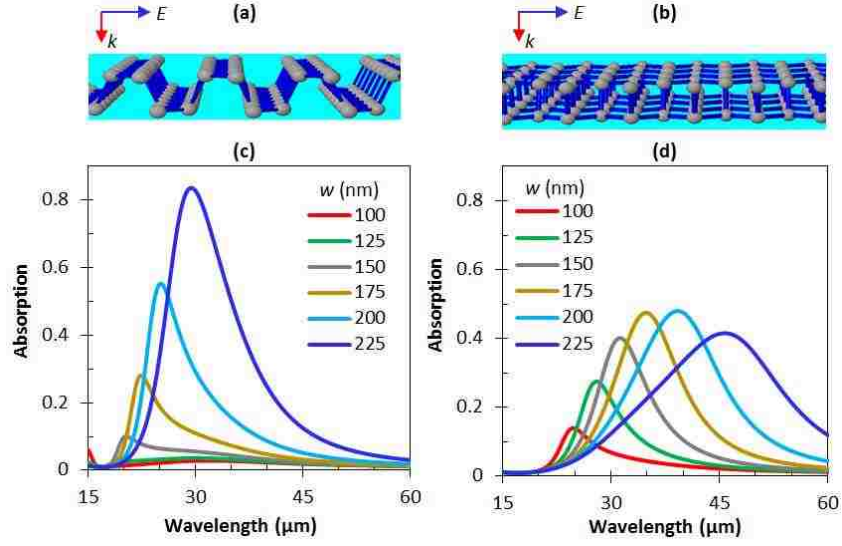
Figure. 4.4. Comparison of the optical response of light polarized in the **(a)** armchair and **(b)** zigzag directions. Simulated absorption spectra for normal-incidence TM mode light polarized along the **(c)** armchair and **(d)** zigzag directions for different w. Here, $n_2 = 1.71$, $n_1 = 1.0$, $N = 2.5\text{x}10^{13}$ cm^{-2}, $P = 250$ nm, and w is swept from 100 to 225 nm.

The absorption strength in the zigzag direction increases from 0.14 to 0.48 for number density N = 2.5×10^{13} cm^{-2}, compared to the absorption peak value of 0.13 reported by Liu and Aydin for $N = 10^{13}$ cm^{-2} [23]. When one compares the peak wavelengths between $N = 10^{13}$ cm^{-2} (Fig. 2) and $N = 2.5\times10^{13}$ cm^{-2} (Fig. 4.4) for $w = 150$, both armchair and zigzag directions show a blueshift of the absorption peak with increased carrier concentration, consistent with the prediction of Eq. (4.5). For carrier number density below $N = 10^{13}$ cm^{-2} (see supplementary information), a width-dependent-dominant absorption is observed in the armchair direction and a weak resonance in the zigzag direction. Therefore, changing the electron number density, N, by using different substrates, doping the BP, or gating introduces a mechanism for tuning and amplifying the plasmonic resonance in BP.

4.6 Dielectric encapsulated periodic black phosphorene ribbon

Black phosphorus is highly reactive with oxygen; upon exposure to the environment, it degrades in a matter of minutes or hours [21, 31-37]. Also, exposure to moisture causes significant distortion of its structure, causing the formation of porous regions that eventually decompose [31-37]. Encapsulation of BP with a thin dielectric sheet is essential for stability [58, 59]. Therefore, we investigate how the dielectric sheet affects the edge plasmon modes in BP. Numerical simulations have been performed to demonstrate the electromagnetic response of phosphorene nanoribbons capped with two materials: a lossless dielectric, Al_2O_3, and a hyperbolic metamaterial hexagonal boron nitride (hBN) with optical constants obtained from [60].

First, encapsulation via Al_2O_3 was studied, with the results shown in Fig. 4.5. Fig. 4.5(a) shows the geometry of the model. For consistency with earlier discussions, we kept $P = 250$ nm, $w = 150$ nm, $n_1 = 1.0$, and $n_2 = 1.71$, the refractive index of Al_2O_3. Fig. 4.5(b) shows the absorption spectra, corresponding to infrared plasmons, with the BP ribbon positioned at different distances (d) inside the substrate in the armchair direction. The peak wavelength shifts by approximately 1.5 μm as d increases from 0 to 10 nm inside the substrate, shown in detail in Fig. 4.5(c). The range of d is important to maintain the absorption amplitude so that it does not lead to a large change in the optical path length within the dielectric, potentially creating a standing wave. The small shift in wavelength and consistent peak absorption amplitude from Fig. 5 verify that dielectric layer encapsulation helps to conserve the main plasmon resonance properties. These small fine-tuned plasmon wavelength shifts due to a thin capping layer have interesting implications for light-matter interactions with regard to BP plasmon infrared nanoresonators, potentially for highly sensitive sensors.
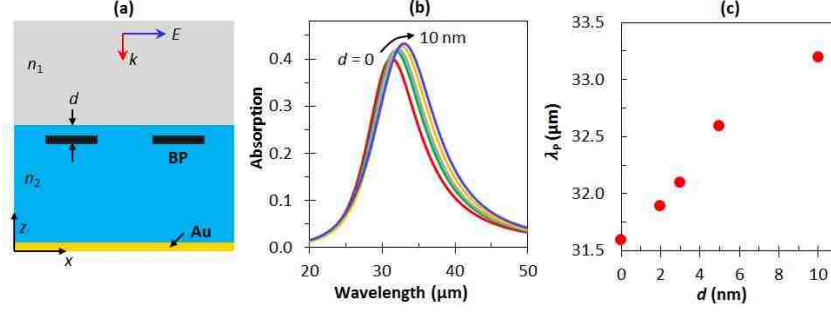
Figure 4.5. Results for simulated patterned BP nanoribbons encapsulated by a dielectric buffered layer at different depths, d. **(a)** 2D cross-sectional schematic **(b)** Simulated absorption spectra for $d = 0 - 10$ nm and **(c)** resonance peak position as a function of d. Here, $P = 250$ nm, $w = 150$ nm, $n_1 = 1.0$, $N = 10^{13}$ cm^{-2}, and $n_2 = 1.71$ (Al$_2$O$_3$).

Next, we simulated hBN, anisotropic hyperbolic material, as an overlayered sheet for preserving the surface of the BP ribbons from degradation. hBN provides a superior protection layer for BP, mainly because it provides high mechanical strength, high thermal stability and chemical inertness [59, 61]. In addition, the layer numbers (thickness) of hBN can be precisely controlled from monolayer to multilayer during the fabrication process through mechanical exfoliation or chemical vapor deposition methods [62]. Fig. 4.6(a) and (b) depict the simulation design for BP ribbons encapsulated with hBN layers of different thickness, d. The armchair and zigzag directions are depicted again in Fig. 4.6(c) and (d), respectively. The simulated total absorption spectrum with d swept from 0 to 10 nm for TM polarized light in the zigzag and armchair directions are shown in Fig. 4.6(e) and (f), respectively.

The case of extremely small gaps between ribbons ($w = 225$ nm) was studied for $N = 2.5 \times 10^{13}$ cm^{-2}. As shown in Fig. 4.6(e) and (f), the resonant wavelength shifts from 29 μm to 39 μm for armchair polarization, and 47 μm to 56 μm for zigzag. The gradual peak redshift is significantly larger than that of BP embedded in Al$_2$O$_3$. The absorption intensity is maintained between 80% and 90% in the armchair direction. The zigzag peak absorption drops gradually from 42% to 29% as the thickness of hBN increases, less than half of the values for armchair peak absorption. The

presence of the hBN results in a strong localization of the field at the hBN/BP/dielectric interface in armchair direction and weak localization for zigzag. This is mainly due to the full electrical contact and strong interactions in the hybrid interaction that can arise between the ribbon plasmons and a thickness dependent phonon polariton mode that can arise in the hBN [63]. In addition, a noticeable broadening of the absorption peaks occurs for both polarization directions with the introduction of hBN on the BP ribbons.
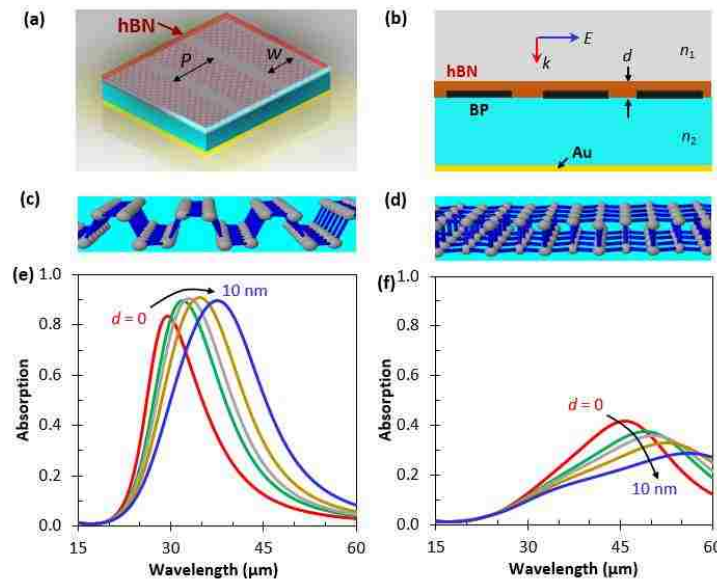

Figure. 4.6 **(a)** 3D and **(b)** 2D schematics of the simulated BP ribbons covered by a protective layer of hBN film of thickness d. **(c)** Armchair and **(d)** zigzag polarization directions as shown in Fig. 5. Simulated normal-incidence TM mode electric field absorption spectra for different thicknesses of hBN encapsulating BP for **(e)** armchair and **(f)** zigzag directions. Here, $w = 225$ nm, $P = 250$ nm, $n_1 = 1.0$, $n_2 = 1.71$, and $N = 2.5 \times 10^{13}$ cm^{-2}.

4.7 Conclusion

In summary, we have investigated propagating surface plasmon properties of black phosphorus sheet- and edge-confined plasmons in surrounding dielectric structures for enhanced tunable absorption. Theoretical schemes of the plasmonic dispersion showed

dependence on BP anisotropy, light polarization direction, and dielectric material. In particular, the confinement factor of SPPs has a strong effect, a factor of hundreds, on isolated BP and that increases as the refractive index of the surrounding media increases. Scaling of BP into the nanoribbon size leads to the formation of edge plasmons that trigger enhanced absorption. Simulation results of the spectral position and the absorption peaks can be adjusted both by the anisotropic nature of BP as well as by parameters such as the refractive index, ribbon size, ribbon spacing, and electron density; and the results have validated the theoretical prediction. Additionally, simulations of plasmon enhanced absorption behavior encapsulated the BP ribbon with either a protection nanolayer of lossless dielectric material or the metamaterial hBN to address the possibility of degradation through oxidation. The result shows further mechanisms of tuning resonance modes in infrared wavelengths due to hybridization of BP ribbon edge plasmon and the hyperbolic modes of hBN. The research achievements reveal a promising future for black phosphorene as a plasmonic material with properties that can give a viable platform to plasmon modulated optoelectronic devices across the infrared region of the spectrum.

References

[1] Barnes, W. L., Dereux, A. & Ebbesen, T. W. Surface plasmon subwavelength optics. *Nature* **424**, 824–830 (2003).

[2] Maier, S. A. & Atwater, H. A. Plasmonics: localization and guiding of electromagnetic energy in metal/dielectric structures. *J. Appl. Phys.* **98**, 011101 (2005).

[3] Ozbay, E. Plasmonics: merging photonics and electronics at nanoscale dimensions. *Science* **311**, 189–193 (2006).

[4] Atwater, H. A. The Promise of Plasmonics. *Scientific American* **296**, 56–63 (2007).

[5] Law, S., Yu, L., Rosenberg, A. & Wasserman, D. All-semiconductor plasmonic nanoantennas for infrared sensing. *Nano Lett.* **13**, 4569–4574 (2013).

[6] Pendry, J. B., Schurig, D. & Smith, D. R. Controlling electromagnetic fields, Science, **312**, 1780 (2006).

[7] Low T. & Avouris P. Graphene Plasmonics for Terahertz to Mid-Infrared Applications. *ACS Nano* **8**, 1086–1101 (2014).

[8] Niu, J., Jun Shin, Y. Lee, Y., Ahn, J. H. & Yang. H. Graphene induced tunability of the surface plasmon resonance. *Appl. Phys. Lett.*, 100, 061116 (2012).

[9] Fei, Z. *et al.* Gate-tuning of graphene plasmons revealed by infrared nano-imaging. *Nature* **487**, 82–85 (2012).

[10] Yan, H. *et al*. Infrared spectroscopy of tunable Dirac terahertz magneto-plasmons in graphene. *Nano Lett.* **12**, 3766–3771 (2012).

[11] Fang, Z. *et al*. Active tunable absorption enhancement with graphene nanodisk arrays. *Nano Lett.* **14**, 299–304 (2014).

[12] Yan, H. et al. Damping pathways of mid-infrared plasmons in graphene nanostructures. *Nat. Photonics* **7**, 394–399 (2013).

[13] Niu, J. *et al.* Shifting of surface plasmon resonance due to electromagnetic coupling between graphene and Au nanoparticles. *Opt. Express*, **20**, 19690–19696 (2012).

[14] Niu J., Shin Y. J, Lee Y, Ahn J. H, Yang H Graphene induced tunability of the surface plasmon resonance. *Appl Phys Lett* **100**(6) 1116-1120 (2012).

[15] Li, L. *et al*. Black phosphorus field-effect transistors. *Nat. Nanotechnology*, 9, 372– 377 (2014).

[16] Xia, F., Wang, H. & Jia, Y. Rediscovering black phosphorus as an anisotropic layered material for optoelectronics and electronics. *Nature Commun.* **5**, 4458 (2014).

[17] Liu, H. *et al*. Phosphorene: an unexplored 2D semiconductor with a high hole mobility. *ACS Nano*, **8,** 4033–41 (2014).

[18] Wang, X. *et al*. Highly anisotropic and robust excitons in monolayer black phosphorus. *Nat. Nanotechnology*, 1**0,** 517–521 (2015).

[19] Koenig, S., Doganov, R., Schmidt, H., Castro Neto, A. & Ozyilmaz, B. Electric field effect in ultrathin black phosphorus. *Appl. Phys. Lett.* **104**, 103106 (2014).

[20] Qiao, J., Kong, X., Hu, Z., Yang, F. & Ji, W. High-mobility transport anisotropy and linear dichroism in few-layer black phosphorus. *Nat. Commun*. **5**, 4475 (2014).

[21] Low, T. *et al.* Plasmons and Screening in Monolayer and Multilayer Black Phosphorus. *Phys. Rev. Lett.* 113, 106802 (2014).

[22] Rodin, A. S. & Castro Neto, A. H. Collective modes in anisotropic double-layer systems. *Phys. Rev.* B **9**, 075422 (2015).

[23] Liu, Z. & Aydin, K. Localized surface plasmons in nanostructured monolayer black phosphorus. *Nano Letters* **16**(6), 3457-3462 (2016).

[24] Jiang, Y., Roldán, R., Guinea, F. & . Low, T. Magneto-electronic properties of multilayer black phosphorus. *Phys. Rev.* B **92**, 085408 (2015).

[25] Jin, F., Roldán R., Katsnelson, M. I. & Yuan, S. Plasmonics in strained monolayer black phosphorus. *Phys. Rev.* B **92**, 115440 (2015).

[26] Rodin, A. S., Carvalho, A. & Castro Neto, A. H. Strain-induced gap modification in black phosphorus. *Phys. Rev. Lett.* **112**, 176801 (2014).

[27] Yang, J. *et al.* Optical tuning of exciton and trion emissions in monolayer phosphorene. *Light: Sci. Appl.* **4**, e312 (2015).

[28] Li, P. & Appelbaum, I. Electrons and holes in phosphorene. *Phys. Rev. B* **90**, 115439 (2014).

[29] Engel M., Steiner M. & Avouris P. Black Phosphorus Photodetector for Multispectral, High-Resolution Imaging. *Nano Lett*. **14**, 6414–6417 (2014).

[30] Viti, L. *et al.* Black phosphorus terahertz photodetectors. Adv. Mater. 27, 5567–5572 (2015).

[31] Castellanos-Gomez, A. *et al.* Isolation and characterization of few-layer black phosphorus. *2D Materials* **1**, 025001 (2014).

[32] Buscema, M., *et al.* Fast and broadband photoresponse of few-layer black phosphorus field-effect transistors. *Nano Lett*. **14** 3347–3352 (2014).

[33] Ziletti, A., Carvalho, A. Campbell, D. K. Coker, D. F. and Castro Neto, A. H. Oxygen defects in phosphorene. *Phys. Rev. Lett*. **114**, 046801 (2015). [34] Favron, A. *et al.* Exfoliating pristine black phosphorus down to the monolayer: photo-oxidation and electronic confinement effects. *arXiv preprint arXiv:1408.0345* (2014).

[35] Sland, J. O., Steele, G. A., van der Zant, H. S. & Castellanos-Gomez, A. Environmental instability of few-layer black phosphorus. *2D Mater*. **2**, 011002 (2015).

[36] Kim, J. S. *et al.* Toward air-stable multilayer phosphorene thin-films and transistors. *Sci. Rep.* **5**, 8989 (2015).

[37] Pei, J. *et al.* Producing air-stable monolayers of phosphorene and their defect engineering, Nat. Commun. **7** 10450 (2016).

[38] Low, T. *et al.* Tunable optical properties of multilayer black phosphorus thin films. *Phys. Rev. B* **90**, 075434 (2014).

[39] Tea, E., & Hin C. Charge carrier transport and lifetimes in n-type and p-type phosphorene as 2D device active materials: an ab initio study, Physical Chemistry Chemical Physics, (18) 22706-22711 (2016).

[40] Han, W. H., Kim S., Lee I. H., & Chang K. J., Prediction of Green Phosphorus with Tunable Direct Band Gap and High Mobility, J. Phys. Chem. Lett., 8(18) 4627-4632 (2017).

[41] Maier, S. A. *Plasmonics: fundamentals and applications* 29–30 (Springer Science & Business Media, 2007).

[42] Matthes, L. *et al.* Optical properties of two-dimensional honeycomb crystals graphene, silicene, germanene, and tinene from first principles, *New J. Phys.* 16 105007 (2014).

[43] Asahina, H. and Morita, A. Band structure and optical properties of black phosphorus. Journal of Physics C: Solid State Physics, **17**, 1839 (1984).

[44] Gao, W., Shu, J., Qiu, C. & Xu, Q. Excitation of plasmonic waves in graphene by guided-mode resonances. ACS Nano 6, 7806–7813 (2012).

[45] Ju, L. *et al.* Graphene plasmonics for tunable terahertz metamaterials. *Nat. Nanotech*. **6**, 630–634 (2011).

[46] Grigorenko, A. N., Polini, M. & Novoselov, K. S. Graphene plasmonics. *Nature Photon.* 6, 749–758 (2012).

[47] Du, L. *et al.* Edge-Reflection Phase Directed Plasmonic Resonances on Graphene Nano-Structures. *Opt Express* **22** (19), 22689-22698 (2014).

[48] Tran, V. & Yang, L. Scaling laws for the band gap and optical response of phosphorene nanoribbons. Phys. Rev. B 89, 245407 (2014).

[49] *Liang L. et al*. Electronic bandgap and edge reconstruction in phosphorene materials. Nano Lett. 14, 6400–6406 (2014).

[50] Palik E. D*., Handbook of Optical Constants., Academic Press Inc., San Diego (1985).*

[51] COMSOL Multiphysics®, v. 5.0. www.comsol.com. COMSOL AB, Stockholm, Sweden.

[52] Thongrattanasiri, S., Koppens, F. H., de Abajo, F. J. G. Complete optical absorption in periodically patterned graphene. *Phys. Rev. Lett*. **108,** 047401 (2012).

[53] Engel, M. *et al.* Light-matter interaction in a microcavity-controlled graphene transistor. *Nat. Commun.* **3**, 906 (2012).

[54] Li, H. H. Refractive index of alkali halides and its wavelength and temperature derivatives. *J. Phys. Chem. Ref. Data* **5**, 329-528 (1976)

[55] Maharana, P. K., Jha, R, & Palei S. Sensitivity enhancement by air mediated graphene multilayer based surface plasmon resonance biosensor for near infrared, Sens. Actuators. B: Chem., vol. 190, pp. 494-501, (2014).

[56] Velizhanin, K. A. Geometric universality of plasmon modes in graphene nanoribbon arrays. *Phys. Rev. B: Condens. Matter Mater. Phys.* **91,** 125429, (2015).

[57] Brar, V. W., Jang, M. S., Sherrott, M., Lopez, J. J. & Atwater, H. A. Highly confined tunable mid-infrared plasmonics in graphene nanoresonators. *Nano Lett.* **13**, 2541–2547 (2013).

[58] Viti, L., *et al*. Heterostructured hBN-BP-hBN Nanodetectors at Terahertz Frequencies *Adv. Mater.* **28**, 7390 – 7396 (2016).

[59] Chen, X. *et al.* High-quality sandwiched black phosphorus heterostructure and its quantum oscillations. *Nat. Commun.* **6**, 7315 (2015).

[60] Caldwell, J. D. *et al.* Sub-diffractional volume-confined polaritons in the natural hyperbolic material hexagonal boron nitride. *Nat. Commun.* **5**, 5221 (2014).

[61] Constantinescu, G. C. & Hine, N. D. Multipurpose Black-Phosphorus/hBN Heterostructures, *Nano Lett.* **16** (4), pp 2586–2594, (2016).

[62] Sinha S, Takabayashi Y, Shinohara H and Kitaura R. Simple fabrication of air-stable black phosphorus heterostructures with large-area hBN sheets grown by chemical vapor deposition method. *2D Mater.* **3** 035010 (2016).

[63] Shi, Z. *et a*l. Amplitude- and Phase-Resolved Nanospectral Imaging of Phonon Polaritons in Hexagonal Boron Nitride, *ACS Photonics* **2**, 790 (2015).

[64] D. T. Debu, S. J. Bauman, D. French, Hugh O. H. Churchill, J. B. Herzog, "Tuning Infrared Plasmon Resonance of Black Phosphorene Nanoribbon with a Dielectric Interface", Scientific Reports 8(1), 3224 (2018).

Chapter 5

Hybrid hyperbolic surface plasmon phonon polariton for spontaneous emission

Abstract

We use theoretical models to study low THz electromagnetic wave propagation in ferroelectric and graphene/ferroelectric hybrid structures. Ferroelectric $LiNbO_3$ can be considered a natural hyperbolic material that supports both type I and type II Reststrahlen hyperbolicity phonon polariton dispersion. Isolated graphene, which supports surface plasmons in both the mid-infrared and terahertz ranges, strongly couples with ferroelectric hyperbolic phonon-polaritons, forming tunable hybrid plasmon–phonon-polaritons (HSPPs). Through variation of the chemical potential of graphene and the thickness of the ferroelectric layer, the supported HSPPs modes were investigated. Results include bands with considerably flat dispersions as well as linear and hybrid dispersions crossing beyond the longitudinal and transverse phonon frequency range of $LiNbO_3$. Comparative analysis of Purcell radiation presented for a point dipole (quantum emitter) positioned at different locations between ferroelectric and graphene-integrated ferroelectric layers reveals that this system can support strong spontaneous emission that can be modulated with the graphene chemical potential. Changing the chemical potential through selective voltage biasing demonstrates a substantial increase or decrease in the decay rate for spontaneous emission. Further analysis of the emission phenomenon shows a dependence on factors such as the relative radiating source position and the thickness of the ferroelectric film. Such characteristics make graphene-ferroelectric materials very promising candidates to modify the light-matter interaction at low THz ranges for thermovoltaic devices and waveguiding modulators.

5.1 Introduction:

The discovery of graphene two dimensional (2D) materials [1,2] has drawn immense scientific attention both experimentally and theoretically for advanced electrical or optoelectronic application [3,4]. Particularly an external electric field strongly interacts exciting electrons collective vibrate, surface propagating plasmons (SPPs) [5,6,7,8]. The surface oscillating electrons are extremely confined with a relatively low level of losses much better-quality properties plasmon than traditional noble metals and that operates mostly optical wavelength, infrared operating plasmonic materials [9,10,11,12,13,14,15]. Mainly at longer wavelength conventional metals such as Au, Ag and Al behaves nearly as perfect electrical and above near infrared wavelength suffers loss [16]. So, for above infrared studies phononic materials which supporting propagating and localized surface phonon polaritons (PSPPs and LSPPs, respectively) widely used [17]. But in longer operation wavelength materials are limited in very narrow spectrum, typically bounded between the longitudinal and transversal phonon modes hence lucks flexibility. Since graphene plasmon can be controlled several mechanisms such as optimization of geometry [18], number of layers [18], dynamically tuning by means of chemical doping or gate voltage from infrared to THz range [18] and mechanical strain [19,20,21], magnetic bias [22,23].

With this insight high quality heterostructures that support propagating phonon modes or hyperbolic phonon-polaritons (HPPs) consists of graphene are regarded to have great potential for plasmonic applications. Both theoretical prediction and experimental extensive investigation of graphene plasmon and surface phonons polariton (SPPs), in widely availability of mid-IR optical materials, most notably silicon carbide (SiC), [24,25,26,27,28,29,30], SiO_2[26,31,], HfO_2 [26], SiN_x [32] offered bigger picture of the hybridization mechanism that lead to formation of localized

Surface-Plasmon-Phonon-polarions (SPPPs). Other candidates, thin III-V group semiconductor epilayers such as (heterostrucure of GaAs /AlAs GaAs) [33] results stronger graphene-induced optical phonon quenching than that of thin metal films. of coupling of graphene proposed giving rise to novel metamaterials which make use of easy gate tunability of the electron density on graphene.

In Piezoelectric materials (ZnO and AlN) plasmons can be switched electrically, resonance can be controled by electrostatic gating with low damping of surface-phonon frequency, in midinfrared frequency range [AIN and ZnO [34]. In addition, material that have type I and type II hyperbolicity of so called, reststrahlen bands, supports propagating HPPs [35] hybridization with graphene SPPs has been also gained attention [36,37,38]. In particular, several experiments conducted to demonstrate the polar van der Waals crystal, hBN, natural two types of hyperbolic responses (two type restrahelen band) [35] exhibits both low losses and long-lived midinfrared hybridized HSPPs [36,37,38]. These studies flourished coupled hybrid modes propagating over relatively long distances, [36,37,38] as well as highly confined three-dimensional [36,37,38,39,40]. Beside such progress at hand studies on interaction of graphene plasmon using hyperbolic material is seldom reported in the low terahertz regime (< 20THz) as most of the natural hyperbolic materials are limited between infrared and near optical frequency range which they show hyperbolic property. In fact, emergence of artificially-engineered THz metamaterial enables the manipulation of the electromagnetic properties. These structures require toying with multiple geometry at nanoscale demanding fabrications precision that physically introduce internal interfaces.

With this insight lithium niobate (LiNbO$_3$) is a polar ferroelectric material that supports subdiffraction confinement of light-waves in two Reststrahlen band within the low terahertz regime (0-15 THz). Experimental advances in recent years and fabrication technique of graphene

on substrate ferroelectric LiNbO$_3$ [41,42,43,44,45] [46] and other ferroelectric materials [47,48,49,50,51] recently, have drawn considerable attention. Graphene/ferroelectric interfaces play a crucial role in the performance of graphene-based electronic devices; electrically programmable nonvolatile memory and field effect-transistors [52,53]. Due to long phonon lifetimes (picoseconds), low loss, high quality factors, high non-linearity and thermal phase transition, graphene/ferroelectric interfaces are highly suitable for several THz applications [54,55,56,57,58,59]. Graphene plasmon hybridization with ferroelectric that supports surface phonon polariton terahertz range leads to the extreme confining quality waveguides compared with conventional dielectric [60]. Absorption spectra of graphene-LiNbO3 hybrid systems shows number of graphene layer dependence, [61], high attenuation and planar tunable waveguides with ultra-low loss in THz region [62]. Visible to mid-wave infrared range propagation of TM surface plasmon polaritons of graphene is controllable by different polarization levels and polarization direction of ferroelectric domain of LiNbO$_3$ [63,64]. Based on these progresses, expanding the studies of the actively tunable HSPPs modes of graphene and nanolayer ferroelectric films using light is substantial interest.

In this work, we demonstrate that combining optical parameters of graphene and the optical phonon resonances response of ferroelectric nanolayer LiNbO$_3$ introduces several bands rich features of HSPPs modes. The dispersion modes of the hybrid structure result frequencies outside the hyperbolic band range in low THz energy of the ferroelectric. One effective way to get insight the light matter interaction process in graphene, hybrid hyperbolic material is quantitative analysis of spontaneous emission (SE) rate or Purcell factor (PF) [65,66,67,68,69,70,71,72]. We explore characteristics of tunable SE in low THz spectra based on gate voltage modulation of graphene, dipole location, and ferroelectric layer size achieved from single quantum (dipole) emitter.
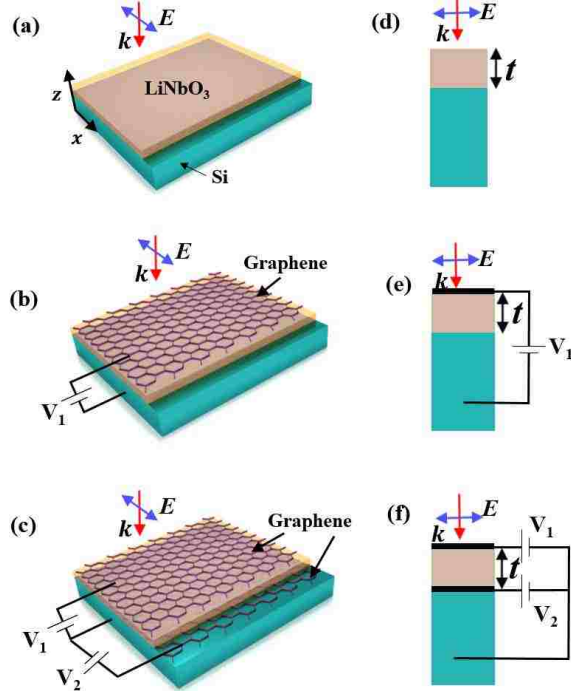
74

Figure 5.1. 3D and corresponding 2D schematics of three different structural configurations as studied in this work. (a) and (d) air/LiNbO₃/substrate, air/graphene/LiNbO₃/substrate (b) and (e), and air/graphene/LiNbO₃/graphene/substrate (c) and (f). The coordinate axes are shown in (a), with incident radiation shown polarized in the x-direction and propagating in the z-direction. The circuit configurations shown in (b) and (c) represent AC voltage sources.

5.2 Optical conductivity of graphene:

The local limit 2D complex conductivity of graphene sheet, within the random phase approximation is given as [74]

$$\sigma(\omega, \tau, \mu, T) = i\frac{e^2 k_B T}{\pi\hbar^2(\omega + i\tau^{-1})}\left[\frac{\mu_c}{k_B T} + 2\ln\left(e^{-\mu_c/k_B T} + 1\right)\right] + i\frac{e^2}{4\pi\hbar}\ln\left(\frac{2|\mu_c| - \hbar(\omega + i\tau^{-1})}{2|\mu_c| + \hbar(\omega + i\tau^{-1})}\right), \qquad (5.1)$$

Here, the first and second terms are the intraband and interband contributions, respectively, ω is the angular frequency, k_B is Boltzmann constant, T is the temperature, e is the electron charge, τ is a finite relaxation time, and μ_c is the chemical potential. The chemical potential can be modulated by external voltage biasing [75], and the relation between the gate voltage (V_g) and the

chemical potential is $\mu_c = \hbar v_F \sqrt{\pi |\alpha_0 (V_g - V_0)|}$, where V_0 is the voltage from natural doping at the Fermi level and $\alpha_0 \approx 9 \times 10^{16}\,\text{m}^{-2}\text{V}^{-1}$, estimated from a parallel-plate capacitor model [75]. We assume constant temperature, $T = 300$ K, and constant $\tau = 10^{-13}$ s which are also within the range of experimentally attained values [9].

5.3 Low terahertz anisotropic hyperbolic optical media

We choose LiNbO$_3$ as the ferroelectric layer because it has uniaxial anisotropic properties in low THz range. The dielectric tensor is uniaxial and have opposite signs which are essential several applications. The dispersion relations for optical iso-frequency surfaces for the momentum vector and permittivity are, $k_x^2/\varepsilon_{zz} + k_y^2/\varepsilon_{zz} + k_z^2/\varepsilon_{xx} = \omega^2/c^2$ and $k_x^2/\varepsilon_{xx} + k_y^2/\varepsilon_{xx} + k_z^2/\varepsilon_{xx} = \omega^2/c^2$ for TM- and TE-polarized waves, respectively. Where $\varepsilon_{xx} = \varepsilon_{yy} = \varepsilon_{||} \neq \varepsilon_{zz} = \varepsilon_\perp$. Here, k_x, k_y, and k_z are the x, y and z components of the wave vector, respectively, ω is the wave frequency, and c is the speed of light. LiNbO$_3$ supports spherical or elliptic iso-frequency in the TE-polarization, and it shows hyperbolicity in the TM case. Using in-plane ($\omega_{T0,\perp}$ and $\omega_{L0,\perp}$) and out-of-plane ($\omega_{T0,||}$ and $\omega_{L0,||}$) transversal and longitudinal phonon vibrations, the dielectric constant of LiNbO$_3$ in the THz range can be described by a Lorentz oscillator model as [76,77]

$$\varepsilon_u = \varepsilon_{\infty,u} - \frac{(\varepsilon_{0,u} - \varepsilon_{\infty,u})\omega_{T0,u}^2}{\omega_{T0,u}^2 - \omega^2 + i\omega\gamma_u}, \tag{5.2}$$

where u stand for $= \perp$ or $||$. At room temperature, the dielectric parameters are $\varepsilon_{\infty,||} = 19.5$, $\varepsilon_{0,||} = 41.5$, $\gamma_{||} = 17.0$ cm^{-1}, $\omega_{T0,||} = 153.5$ cm^{-1}, $\varepsilon_{\infty,\perp} = 10.0$, $\varepsilon_{0,\perp} = 26.0$, $\gamma_\perp = 28.0$ cm^{-1}, $\omega_{T0,\perp} = 253.5$ cm^{-1}, Lyddane-Sachs-Teller relation, ($\omega_{L0,u} = \omega_{T0,u}\sqrt{\varepsilon_{0,u}/\varepsilon_{\infty,u}}$), $\omega_{L0,||} = 224.2$ cm^{-1} and $\omega_{L0,\perp}$

$= 408.8$ cm^{-1}. Depending on the sign of the real part of the relative permittivity in a given direction, LiNbO$_3$ can have one of the two terahertz hyperbolicity bands [76]. For type I hyperbolic bands, $\omega_{T0,\|} = 253.5$ cm^{-1} and $\omega_{L0,\|} = 408.8$ cm$^{-1;}$ for type II hyperbolic bands, $\omega_{T0,\|} = 153.5$ cm^{-1} and $\omega_{L0,\|} = 224.2$ cm^{-1}.

5.3.1 Surface plasmon and hyperbolic phonon polariton dispersion

The first objective of this work was to numerically the characteristics of HPPs of LiNbO$_3$, SPPs of graphene and the combined effects on these dispersion modes in the THz range. The dispersion modes for graphene integrated layered material can be determined from the Fresnel's total reflection coefficient [78]. The reflection coefficient of TE-polarized and TM-polarized waves propagating in the normal direction from the air side in each layered structure (as differentiated in Fig. 1) can be generally expressed as (see chap. 2.3),

$$r_{123}^p = \frac{r_{12}^p + r_{23}^p e^{2ik_{2z}^p t}}{1 + r_{12}^p r_{23}^p e^{2ik_{2z}^p t}},\tag{5.3}$$

$$r_{123}^S = \frac{r_{12}^S + r_{23}^S e^{2ik_{2z}^S t}}{1 + r_{12}^S r_{23}^S e^{2ik_{2z}^S t}},\tag{5.4}$$

where the subscripts 1, 2, and 3 correspond to the air, ferroelectric material, and substrate, respectively. Graphene is treated as a 2D conducting sheet in the reflection coefficient calculation while solving Maxwell's equation with appropriate boundary conditions [79]. The reflection coefficient $r_{12}^{S,p}$ and $r_{23}^{S,p}$ (for figure 2.2b) is given by (see chap. 2.2),

$$r_{12}^p = \frac{k_{1z}^p \varepsilon_{2,\perp} - k_{2z}^p \varepsilon_1 + \frac{\sigma_1 k_{2z}^p k_{1z}^p}{\varepsilon_0 \omega}}{k_{1z}^p \varepsilon_\perp + k_{2z}^p \varepsilon_1 + \frac{\sigma_1 k_{1z}^p k_{2z}^p}{\varepsilon_0 \omega}},\tag{5.5}$$

$$r_{23}^p = \frac{k_{2z}^p \varepsilon_3 - k_{3z}^p \varepsilon_{2,\perp} + \frac{\sigma_2 k_{2z}^p k_{3z}^p}{\varepsilon_0 \omega}}{k_{2z}^p \varepsilon_3 + k_{3z}^p \varepsilon_{2,\perp} + \frac{\sigma_2 k_{2z}^p k_{3z}^p}{\varepsilon_0 \omega}}, \tag{5.6}$$

$$r_{12}^s = \frac{k_{1z}^s - k_{2z}^s - \sigma_1 \mu_0 \omega}{k_{1z}^s + k_{2z}^s + \sigma_1 \mu_0 \omega}, \tag{5.7}$$

$$r_{23}^s = \frac{k_{2z}^s - k_{3z}^s - \sigma_2 \mu_0 \omega}{k_{2z}^s + k_{3z}^s + \sigma_2 \mu_0 \omega}, \tag{5.8}$$

where $k_{1z}^p = \sqrt{\varepsilon_1 k_0^2 - k_x^2}$, $k_{2z}^p = \sqrt{\varepsilon_\perp k_0^2 - \frac{\varepsilon_{2,\perp}}{\varepsilon_{2,\parallel}} k_x^2}$, $k_{3z}^p = \sqrt{\varepsilon_3 k_0^2 - k_x^2}$, $k_{1z}^s = k_{1z}^p$, $k_{3z}^s =$

$\sqrt{\varepsilon_3 k_0^2 - k_x^2}$, and $k_{3z}^s = k_{3z}^p$ are propagation vector in perpendicular direction at each medium, k_x, is the tangential component of the wavevector along the propagation direction (x-direction) that gives general dispersion modes. μ_0 and ε_0 are permeability and permittivity in vacuum, respectively. The Fresnel coefficients for figure a is evaluated by setting $\sigma_1 = \sigma_2 = 0$ in and for figure b $\sigma_2 = 0$.

5.3.2 Purcell factor

There are significant effects of the surface plasmon-phonon modulated light-matter interaction of graphene in the hyperbolic material on the lifetime of SE processes of quantum emitters in the THz range. The competing SE rate (Purcell spectra) [80,81,82] in the presence of a dipole emitter oriented in the z-direction (perpendicular, $\boldsymbol{P} = p_z \hat{z}$) above a semi-infinite plane (the three schematics in Figure 1) normalized by the emission of dipoles in free-space is (see chap. 2.4)

$$\frac{\Gamma}{\Gamma_0} = 1 + \frac{3}{2k_0^3} Re \left(\int_0^\infty \frac{r_{123}^p e^{2ik_{1z}d} k_x^3 dk_x}{k_{z1}} \right), \tag{9}$$

where $\Gamma_0 = \frac{\omega_0^3 |p_z|^2}{3\pi\varepsilon_0 \hbar c^3}$ is the spontaneous emission rate of a dipole in free-space, $k_{z1} = \sqrt{\varepsilon_1 k_0^2 - k_x^2}$, and r_{123}^p is the TM- polarized total reflection coefficient of a give layered medium. The choice on perpendicular orientation in this work is mainly for parallel oriented dipole leads to SE rate into SPs of a single emitter gives half the corresponding value to the same perpendicular emitter direction to the [81,83]. Figure 5.1 depicts the schematics of three structure configurations to study HPPs of ferroelectric and SE rates of a thin slab on substrate (c) structure. A graphene on the surface of the ferroelectric slab and (d) ferroelectric sandwiched between two graphene layers (e). The graphene layers are connected in such a way that an external voltage source can be used to modulate its optical properties.

5.4 Surface plasmon and hyperbolic Phonon polariton dispersion

5.4.1 Graphene surface plasmon chemical potential

First, we investigate independently the optical response of an infinite graphene sheet in air and in a thin slab of $LiNbO_3$ on substrate in low terahertz frequencies. In figure 5.2 (a, b) we plot the propagation vector and wavenumber of highly doped freely suspended graphene for chemical potentials $\mu_c = 0.1$ eV and $\mu_c = 0.3$ eV, obtained from the false color map of the imaginary part of the Fresnel reflection coefficient ($Im\ (r^p)$) for a TM-mode incident field using Eq (5.5). In freely suspended graphene the surrounding dielectric permittivity is set one. The bright false color are indicators of the surface confined electromagnetic waves created due to the incident light coupling with the electrons known as surface plasmon polaritons (SPPs). Increment of the chemical potential shift the narrow bright region to lower k_x due to energy loss of the incident light and smaller propagation loss. The confinement of SPPs towards lower k_x, is verified in both experimental and theoretical works [84,85,86,87].
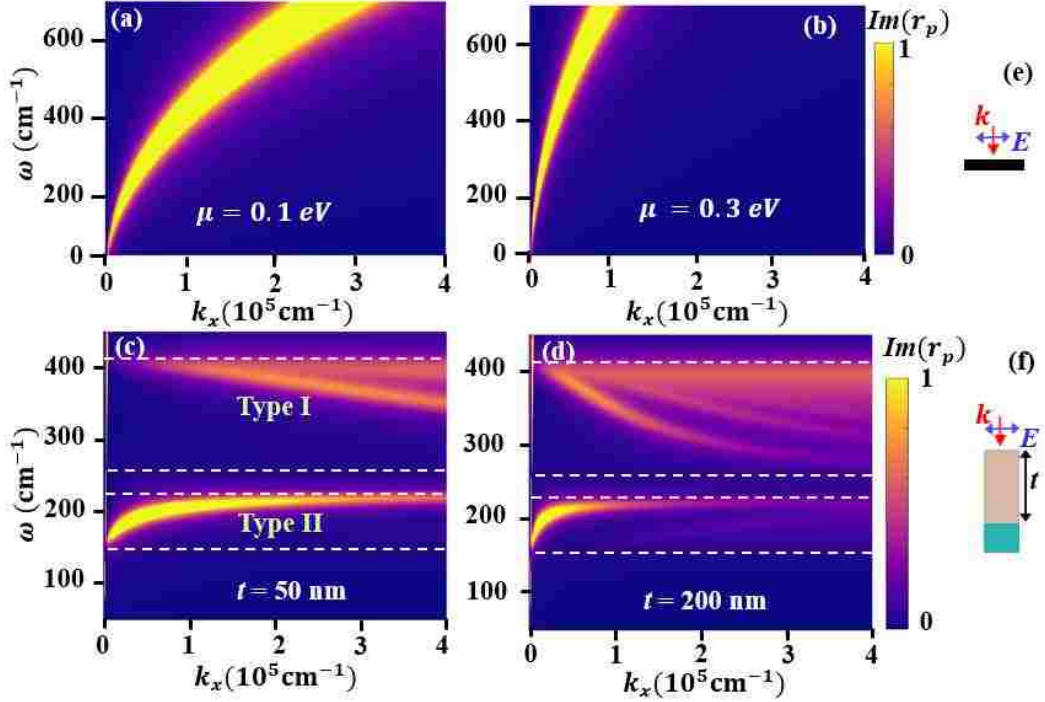
Figure. 5.2. (a) and (b) TM-polarized illumination-induced surface plasmon dispersion strength color maps from the imaginary part of the reflection coefficient for two selected Fermi-energies of free-standing graphene. (c) and (f) dispersion hyperbolic-phonon-polariton of 50 nm and 200 nm thickness of the LiNbO$_3$ slab on a substrate of the type I and II hyperbolic band ranges (white dashed lines).

In graphene, higher chemical potential increases both the real and imaginary parts of the conductivity of graphene, thereby reducing the confinement surface modes far from small wavelengths. Graphene can also support surface plasmons for TE-polarized fields for specific frequency intervals [88,89,90]. Loosely bound propagating TE SPPs can be achieved when the imaginary part of the conductivity has a negative sign, Im(σ) < 0, [91], which is further away from the THz range [89] of our focus. Thus, we are interested in the effects of TM SPPs in the hybridization process.

5.4.2 Ferroelectric LiNbO₃ hyperbolic layer phonon polariton

To understand the behavior of phonon-polariton modes of thin LiNbO₃ on the top of dielectric substrate ($\varepsilon_3 = 2.5$) without graphene, a color map ($Im\ (r^p)$) of Eq. (5.3) is calculated by combining Eq (5.6) and Eq (5.7) while $\sigma_2 = 0$. Figure 5.2(c and d) depicts results of two different LiNbO₃ thicknesses, $t = 50$ and 200 nm. The dispersion consists of two distinguishable (enclosed by dashed white lines) highly quantized dispersive local density of states often referred to as hyperbolic-phonon-polaritons (HPPs), analogous to studies in hBN and Bi₂Se₂ [92]. These modes are standing waves propagating inside the ferroelectric. The HPP modes are bounded inside the hyperbolic band region (type I and type II). From figure 5.2(a) the HPP modes monotonically increase for small k_x and become flat at large k_x at higher frequency in the type II region, while in the type I energy band, large k_x exist towards lower bound frequencies. The opposite HPP modes result in negative group velocity in type II and positive group velocity in type I, implying opposite natured results in anomalous reflections as measured experimentally in other hyperbolic metamaterials [93]. Compared with that of most conventional natural hyperbolic media, the dispersion bands in LiNbO₃ are towards positive bands at higher frequency. However, artificially using two or more different material combinations can be achieved as it is shown in [94]. It is important to emphasize that the number of quantized HPP modes gradually increases in hyperbolic material with t figure 5.2(d). After a few hundreds of nm of t, the number of dispersion modes rises to that of semi-infinite bulk hyperbolic LiNbO₃, a limit which is not shown here.

5.5 Hybrid graphene ferroelectric LiNbO₃ system

5.5.1 Hyperbolic ferroelectric layer single graphene hybridized modes

Next, the heterostructure structure graphene/ferroelectric/substrate system figure 5.1(b) for TM incident light is investigated. The dispersion properties of for three chemical potentials, $\mu_c = 0.1$ eV, 0.3 eV, and 0.6 eV, and ferroelectric layer, $t = 50$ nm and 200 nm, calculated using Eq (5.3) are given in figure 5.3. The first observation due to addition of graphene is the presence of strong dispersion above the type I, between the two bands, and below type II energy range of the ferroelectric LiNbO₃. These dispersion modes are not purely graphene SPPs or ferroelectric HPPs, but rather a combination effect regarded as hybridized surface plasmon phonon–polaritons (HSPPPs) modes. For low chemical potential $\mu_c = 0.1$ eV, figure 5.3 (a, and d), these modes appear just above type I hyperbolicity. Increasing the Fermi energy to $\mu_c = 0.6$ eV leads to increasing HSPPPs modes further away from type I band with high energy while the momentum shifts to lower k_x. The shift in momentum towards the light cone indicates that the chemical potential results in weakly confined HSPPPs. This is different from graphene SPPs, where the dispersion follows $\omega \propto \sqrt{k_x}$, as in figure 5.2(a, b). HSPP modes in the region above the upper limit of type I exhibit nearly linear dispersion and indicate neither pure graphene effect. Most importantly, as the t increases for the same chemical potential, HSPPPs modes above the type I band region stay the same as a further illustration of graphene-dominated hybridization. Inside the type I band, for low chemical potential, the HPPs modes are observed while pushed further to higher k_x with more negative slope. In addition, increasing the chemical potential also leads to a significant decrease in the phonon density of states.
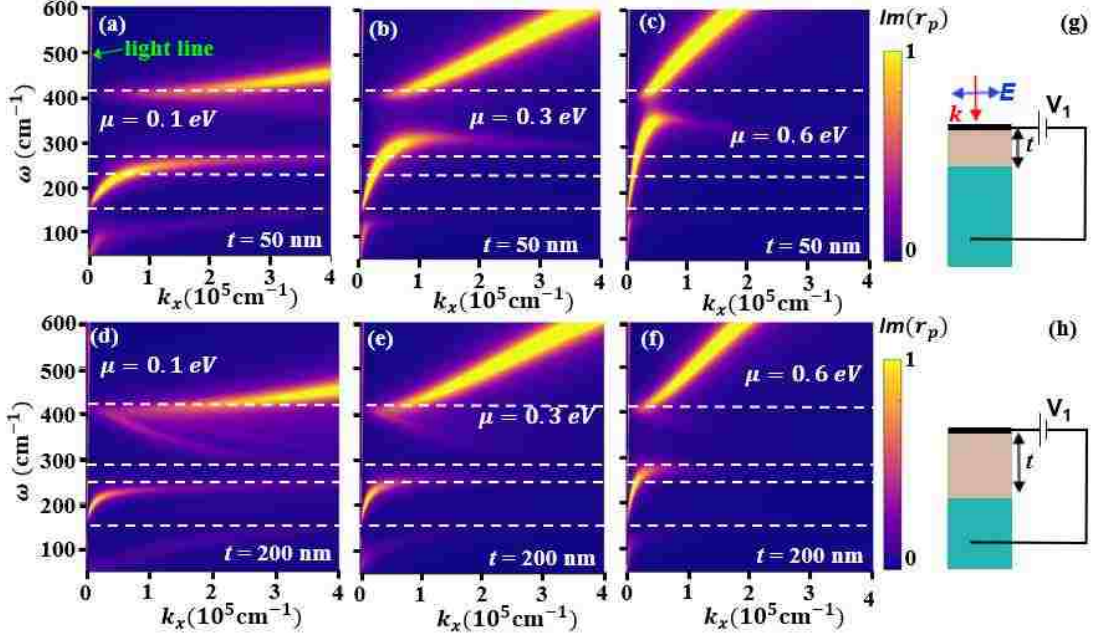
Figure 5.3. TM-polarized illuminated surface plasmon dispersion strength color map of the imaginary part of the reflection coefficient for three selected chemical potential for air/graphene/LiNbO$_3$/substrate. The thickness of the ferroelectric is 50 nm for (a – c), 200 nm for (d – f). TM- polarized field direction 2D schematic of the structure is shown in (c).

Above the lower limit of type II band, HPP modes become strongly dependent on the graphene SPPs hybridization. Near the lower k_x the dispersion shows HPPs. But as the momentum increases, the dispersion that crossed above the type II band reverse towards inside the type II energy. The movement is due to the momentum strength of HPPs and the SPPs at lower frequency are strong towards small k_x. The shift of the HSPPs above type II bands weakens for large t. In the case of frequencies below the lower limit of the type II region, independent of size of the ferroelectric, additional dispersion modes are observed for $\mu_c = 0.1$ eV at lower k_x and frequencies. These weak nonlinear dispersion curves attain flat values of higher k_x in the lower limit of type II band. Since none of these modes were observed in ferroelectric/substrate system, only graphene SPPs can lead to their formation. This is further elaborated by the rise of chemical potential. Higher chemical potential pushes these modes to lower k_x, merging with the light cone for $\mu_c = 0.6$ eV, as in figure 5.3.

5.5.2 Hyperbolic ferroelectric layer double graphene hybridized modes

5.5.2.1 Identical double graphene hybrid HSPPs

An additional system we considered for the hybridization process of HSPPs is the placement of a surface plasmon source on either side of the ferroelectric LiNbO$_3$, the structure shown in figure 5.1(c). Figure 4.4(a – i) displays the results of a thin LiNbO$_3$ layer sandwiched between two graphene layers for equal chemical potential; we consider them as symmetric sources. For $\mu_1 = \mu_2 = 0.1$ eV, the hybridized modes both appear outside the two-band reststrahlen with longer wavevectors. The HSPPs modes in the type II band are pushed outside it is upper limit for thin ferroelectric slab extending in to type I band. When the ferroelectric film thickness increases, the number of phononic modes moves towards the type II band region.
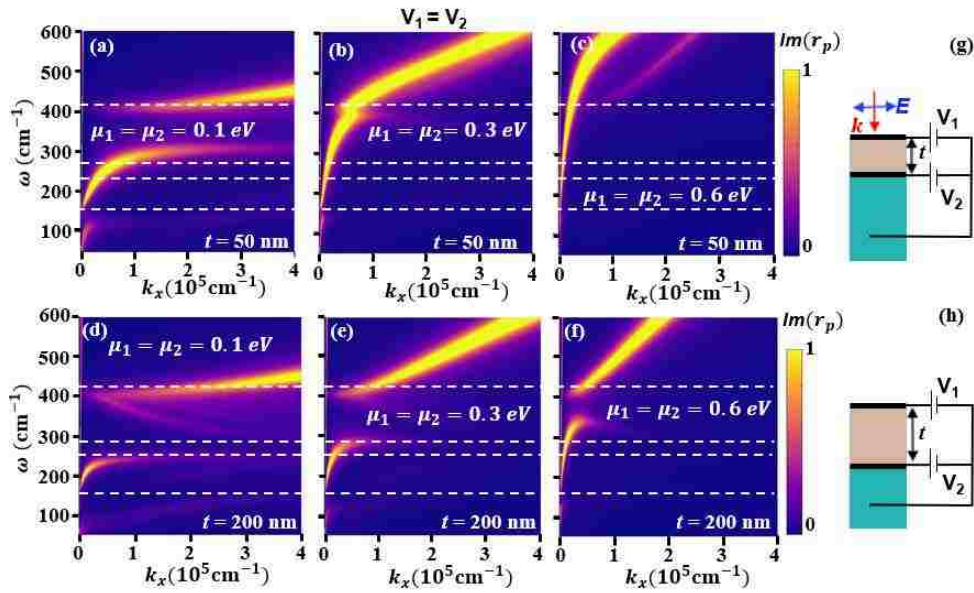

Figure 5.4. TM polarized illuminated surface plasmon dispersion strength color map of the imaginary part of the reflection coefficient for three selected Fermi-energies of free air/graphene/LiNbO$_3$/graphene/substrate. The thickness of the ferroelectric is 50 nm for (a) (b) and (c), 100 nm for (d) (e) and (f), 200 nm for (g) (h) and (i) and $\mu_1 = \mu_2$.

To efficiently excite the HSPPs to higher resonance and minimize the loss, we increased the chemical potential of the two graphene layers to $\mu_1 = \mu_2 = 0.3$ eV and $\mu_1 = \mu_2 = 0.6$ eV. The effect of the chemical potential becomes prominent above the upper limit of type II for chemical potential 0.3 eV, and for 0.6 eV the wavevectors are pushed to larger wavelengths, close to the light cone. For films less than 50 nm, the hybrid modes are dominated by the graphene surface plasmon. It is important to notice that for 0.6 eV, separate weak and strong HSPP modes are obtained, contrary to the case of two-graphene separated by a vacuum or dielectric crystal where the graphene surface plasmon modes merge together at higher energies. However, such claims are noticeable for equal chemical potential and $t = 100$ nm. Compared to single graphene system nearly above type I band linear dispersion is exhibited for larger t and larger chemical potential. In the intermediate condition, graphene-like nonlinear HSPP dispersion can exist. This analysis indicates that linear and nonlinear frequency and momentum dependent excited HSPPs can be controlled through the applied voltage. The dielectric function of the hyperbolic material and its size strongly affects the dispersion mode below the upper limit of the type I region. In general, unlike for single-layer graphene, double-layer graphene systems show strong hybridization effects. This represents a significant advantage over graphene/ferroelectric/substrate systems where the hybridization process needs a large chemical potential. The above analysis also shows the possibility to cause mixed modes, as is seen in the case of the highly influenced dispersion.

5.5.2.2 Dissimilar graphene ferroelectric HSPPs

Since we are interested in producing delicate HSPPs modes, we need a significantly high gate difference. Therefore, the ferroelectric enclosed between two graphene systems and gated by dissimilar chemical potential is calculated, with the results shown in figure 5.4(a – d). In these systems, to control the hybridization process we focus on the chemical potential of one of the top

graphene monolayers while keeping the other fixed. First, we consider a chemical potential $\mu_{c,1}$ = 0.1 eV for the graphene at the top of the ferroelectric and μ_2 = 0.6 eV for the bottom graphene layer with a constant thickness, t = 50 nm. In the region above the type I hyperbolic band there exist two distinct HSPP dispersion bands because high chemical potential leads to higher k_x. The first HSPP curve which is close to the light cone comes from the bottom graphene while the second curve with higher momentum is from the graphene on the top of ferroelectric. Increasing the chemical potential of the top graphene to μ_1 = 0.3 eV pushes the second dispersion mode close to the light cone. Gate modulation of hybrid modes between two dissimilar graphene layers shows that formation of symmetric and antisymmetric electric fields between two graphene sheets separated by a vacuum [95,96,97], dielectric between the two graphene [98], and hyperbolic slab [40], are a result of phase difference.
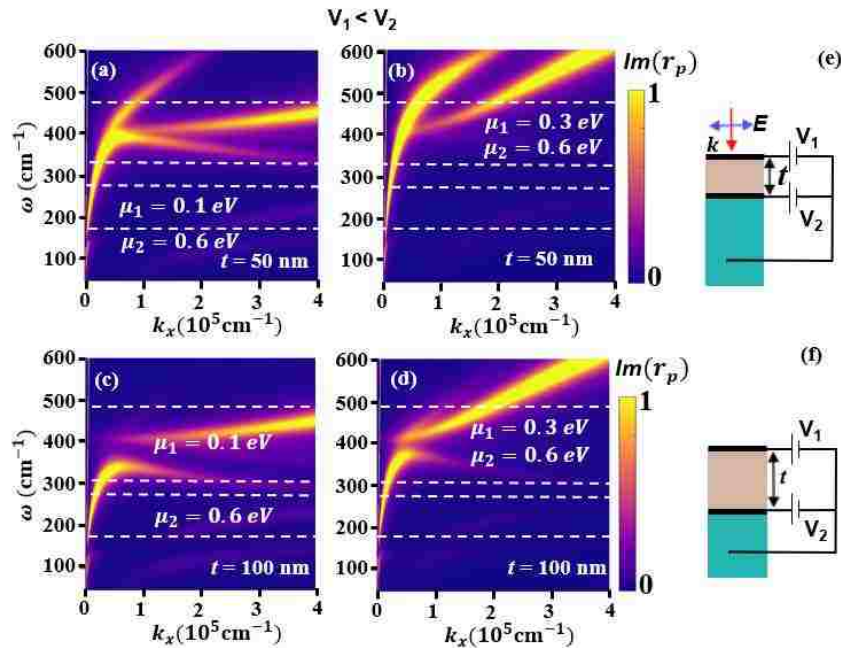

Figure 5.5. TM polarization illuminated surface plasmon dispersion strength color map of the imaginary part of the reflection coefficient for different Fermi-energies for the top and lower parts of a graphene free air/graphene/LiNbO₃/graphene/substrate. The thicknesses of the ferroelectric are (a – b) 50 nm and (c – d) 100 nm. (e) 2D schematics of ferroelectric layer sandwiched between dissimilar graphene ($\mu_1 \neq \mu_2$).

When the two graphene sheets are gated with identical chemical potentials, the dispersion modes merge together as shown in figure 5.4(c). At higher frequencies, through selective asymmetric chemical potential, it is also possible to obtain single HSPPs, as shown in figure 5.5 (c – d), for large k_x as reported by [40, 99]. In addition, for ferroelectric thickness t = 100 nm, the HSPPs mode converge, creating weak coupling of the momentum. The larger the separation of the two graphene sheets, the weaker the interaction, hence the graphene's acting as identical graphene even with different chemical potential. The effect of the dispersion for large wavevectors comes from the top graphene as evidenced in the figure 5.3 and figure 5.4 when the chemical potential is 0.3 eV. In the region below the upper limit of the type I hyperbolicity, μ_1 = 0.1 eV for t = 50 nm and 100 nm, strong HSPP modes are found for higher frequency and low k_x and shift to lower frequency as the k_x increases. The HSPP modes here cross into the type I range for lower k_x and higher frequencies and return for larger k_x towards the lower limit of the type II band and stay flat. It is also noticeable that at lower frequencies, additional surface modes are below the minimum wavenumber of the type II band. These dispersion modes don't cross the lower frequency range of the type II and stay flat for higher k_x when μ_1 = 0.6 eV for t = 50 nm and 100 nm from Figure 5. As in a symmetric graphene system, above type I hyperbolic region one can find several HSPP modes for the same momentum, k_x, for t = 50 nm. Such cases are less observed for t = 200 nm and even larger t values. An additional effect observed is when we have two graphene sheets, the linear dispersion behavior observed in a specific energy range is not seen, compared to single graphene. The variation of the top graphene and bottom graphene chemical potential offers a great means to break the symmetric nature of the hybridization behavior for thin ferroelectric films, as opposed to the thick case where the total effect appears as if the chemical potential was symmetric.

5.6 Spontaneous emission (Purcell factor) in 2D and hyperbolic hybrid material

5.6.1 SE rate in hyperbolic ferroelectric layer single graphene

In this section, we consider the problem of the SPPs and HPPs mixing in SE. Plasmon modulated local density of state of hyperbolic material lead so temporal modulation of near and far field emission of radiation. The strength of SE rate related to the available hybrid mode and local density of states. We validated SE rate modulation numerically from Eq. (5.9) by impressed dipole comparing results from thin ferroelectric layer and graphene gated ferroelectric layer.
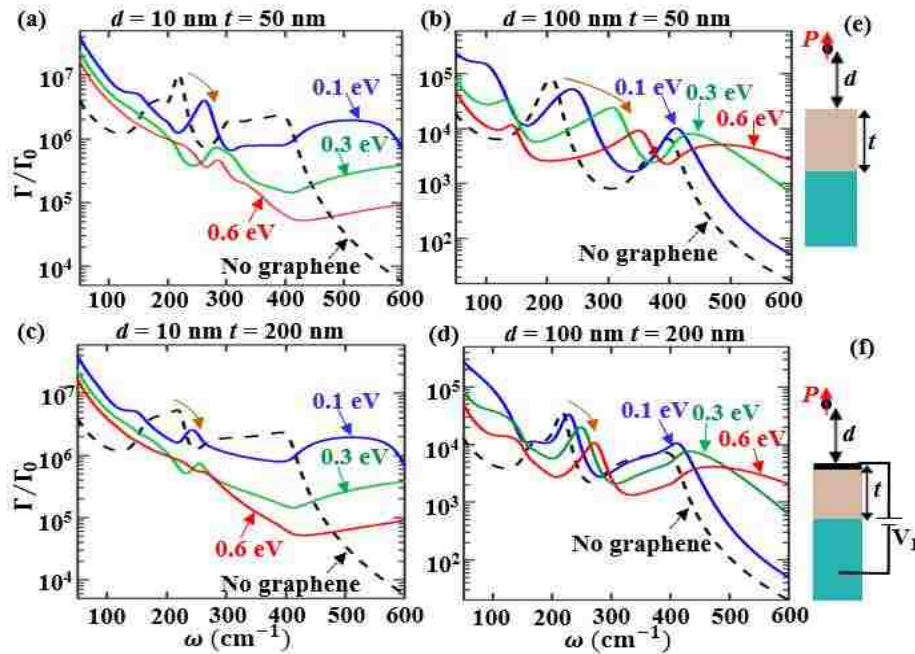
Figure 5.6. Rate of spontaneous emission of different dipole distances modulated with different Fermi energies. The results show the SE as a function of distance of point dipole located in the air medium and frequency for air/graphene/LiNbO$_3$/substrate (2D schematics, f) when $\mu = 0.0$ the system reduces to air/LiNbO$_3$/substrate (2D schematics, e). (a) $d = 10$ nm (b) $d =100$ nm for ferroelectric thickness of 50 nm. (c) $d = 10$ nm (b) $d = 100$ nm for ferroelectric thickness of 200 nm. 2D schematics of dipole orientation and location without graphene (e) and with graphene (f), respectively

In figure 5.6 we plot the SE emitter positioned on the z axis at a distance d in the air medium oriented in the z direction (2D schematics e and f) obtained from Eq (5.9). The green line with

the legend $\mu_c = 0.0$ (without graphene), indicates the HPPS response for the point dipole evaluated from Eq (5.9) of LiNbO3 thin layer on a substrate. SE resonant peak spectral enhancements were in the order of 10^7 and 10^6, respectively for $t = 50$ nm and 200 nm for $d = 10$ nm, as shown in figure 5.6(a and c). The peak resonances can be traced back to the HPPs in figure 5.2 (c-d). The location of the peak position of the spontaneous emission is near the upper limit frequency of the type I and type II regions. Also, the sharp dip in the SE in the two Restrahallan band corresponds to the location where the perpendicular permittivity is $\varepsilon_\perp \sim 0$. Increasing the emitter separation to $d = 100$ nm causes the emission spectrum to be lowered by nearly a factor of 100 and narrows the spectrum width, as shown in figure 5.6(b and d). The emission rate also rapidly decreases with the increasing thickness of LiNbO$_3$ from 50 nm to 200 nm and is independent of the dipole position. However, these decay rate process variations will not change with LiNbO$_3$ thickness after a few 100 nm, which is not shown here. In the case of graphene inclusion graphene on the top ferroelectric, the SE rate decreases inside the two-band region due to the temporal modulation of the local density of states as discussed in the dispersion mode of adding graphene. For a dipole close to the graphene, $d = 10$ nm the SE rate is dominated by graphene outside HPPs. Significance of the graphene property is observed from gradual shifts to higher energy with the chemical potential in the type II band disappear due to graphene plasmon dominance (red arrow) in figure 5.6 (a-d). Above the Type I band region the chemical potential contributes by increasing the emission rate due to HSPPs modes (blue arrow). However, the strength of the SE becomes weaker as the chemical potential gets higher. As the dipole is positioned farther away, $d = 100$ nm, a lower spontaneous emission rate is calculated, largely because the evanescent waves with penetration depths below the dipole distance no longer contribute to the emitter interaction while the peak emission is also stronger. The shift produced by hybridization in the SE peaks is distinctly

separated for the margin of chemical potential selected; the energy SE rate also can reach to the upper limit of the type II band. The major difference for the dipole located at 100 nm with the ferroelectric size is that the spontaneous emission peak shift values are more drastic for $t = 50$ nm than $t = 200$ nm. The height of this peak decreases as d increase and its position is dependent both on d and chemical potential as in Figure 6(b, and d). For a dipole near the graphene, $d = 10$ nm, the SE rate can decrease by a factor of 10 when the chemical potential of the graphene increases to 0.6 eV in the type II band and by a factor of 100 times in the type I region for both ferroelectric $t = 50$ nm and 200 nm figure 5.6(a and c). On the contrary, SE rate in thin ferroelectric remains high at low frequencies where both hyperbolic and mainly surface modes are supported. There is a clear trained showing that SE rate can increased from 10^2 to 10^3, for dipole far from the hybrid system and when the dipole is nearer, above the Type I band.

5.6.2 SE rate in hyperbolic ferroelectric layer in double graphene
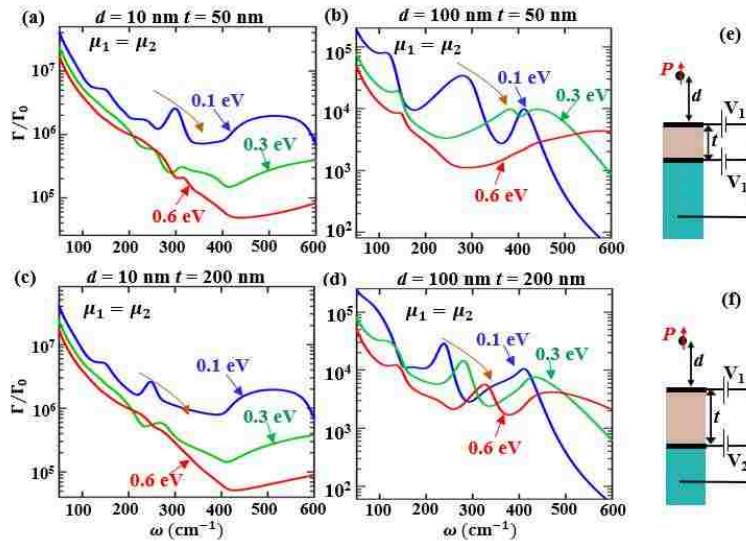

Figure 5.7. Rate of SE of different dipole distance modulated with different Fermi energy. The result shows the Purcell factor as a function of distance of dipole located in the air medium and frequency for air/graphene/LiNbO$_3$/graphene/substrate identical graphene (a) $\mu_1 = \mu_2$, **(a)** d = 10 nm, t = 50 nm (b) d = 100 nm for $t = 50$ nm (c) $d = 10$ nm, $t = 200$ nm and (d) $d = 100$ nm, $t = 200$ nm respectively. (e) identical graphene ($\mu_1 = \mu_2$) sandwiched ferroelectric layer point dipole location.

When a graphene is introduced on the top and bottom of LiNbO$_3$ figure 5.7 (e), SE rate effectively changes. We use identically gated graphene for SE calculation. When $\mu_1 = \mu_2 = 0.1$ eV, small peaks are observed in the Type II band and the peaks in Type I band vanishes. The peaks show similar trained when there is single graphene and without graphene for $d = 10$ nm for $t = 50$ nm and $t = 200$ nm. The nature of this peaks is from HPPs than HSPPS since weak hybrid mode exists in this band, figure 5.4 and 5.5. As the chemical potential of both graphene increases to 0.6 eV HSPPs mode contribution dominates by flattening the SE rate in Type II band. Distinct resonance SE peak shift in Type II band are more noticeable in double graphene system figure 5.7 (c and d) than single graphene figure 5.6(c and d) when the dipole is located far from the top graphene, $d = 100$ nm. In both single graphene modulated or double graphene modulated ferroelectric the SE rate bellow Type II band is dominated by the properties of graphene. Furthermore, HSPPs modes play opposite roles from those of the SPPs for SE, i.e. suppressing the SE in the hyperbolic regions and enhancing outside the hyperbolic region.

5.7 Conclusion:

In conclusion, we studied heterostructure composed of graphene and ferroelectric film hybrid dispersion modes and SE process in THz range. Comparative analysis of SPPs waves formed in graphene affects the local density of state of the HPPs bands of the ferroelectric film. HSPPs supported can extend beyond the two RS band abounded of the ferroelectric. Lower frequency and large wavevector SPPs mode of graphene couples with the lower band HPPs mode causing the crossing of LiNbO$_3$ lower bound band and increases the group velocity for actively tuned higher chemical potential. This HSPPs mode formed in the lower-frequency region do not extend to large wave vectors. In addition, the HSPPs modes further modulated by the number of graphene in the hybrid system. Increasing the number of graphene from single to double layers allows more HSPPs

inside the effective hyperbolic regions which is performed simultaneous tuning both graphene. Numerically calculated SE rate of the hyperbolic band contribution of LiNbO$_3$ compared with that of the graphene integrated hyperbolic material elucidated both enhancement and reduction are achieved. The HSPPs modes provide a strong enhancement of SE compared to outside the hyperbolic band of the pure ferroelectric layer. There is also a ferroelectric film thickness that can maximize hybridization of HSPPs, especially for small distance radiation source, and thus SE rate. In addition, doubling the graphene layer result in higher modification of SE rate. Therefore, hybrid mode modulation of light matter interactions of 2D material plus ultrathin film of hyperbolic ferroelectric material could lead to potential applications in the area of near field radiation, thermovoltaic devices and in THz waveguiding.

Reference:

[1]. Novoselov, K. S.; Geim, A. K.; Morozov, S. V.; Jiang, D.; Zhang, Y.; Dubonos, S. V.; Grigorieva, I. V.; Firsov, A. A. Electric field effect in atomically thin carbon films. Science 306, 666–669 (2004)

[2]. Novoselov, K. S.; Geim, A. K.; Morozov, S. V.; Jiang, D.; Katsneison, M. I.; Grigorieva, I. V.; Dubonos, S. V.; Firsov, A. A. Two-dimensional gas of massless Dirac fermions in graphene. Nature 438, 197–200 (2005)

[3] Geim, A. K.; Novoselov, K. S. The Rise of Graphene Nat. Mater. 2007, 6, 183–191

[4] Berger, C.; Song, Z.; Li, X.; Wu, X.; Brown, N.; Naud, C.; Mayou, D.; Li, T.; Hass, J.; Marchenkov, A. N.; Conrad, E. H.; First, P. N.; de Heer, W. A. Electronic Confinement and Coherence in Patterned Epitaxial Graphene Science 2006, 312, 1191–1196

[5] B. Wunsch, T. Stauber, F. Sols, and F. Guinea, "Dynamical polarization of graphene at finite doping" N. J. Phys. 8, 318 (2006).

[6] E. H. Hwang and S. Das Sarma, "Dielectric function, screening, and plasmons in two-dimensional graphene" Phys. Rev. B 75, 205418 (2007).

[7] S. A. Mikhailov and K. Ziegler, "New Electromagnetic Mode in Graphene". Phys. Rev. Lett. 99, 016803 (2007).

[8] G. W. Hanson, "Dyadic Green's functions and guided surface waves for a surface conductivity model of graphene". J. Appl. Phys. 103, 064302 (2008)

[9]. F. H. L. Koppens, D. E. Chang, and F. Javier García de Abajo, "Graphene plasmonics: a platform for strong light–matter interactions," Nano Lett. 11, 3370–3377 (2011).

[10]. A. Vakil and N. Engheta, "Transformation optics using graphene," Science 332, 1291–1294 (2011).

[11]12. A. N. Grigorenko, M. Polini, and K. S. Novoselov, "Graphene plasmonics," Nat. Photonics 6, 749–758 (2012).

[12]. T. Low and P. Avouris, "Graphene plasmonics for terahertz to midinfrared applications," ACS Nano 8, 1086–1101 (2014).

[13] W. Zhu, I. D. Rukhlenko, L. Si, and M. Premaratne, "Grapheneenabled tunability of optical fishnet metamaterial," Appl. Phys. Lett. 102, 121911 (2013).

[14]. W. Zhu, I. D. Rukhlenko, L. Si, and M. Premaratne, "Graphene metamaterial for optical reflection modulation," Appl. Phys. Lett. 102, 241914 (2013).

[15] I. D. Rukhlenko, A. Pannipitiya, M. Premaratne, and G. P. Agrawal, "Exact dispersion relation for nonlinear plasmonic waveguides," Phys. Rev. B. 84, 113409 (2011).

[16] S. Law, V. Podolskiy, and D. Wasserman: Towards nano-scale photonics with micro-scale photons: the opportunities and challenges of midinfrared plasmonics. Nanophotonics 2, 103–130 (2013)

[17] W. Streyer, K. Feng, Y. Zhong, A. J. Hoffman, and D. Wasserman, Engineering the Reststrahlen band with hybrid plasmon/ phonon excitations, MRS Commun. 6, 1 (2016).

[18] Luo, X.; Qiu, T.; Lu, W.; Ni, Z. Plasmons in Graphene: Recent Progress and Applications Mater. Sci. Eng., R 2013, 74, 351– 376.

[19] Pellegrino, F.M.D.; Angilella, G.G.N.; Pucci, R. Dynamical polarization of graphene under strain. Phys. Rev. B 2010, 82, 115434:1–115434:9.

[20] Pellegrino F.M.D, Angilella G.G.N, Pucci R: Effect of uniaxial strain on plasmon excitations in graphene. J Phys 2012, 377: 012083.

[21] J.P.F. Leblanc, J.P. Carbotte Effect of dynamical screening on single-particle spectral features of uniaxially strained graphene: tuning the plasmaron ring Phys. Rev. B, 87 (2013), Article 205407,

[22] J. S. Gómez-Díaz and J. Perruisseau-Carrier, "Propagation of hybrid transverse magnetic-transverse electric plasmons on magnetically-biased graphene sheets," Journal of Applied Physics, vol. 112, p. 124906, 2012.

[23] Tymchenko, M.; Nikitin, A. Y.; Martín-Moreno, L. Faraday Rotation due to Excitation of Magnetoplasmons in Graphene Microribbons ACS Nano 2013, 7 (11) 9780– 9787.

[24] Liu, Y.; Willis, R. F. Plasmon-phonon strongly coupled mode in epitaxial graphene Phys. Rev. B 2010, 81, 081406(R)

[25] Yan, H.; Low, T.; Zhu, W.; Wu, Y.; Freitag, M.; Li, X.; Guinea, F.; Avouris, P.; Xia, F. Damping pathways of mid-infrared plasmons in graphene nanostructures Nat. Photonics 2013, 7, 394– 399.

[26] Koch, R. J., Seyller, T. & Schaefer, J. A. Strong phonon-plasmon coupled modes in the graphene/silicon carbide heterosystem. PHYSICAL REVIEW B 82, 201413, (2010).

[27] Hwang, E. H.; Sensarma, R.; Sarma, S. D. Plasmon-Phonon Coupling in Graphene Phys. Rev. B: Condens. Matter 2010, 82, 195406

[28] H. Yan, T. Low, W. Zhu, Y. Wu, M. Freitag, X. Li, F. Guinea, P. Avouris, and F. Xia, Damping pathways of mid-infrared plasmons in graphene nanostructures. Nat. Photon. 7, 394–399 (2013).

[29] R. J. Koch et al, "Robust phonon-plasmon coupling in quasifreestanding graphene on silicon carbide," Physical Review Letters 116, 106802 (2016).

[30] I. J. Luxmoore, C. H. Gan, P. Q. Liu, F. Valmorra, P. Li, J. Faist, and G. R. Nash, Strong coupling in the far-infrared between graphene plasmons and the surface optical phonons of silicon dioxide, ACS Photonics 1, 1151 (2014).

[30] I. J. Luxmoore, C. H. Gan, P. Q. Liu, F. Valmorra, P. Li, J. Faist, and G. R. Nash, Strong coupling in the far-infrared between graphene plasmons and the surface optical phonons of silicon dioxide, ACS Photonics 1, 1151 (2014).

[32] Duo, Q.; Guinea, F.; Deng, B.; Sarpkaya, I.; Li, C.; Chen, C.; Ling, X.; Kong, J.; Xia, F. Electrothermal Control of Graphene Plasmon-Phonon Polaritons Adv. Mater. 2017, 29, 1700566

[33] P. Q. Liu, J. Reno, and I. Brener, "Graphene-induced Strong Quenching of Optical Phonons in III-V Semiconductor Heterostructures," in *Conference on Lasers and Electro-Optics*, OSA Technical Digest (online) (Optical Society of America, 2017), paper FTh3F.8.

[34] J. Schiefele, J. Pedrós, F. Sols, F. Calle, and F. Guinea, Coupling light into graphene plasmons through surface acoustic waves, Phys. Rev. Lett. 111(23), 237405 (2013)

[35] Dai, S.; Ma, Q.; Liu, M. K.; Andersen, T.; Fei, Z.; Goldflam, M. D.; Wagner, M.; Watanabe, K.; Taniguchi, T.; Thiemens, M.; Keilmann, F.; Janssen, G. C. A. M.; Zhu, S.-E.; Jarillo-Herrero, P.; Fogler, M. M.; Basov, D. N.; Graphene on hexagonal boron nitride as a tunable hyperbolic metamaterial. Nat. Nanotechnol. 2015, 10, 682−686.

[36,] V. W. Brar, M. S. Jang, M. Sherrott, S. Kim, J. J. Lopez, L. B. Kim, M. Choi and H. Atwater, Hybrid surface-phonon-plasmon polariton modes in graphene/monolayer h-BN heterostructures, Nano Lett., 2014, 14, 3876–3880.

[37] S. Dai, Q. Ma, M. K. Liu, T. Andersen, Z. Fei, M. D. Goldflam, M. Wagner, K. Watanabe, T. Taniguchi, M. Thiemens, F. Keilmann, G. C. A. M. Janssen, S-E. Zhu, P. Jarillo-Herrero, M. M. Fogler & D. N. Basov. "Graphene on hexagonal boron nitride as a tunable hyperbolic metamaterial". Nature Nanotech. 10, 682-686 (2015).

[38,] A. Woessner, M. B. Lundeberg, Y. Gao, A. Principi, P. Alonso-González, M. Carrega, K. Watanabe, T. Taniguchi, G. Vignale, M. Polini, J. Hone, R. Hillenbrand and F. H. L. Koppens, Highly confined low-loss plasmons in graphene–boron nitride heterostructures. Nat. Mater. 14, 421–425 (2015).

[39] Barcelos, I. D. et al. Graphene/h-BN plasmon-phonon coupling and plasmon delocalization observed by infrared nano-spectroscopy. Nanoscale 7, 11620–11625 (2015).

[40] Kumar, A. et al. Tunable light-matter interaction and the role of hyperbolicity in graphene-hBN system. Nano Lett. 15, 3172–3180 (2015).

[41] C. Baeumer, D. Saldana-Greco, J. M. P. Martirez, A. M. Rappe, M. Shim, L. W. Martin, "Ferroelectrically driven spatial carrier density modulation in graphene". *Nat. Commun.* **6**, 6136 (2015).

[42] Gopalan, K. K.; Janner, D.; Nanot, S.; Parret, R.; Lundeberg, M. B.; Koppens, F. H. L.; Pruneri, V. Mid-Infrared Pyroresistive Graphene Detector on LiNbO$_3$. Adv. Opt. Mater. 2017, 5, in press DOI: 10.1002/ adom.201770025

[43] Sassi, U.; Parret, R.; Nanot, S.; Bruna, M.; Borini, S.; De Fazio, D.; Zhao, Z.; Lidorikis, E.; Koppens, F. H. L.; Ferrari, A. C.; Colli, A. Graphene-Based Mid-Infrared Room-Temperature Pyroelectric Bolometers with Ultrahigh Temperature Coefficient of Resistance. Nat. Commun. 2017, 8, 14311,

[44] Baeumer, C.; Saldana-Greco, D.; Martirez, J. M. P.; Rappe, A. M.; Shim, M.; Martin, L. W. Nat. Commun. 2015, 6, 6136 DOI: 10.1038/ncomms7136

[45] Bidmeshkipour, S.; Vorobiev, A.; Andersson, M. A.; Kompany, A.; Stake, J. Effect of Ferroelectric Substrate on Carrier Mobility in Graphene Field-Effect Transistors. Appl. Phys. Lett. 2015, 107, 173106,

[46] Baeumer, C.; Saldana-Greco, D.; Martirez, J. M. P.; Rappe, A. M.; Shim, M.; Martin, L. W. Nat. Commun.2015, 6, 1– 1.

[47] Hong, X.; Posadas, A.; Zou, K.; Ahn, C. H.; Zhu, J. High-Mobility Few-Layer Graphene Field Effect Transistors Fabricated on Epitaxial Ferroelectric Gate Oxides Phys. Rev. Lett. 2009, 102, 136808.

[48] Rajapitamahuni, A.; Hoffman, J.; Ahn, C. H.; Hong, X. Examining Graphene Field Effect Sensors for Ferroelectric Thin Film Studies Nano Lett. 2013, 13, 4374– 4379.

[49] Jie, W.; Hui, Y. Y.; Chan, N. Y.; Zhang, Y.; Lau, S. P.; Hao, J. Ferroelectric Polarization Effects on the Transport Properties of Graphene/PMN-PT Field Effect Transistors J. Phys. Chem. C 2013, 117, 13747–13752

[50] Baeumer, C.; Rogers, S. P.; Xu, R.; Martin, L. W.; Shim, M. Tunable Carrier Type and Density in Graphene/$PbZr_{0.2}Ti_{0.8}O_3$ Hybrid Structures through Ferroelectric Switching Nano Lett. 2013, 13, 1693–1698

[51] M. D. Goldflam, G. X. Ni, K. W. Post, Z. Fei, Y. Yeo, J. Y. Tan, A. S. Rodin, B. C. Chapler, B. Özyilmaz, A. H. Castro Neto, M. M. Fogler, and D. N. Basov, "Tuning and Persistent Switching of Graphene Plasmons on a Ferroelectric Substrate," Nano Lett. 15(8), 4859–4864 (2015)

[52] Zheng Y., Ni G. X., Toh C. T., Tan C. Y., Yao K. and Özyilmaz B., "Graphene Field-Effect Transistors with Ferroelectric Gating", 2010 Phys. Rev. Lett. 105 166602

[53] Y. Zheng, G. X. Ni, S. Bae, C. X. Cong, O. Kahya, C. T. Toh, H. R. Kim, D. Im, T. Yu, J. H. Ahn, B. H. Hong, and B. Ozyilmaz, "Wafer-scale graphene/ferroelectric hybrid devices for low-voltage electronics" Europhys. Lett. 93(1), 17002 (2011).

[54] Hebling, J., Yeh, K.-L., Hoffmann, M. C., Bartal, B. and Nelson, K. A. Generation of high-power terahertz pulses by tilted-pulse-front excitation and their application possibilities. J. Opt. Soc. Am. B, vol. 25(7): B6–B19, 2008.

[55] Stepanov, A., Hebling, J. and Kuhl, J. Generation, tuning, and shaping of narrow-band, picosecond THz pulses by two-beam excitation. Opt. Express, vol. 12(19): 4650–4658, 2004.

[56] Hoffmann, M. C., Yeh, K.-L., Hebling, J. and Nelson, K. A. Efficient terahertz generation by optical rectification at 1035 nm. Opt. Express, vol. 15(18): 11706–11713, 2007.

[57] Lin, K.-H., Werley, C. A. and Nelson, K. A. Generation of multicycle terahertz phononpolariton waves in a planar waveguide by tilted optical pulse fronts. Applied Physics Letters, vol. 95(10): 103304, 2009.

[58] Hebling, J., Stepanov, A. G., Alm´asi, G., Bartal, B. and Kuhl, J. Tunable THz pulse generation by optical rectification of ultrashort laser pulses with tilted pulse fronts. Applied Physics B: Lasers and Optics, vol. 78(5): 593–599, 2004.

[59] Yeh, K.-L., Hebling, J., Hoffmann, M. C. and Nelson, K. A. Generation of high average power 1 kHz shaped THz pulses via optical rectification. Optics Communications, vol. 281(13): 3567 – 3570, 2008.

[60] Jin, D., Kumar, A., Hung Fung, K., Xu, J. & Fang, N. X. Terahertz plasmonics in ferroelectric-gated graphene. Appl. Phys. Lett. 102, 201118 (2013).

[61] X.Q. Gu, W.Y. Yin, Terahertz wave responses of dispersive few-layer graphene (FLG) and ferroelectric film composite, Opt. Commun., 319 (2014), p. 70.

[62] Gu X. -Q., Yin W. -Y., and Zheng T., Attenuation characteristics of the guided THz wave in parallel-plate ferroelectric-graphene waveguides Optics Communications, Vol. 330. (2014) pp.19-23.

[63] H. Wang, H. Zhao, G. Hu, S. Li, H. Su, and J. Zhang, "Graphene based surface plasmon polariton modulator controlled by ferroelectric domains in lithium niobate," Sci. Rep. 5, 18258 (2015).

[64] H. Wang, H. Zhao, G. Hu, S. Li, H. Su, and J. Zhang, "Graphene based surface plasmon polariton modulator controlled by ferroelectric domains in lithium niobate," Sci. Rep. 5, 18258 (2015).

[65] Kumar, A.; Low, T.; Fung, K. H.; Avouris, P.; Fang, N. X. "Tunable light–matter interaction and the role of hyperbolicity in graphene–hBN system."Nano Lett. 2015, 15 (5) 3172– 3180.

[66] F. H. L. Koppens, D. E. Chang, and F. J. Garc´ıa de Abajo, Graphene Plasmonics: A Platform for Strong LightMatter Interactions. Nano Letters 2011 11 (8), 3370-3377.

[67] R. Filter, M. Farhat, M. Steglich, R. Alaee, C. Rockstuhl, and F. Lederer, "Tunable graphene antennas for selective enhancement of THz-emission," Opt. Express 21, 3737-3745 (2013)

[68] Jamison Sloan, Nicholas Rivera, Marin Soljačić, and Ido Kaminer, "Tunable UV-Emitters through Graphene Plasmonics," Nano Letters 2018 18 (1), 308-313.

[69] Zhang, L., Fu, X., Zhang, M. & Yang, J. Spontaneous emission in paired graphene plasmonic waveguide structures. Opt. Exp. 21, 7897 (2013).

[78] Zenghong Ma, Wei Cai, Yinxiao Xiang, Mengxin Ren, Xinzheng Zhang, and Jingjun Xu, "Dynamic spontaneous emission control of an optical emitter coupled to plasmons in strained graphene," Opt. Express 25, 23070-23081 (2017).

[71] Rivera, N.; Kaminer, I.; Zhen, B.; Joannopoulos, J. D.; Soljačić, M. Shrinking light to allow forbidden transitions on the atomic scale Science 2016, 353, 263– 269.

[72] Koppens, F. H. L.; Chang, D. E.; García de Abajo, F. J. Graphene Plasmonics: A Platform for Strong Light–Matter Interactions Nano Lett. 2011, 11, 3370– 3377.

[73] P. Y. Chen and A. Alù, "Atomically thin surface cloak using graphene monolayers," ACS Nano 5(7), 5855–5863 (2011).

[74] Yan, Y. Zhang, P. Kim, and A. Pinczuk, "Electric Field Effect Tuning of Electron-Phonon Coupling in Graphene," Phys. Rev. Lett. 98(16), 166802 (2007).

[75] M. Liu, X. Yin, E. Ulin-Avila, B. Geng, T. Zentgraf, L. Ju, F. Wang, and X. Zhang, "A graphene-based broadband optical modulator," Nature 474(7349), 64–67 (2011).

[76] D. Jin, A. Kumar, K.H. Fung, J. Xu, N.X. Fang Appl. "Terahertz plasmonics in ferroelectric-gated graphene", Phys. Lett., 102 (2013), p. 201118.

[77] T. Feurer, N. S. Stoyanov, D. W. Ward, J. C. Vaughan, E. R. Statz, and K. A. Nelson, "Terahertz polaritonics," Annu. Rev. Mater. Res. 37, 317–350 (2007).

[78] Born, M.; Wolf, E. Principles of Optics, 6th (with corrections) ed.; Pergamon Press: Oxford, 1980.

[79] L. A. Falkovsky, Optical properties of graphene, J. Phys.: Conf. Ser. 129, 012004, 2008.

[80] Koppens, F. H.; Chang, D. E.; Garcia de Abajo, F. J. Nano letters 2011, 11, 33703377.

[81] M. Cuevas, "Surface plasmon enhancement of spontaneous emission in graphene waveguides," J. Opt. 18(10), 105003 (2016).

[82] S.Haroche, Cavity Quantum Electrodynamics in Fundamental Systems in Quantum Optics, les Houches session LIII. Editors: J. Dalibard, J.M. Raimond and J. Zinn Justin, Elsevier Science Publishers (1992).

[83] Vos, W. L.; Koenderink, A. F.; Nikolaev, I. S. Orientation-dependent spontaneous emission rates of a two-level quantum emitter in any nanophotonic enviroment. Phys. Rev. A: At., Mol., Opt. Phys. 2009, 80, 053802.

[84] Wunsch, B., Stauber, T., Sols, F. & Guinea, F. Dynamical polarization of graphene at finite doping. New J Phys 8, 318, (2006).

[85] Eberlein, T.; Bangert, U.; Nair, R. R.; Jones, R.; Gass, M.; Bleloch, A. L.; Novoselov, K. S.; Geim, A.; Briddon, P. R. Plasmon Spectroscopy of Free-Standing Graphene Films Phys. Rev. B 2008, 77, 233406.

[86] Koch, R. J.; Seyller, T.; Schaefer, J. A. Strong Phonon-Plasmon Coupled Modes in the Graphene/Silicon Carbide Heterosystem Phys. Rev. B: Condens. Matter 2010, 82, 201413.

[87] Liu, Y.; Willis, R. F. Plasmon-phonon strongly coupled mode in epitaxial graphene Phys. Rev. B 2010, 81, 081406(R).

[88] Mikhailov, S. A. & Ziegler, K. New electromagnetic mode in graphene. Phys. Rev. Lett. 99, 016803 (2007).

[89] Kotov, O. V., Kol'chenko, M. A. & Lozovik, Y. E. Ultrahigh refractive index sensitivity of TE-polarized electromagnetic waves in graphene at the interface between two dielectric media. Opt. Express 21, 13533–13546 (2013).

[90] Menabde, S. G., Mason, D. R., Kornev, E. E., Lee, C. & Park, N. Direct optical probing of transverse electric mode in graphene. Scientific Reports 6, 21523 (2016).

[91] Stauber, T. Plasmonics in Dirac Systems: from Graphene to Topological Insulators J. Phys.: Condens. Matter 2014, 26, 123201.

[92] Govyadinov, A.A. et al. Probing low-energy hyperbolic polaritons in van der Waals crystals with an electron microscope. Nature Communications 8, 95 (2017).

[93] Yoxall, E.; Schnell, M.; Nikitin, A. Y.; Txoperena, O.; Woessner, A.; Lundeberg, M. B.; Casanova, F.; Hueso, L. E.; Koppens, F. H. L.; Hillenbrand, R. Direct observation of ultraslow hyperbolic polariton propagation with negative phase velocity. Nat Photon 9, 674-678 (2015).

[94] S.-A. Biehs and P. Ben-Abdallah, "Near-field heat transfer between multilayer hyperbolic metamaterials," Z. Naturforsch. A 72, 115–127 (2017).

[95] Wang B., Zhang X., Yuan X. and Teng J. "Optical coupling of surface plasmons between graphene sheets", J. Appl. Phys. Lett. 2012, 100 (13) 131111.

[96] Ilic O., Jablan M., Joannopoulos J. D., Celanovic I., Buljan H. and Soljačić M. Near-field thermal radiation transfer controlled by plasmons in graphene Phys. Rev. B 2012, 85, 155422.

[97] G. Yin, J. Yang, and Y. Ma, "Near-field heat transfer between graphene monolayers: Dispersion relation and parametric analysis". Applied Physics Express 9, 122001 (2016). 47.

[98] C. H. Gan, H. S. Chu, and E. P. Li, Synthesis of highly confined surface plasmon modes with doped graphene sheets in the midinfrared and terahertz frequencies, Phys. Rev. B 85, 125431 (2012).

[99] de Vega, S.; García de Abajo, F. J. Plasmon Generation through Electron Tunneling in Graphene ACS Photonics 2017, 4 (9) 2367– 2375.

Chapter 6

Summary and Future Direction

In this dissertation's first section, we described adhesion layer contribution on plasmonic gold nanodisk, one of the promising structures and materials for an application such as nanoantenna, nanosensing devices from optical range to near midinfrared. Considering Ti adhesion to gain a general understanding in plasmon response to the effect of noble metals assuming that other adhesion layers tend to show similar optical properties. We analyzed both quantitatively and qualitatively from theoretical standing point light absorption, scattering, and extinction contribution of adhesion material. Spectra of optical responses of single gold nanodisk showed substantial damping of confined plasmon due to Ti. The result concluded gives way to overcome confined plasmon deterioration and provides a useful tool applicable to similar materials and small nanostructure that requires adhesion layer during the fabrication process. Hence, expanding this numerical work to explore other adhesion layers; Cr, Cr_2O_3, TiO_2 and Indium Tin Oxide (ITO), coupling and losses of the confined surface plasmon spectra in a single nanoparticle is one of future prospects. In addition, we look forward to more understanding of the physical mechanism adhesion material contribution in single nanoparticle plasmonic deriving analytical solutions. This will be done solving Maxwell's equation by implementing the quasi-static dipolar approximation method. This will be supported by both experimental and computational results from several literatures summarized as a review chapter and is another direction we hope to address as progress in plasmonics.

The second part of the disseration is devoted to the study of light-matter interactions mediated by anisotropic 2D material illuminated by a plane wave. We presented a newly discovered anisotropic

2D material, black phosphorene, plasmonic properties and effects of dielectric environments. Our results suggest that the surface plasmon properties of black phosphorene of ribbons of different geometrical parameters from mid-infrared to high infrared regimes could be exploited to probe the efficiency of plasmonic enhanced absorption. Furthermore, localized surface plasmon and enhanced absorption of periodic BP nanoribbons are affected strongly by free carrier density. Introduction of shielding thin dielectric, such as hexagonal boron nitride beside preserving the edge mode plasmonic nature of BP, allows for an unprecedented control of the resonance energy. One of the prominent properties of 2D materials is that their optical properties differ based on the number of sub atomic layers. This means the light matter interaction will be different from monolayer to bilayer, etc. Further progress we look forward to addressing on anisotropic plasmonic responses of 2D BP for patterned nanoscale structure (rectangle, disk, etc), ribbon, based on layer dependence. In addition, significant leaps in fabrication of BP with several types of van der Waals (vdW) structure from single layer to multilayer has been achieved in the lab in the past few years. We see this as a great potential area of research possibility in hybridization of surface plasmon from two distinct 2D materials (e.g. BP and graphene) for modulated terahertz metamaterial applications.

At last, we extend the impact of prominent 2D material graphene in combination with hyperbolic heterostructures. The core this part of the thesis deals with the study of hybridization of surface plasmon with hyperbolic phonon polariton modes and implications of the electrostatic gating in low THz. Using the theory of transfer matrix, we show that the monolayer graphene surface plasmon hybridization with hyperbolic phonon polarization local density of state of natural hyperbolic material, ferroelectric $LiNbO_3$. The results achieved elaborate hybridization processes significantly regulated by the electrostatic gated top (single) graphene and top and bottom (double)

graphene layer. By comparing the SE of the hyperbolic band contribution of hyperbolic material with that of the graphene integrated hyperbolic material, elucidated flexible enhancement as well as inhibition of spontaneous emission. Regulating emission of radiation and controlling has been an excellent concept for super Plank radiation (heat transfer beyond Plank radiation limit). A process that requires bringing two objects of temperature, T_1 in one end, and T_2 in the other end ($T_1 \neq T_2$), separation of a few nanometers closer. Such condition leads to EM radiation from coupling of surface hybrid evanescence field and propagation field. Theoretically based on the solution of Maxwell equations via the fluctuation-dissipation theorem, actively controlling radiative heat flux, optimized photon tunneling probability from higher temperature end to lower temperature applying external voltage is a main future work we will address for hybrid graphene ferroelectric systems.

Appendix:

A. Optical constant of gold and Ti
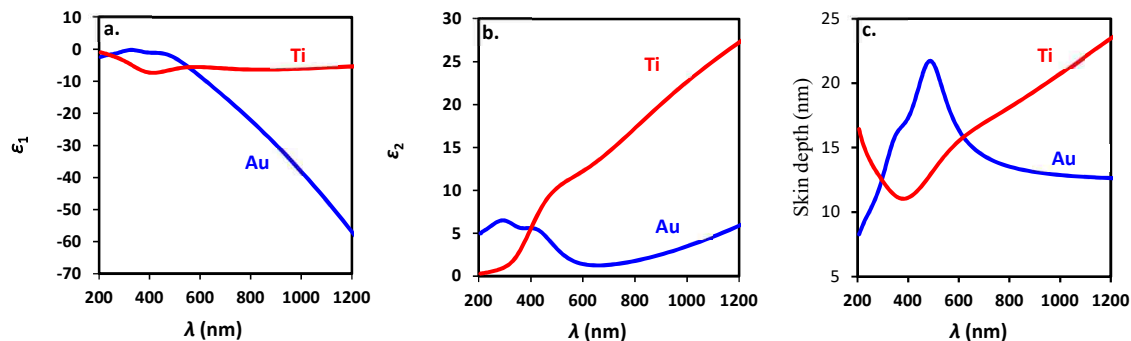
Figure A. S1. Complex dielectric constants of gold and titanium, (a) real and (b) imaginary. (c) Shows calculated skin depth as a function of wavelength for both gold and titanium.

The computational method requires the optical properties of the material; specifically, it requires wavelength dependent dielectric constants of the materials. Figure A (S1 a) is plotted for the real part of the dielectric constant ε_1 for both titanium and gold. In wavelength range ~ 200 nm to ~ 600 nm, Au has slightly higher values relative to Ti, while below 600 nm the real part for Ti remains almost constant while the Au dropped significantly to large negative values. In the case of the imaginary component ε_2 as showed in figure A (S1 b), below 400 nm the Au has larger dielectric constant than Ti, while above 400 nm Ti gets larger than Au. The skin depth, which explains penetration of the electromagnetic field inside metals, is calculated for the optical to mid-infrared regimes and shown in figure A (S1 c). The skin depth of Au ranges from $7 - 23$ nm while for the Ti the range is from $13 - 24$ nm. The amplitude of Au skin depth drastically increases up to wavelengths of 500 nm and drops significantly until 750 nm, and then remains nearly constant after 750 nm. In case of Ti skin depth decreases from 200 nm to 400 nm and increases continuously from 400 nm to higher infrared.

B.1. Spectrum of Gold nanodisk with adhesive layer

To illustrate more the shift of resonance mode, we introduce Figure B (S2) that presents the inherent optical interaction efficiencies based on nanodisk size. The specific focus of the examples shown in figures B (S2 a–c) is to demonstrate the changing plasmonic behavior of calculated absorption scattering and extinction spectra for all the diameters (D = 75, 100, 120, 140 150, 160, 175 180 and 200 nm) for adhesion layer thickness of 5 nm. The spectral profile broadens as the size increases for all diameters. A large shift of the dipole peak and a much more complex spectrum occur when the particle radius is increased further. The absorption and the extinction show similar variations, with a small secondary peak, contribution from higher order modes. This concept can be verified by calculating the surface charge distribution.
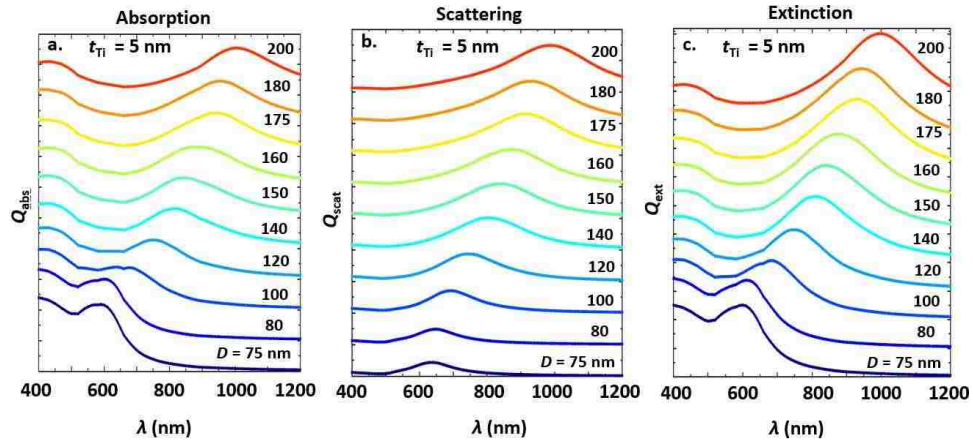
Figure B. S2. Comparison of the spectra of composite disks of titanium adhesion layer thickness (t_{Ti}) = 5 nm and the gold layer thickness (t_{Au} = 15 nm) as a function of wavelength. (a) Calculated absorbed spectra (b) scattering spectra, and (c) extinction spectra. The Au and Ti nanodisks had values for the diameter of 75, 100, 120, 140, 150, 160, 180 and 200 nm.

B.2 Surface charge distribution

To do so we implemented simple integral forms of Gauss's law of electrostatic of dielectric medium and visualize computationally the surface charge density as follows. The total charge incudes in a nanoparticle in a dielectric medium is

$$\Phi_E = \frac{Q}{\varepsilon_{eff}\varepsilon_0} = \oiint \mathbf{\hat{n}} \cdot \mathbf{E} dS = \oiint (\mathbf{\hat{x}} \cdot E_x + \mathbf{\hat{y}} \cdot E_y + \mathbf{\hat{z}} \cdot E_z) dS \qquad (B.2.1)$$

where Φ_E is the electric flux through the nanodisk surface S, ε_0 is the permittivity of vacuum, $\mathbf{\hat{n}} = (\mathbf{\hat{x}}, \mathbf{\hat{y}}, \mathbf{\hat{z}})$ is the outward normal unit vector of the metal surface and $\mathbf{E} = (E_x, E_y, E_z)$ is the local confined electric field. The total the surface charge density for metallic structure is located around the outer surface given by:

$$Q = \oiint \rho_s dS \qquad (B.2.2)$$

From Eq. (B.2.1) and (B.2.2) the surface charge distribution of the nanodisk is

$$\rho_s = \varepsilon_0 \varepsilon_{eff}(e_x \cdot E_x + e_y \cdot E_y + e_z \cdot E_z) \qquad (B.2.3)$$

Primarily the quadrupole moment, becoming very distinct in its amplitude as the diameter grow. The main features of the scattering, absorption, and extinction spectra explained in terms of resonant excitation of the dipolar-like, 1st higher, and 2nd higher can be shown based on surfaces charge density in plasmonic structure. FEM simulated using Eq (B.2.3) strong localized surface charge density for plane wave normal incident excited $D = 200$ nm nanodisk is plotted to verify that the modes are formed due to coupling of the strong dipole plasmon resonances of the nanodisks, figure B (S3 e and f) calculated at resonance wavelengths 990 nm. The weak quadrupole nature (resembles higher order) modes near 440 nm becomes apparent from both surface charge density profiles strong localized figure B (S3 a and b). We also included Figure B(S3 c and d) intermediate wavelength 600 nm the transition from higher mode to dipolar mode.
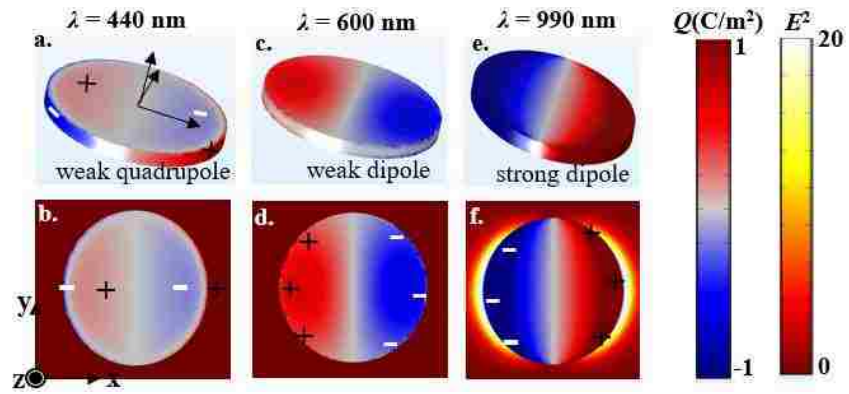
Figure B. S3. Surface charge distribution normalized by (10^-11) and field enhancement of nanodisk D = 200 nm without adhesion Ti layer side and top view; at wavelength of 440 nm (a and b), 600 nm (c and d), and resonant wavelength of 980 nm (e and f), respectively.

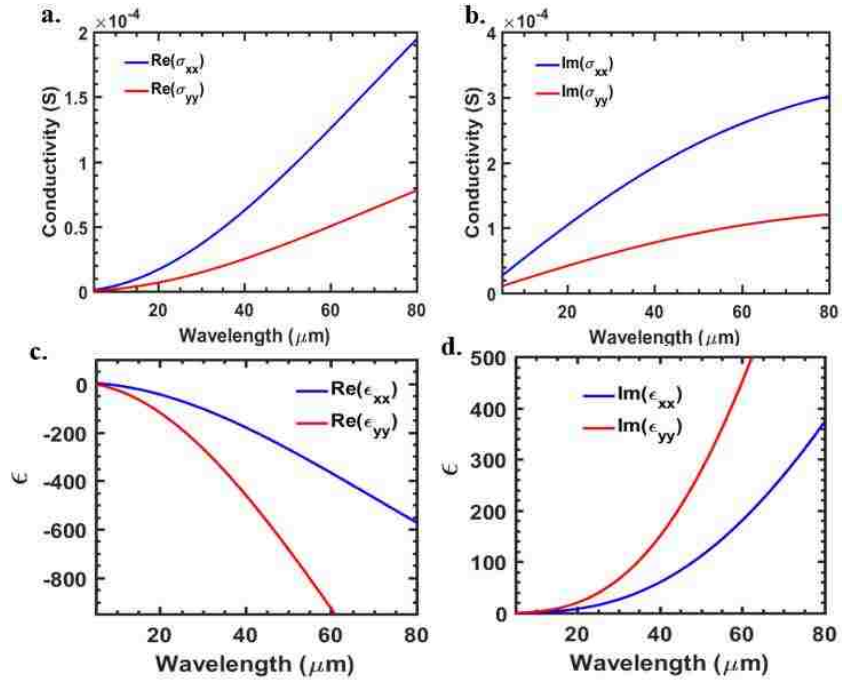## C. 1 Optical conductivity and dielectric constant BP

Figure C. S1. Optical conductivity and dielectric constant of BP for $N = 10^{13}$ cm^{-2} the calculated from Drude model.
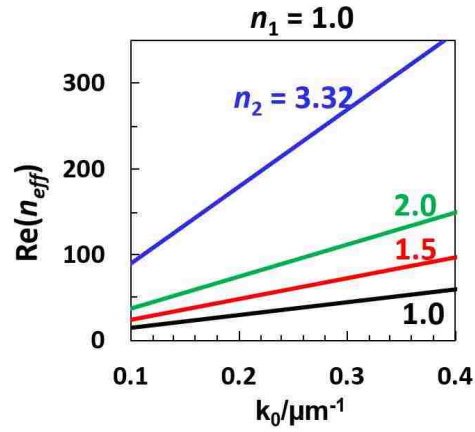

Figure C. S2. Plot of the real part of the SPP modes supported by a BP infinite sheet for four different dielectric media as measured by its vacuum wave vector.

C. 2 Electric field distribution BP ribbon
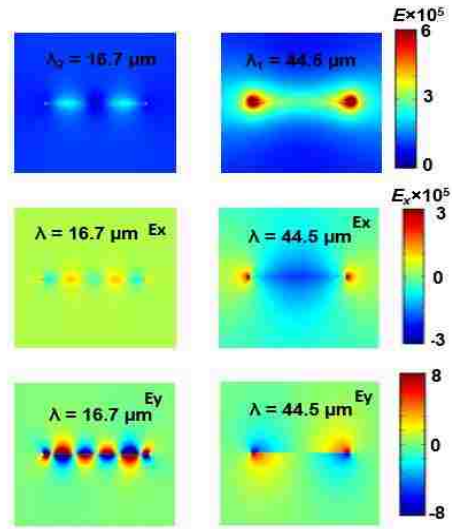
Figure C. S3. Electric field distribution at different direction for $n_1 = 1.0$, n2 = 2.5 of normal-incidence TM mode fundamental mode and higher mode for BP nanoribbons $N = 10^{13}$ cm^{-2} width of ribbon 150 nm and period 250 nm.
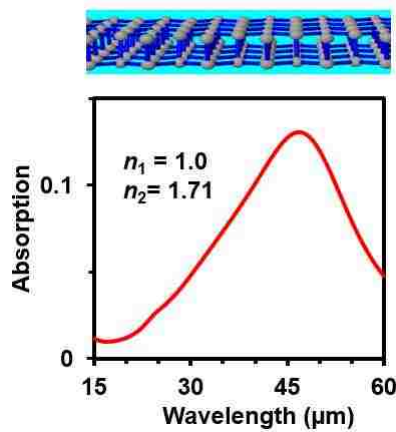
C. 3. Zigzag-direction Ribbon absorption

Figure C. S4. Simulated absorption spectra for normal-incidence TM mode light polarized zigzag directions for different w =150 nm, P = 250 nm, and for $N = 10^{13}$ cm^{-2} .

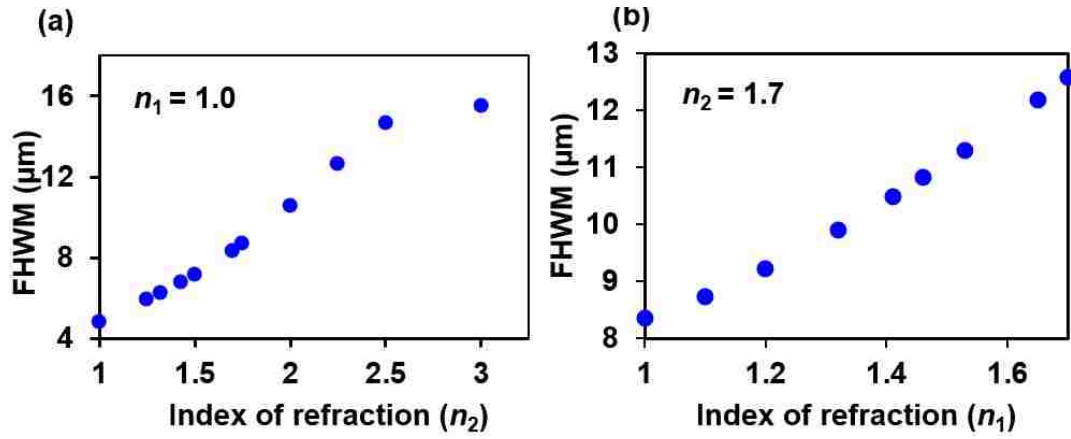## C. 4. FWHM of BP Ribbon broadening

Figure C. S5. Calculated results showing the effects of varying n_2 on the absorption spectrum broadening with n_1 held constant of normal-incidence TM mode. FWHM of fundamental mode ($m = 1$) for BP nanoribbons (a) surrounded by air ($n_1 = 1.0$ and different substrate materials with refractive indices, n_2, and a BP electron density of $N = 10^{13}$ cm^{-2} with respect to the refractive index of the substrate dielectric layer (n_2)(b).

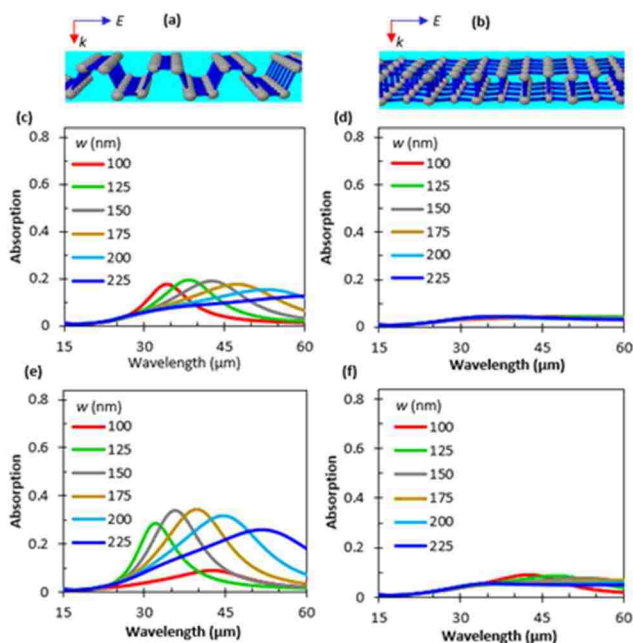## C. 5. BP different ribbon width and number density

Figure C. S6. Comparison of the optical response of light polarized in the (a) armchair and (b) zigzag directions. (c) - (f) Simulated absorption spectra for normal-incidence TM mode light polarized along the armchair and zigzag directions for different w: (c) armchair and (d) zigzag for $N = 5 \times 10^{12}$ cm^{-2}, (e) armchair and (f) zigzag for $N = 7.5 \times 10^{12}$ cm^{-2} . Here, $n_2 = 1.71$, $n_1 = 1.0$, $P = 250$ nm, and w is swept from 100 to 225 nm.

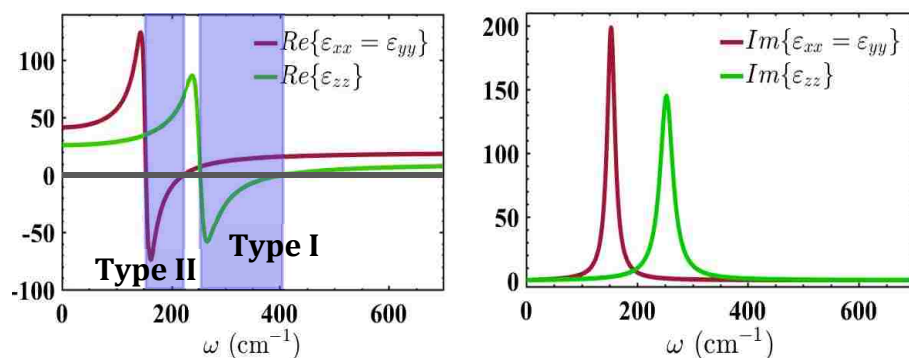## D.1. Dielectric permittivity tensor components of LiNbO₃.

Figure D. S1. (a) Real parts and (b) imaginary part of the dielectric permittivity tensor components of LiNbO3. The red dotted line represents the vertical component, while the blue dash-dotted line is the parallel component. The Type I and II bands region are indicated by shaded area [4,5].
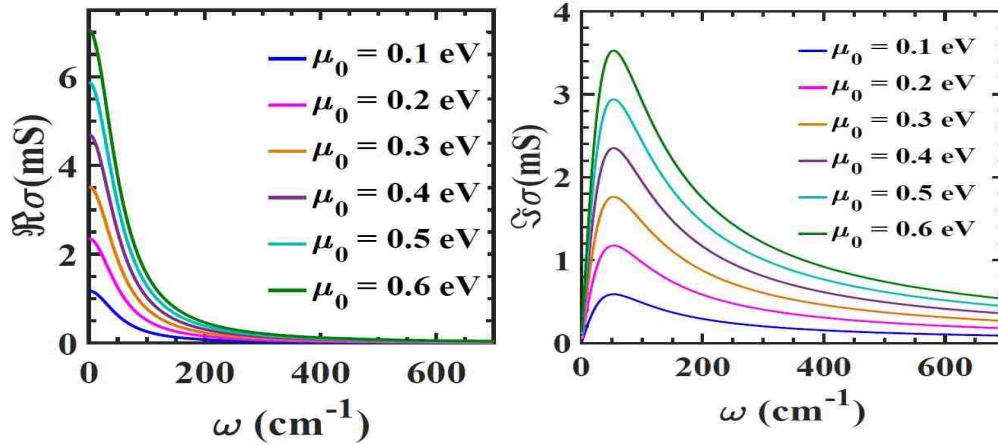
110

D.2. Optical conductivity of graphene:

Figure. D S2. Optical conductivity of graphene sheet from 0.1 eV – 0.6 eV chemical potential real part(a) and imaginary part (b) from Eq (1) showing interband transition gate tunable in THz. Both real and imaginary part value increases with chemical potential vial applied voltage. The intraband contributes more in the higher infrared and higher THz range [6, 7].

Reference

[1] J. D. Jackson, Classical Electrodynamics. New York: Wiley, 2nd edn. (1975).

[2] E. D. Palik, *Handbook of Optical Constants of Solids* (Academic Press, New York, 1985).

[3] D. T. Debu, S. J. Bauman, D. French, Hugh O. H. Churchill, J. B. Herzog, "Tuning Infrared Plasmon Resonance of Black Phosphorene Nanoribbon with a Dielectric Interface", Scientific Reports 8(1), 3224 (2018).

[4] D. Jin, A. Kumar, K.H. Fung, J. Xu, N.X. Fang Appl. "Terahertz plasmonics in ferroelectric-gated graphene", Phys. Lett., 102 (2013), p. 201118.

[5] T. Feurer, N. S. Stoyanov, D. W. Ward, J. C. Vaughan, E. R. Statz, and K. A. Nelson, "Terahertz polaritonics," Annu. Rev. Mater. Res. 37, 317–350 (2007).

[6] Yan, Y. Zhang, P. Kim, and A. Pinczuk, "Electric Field Effect Tuning of Electron-Phonon Coupling in Graphene," Phys. Rev. Lett. **98**(16), 166802 (2007).

[7] M. Liu, X. Yin, E. Ulin-Avila, B. Geng, T. Zentgraf, L. Ju, F. Wang, and X. Zhang, "A graphene-based broadband optical modulator," Nature **474**(7349), 64–67 (2011).

UNIVERSITY OF ARKANSAS

Desalegn Debu <dtdebu@email.uark.edu>

Inquire for Copyright Permission for Dissertation Submission
2 messages

Desalegn Debu <dtdebu@email.uark.edu>   Mon, Jul 23, 2018 at 11:32 AM
To: journalpermissions@springernature.com

Dear Editor,

As copyright rule and requirement of University of Arkansas Dissertation materials, I am writing to request your permission for me to use a published article in Nature Scientific Reports in which I am corresponding author.

I want to use all sections of the article as a chapter and citation of the item to be reproduced in the dissertation as:- D. T. Debu S. J. Bauman, D. French, Hugh O. H. Churchill, and J. B. Herzog, "Tuning Infrared Plasmon Resonance of Black Phosphorene Nanoribbon with a Dielectric Interface", Scientific Reports 8(1), 3224 (2018).

Requester Information:
Name: Desalegn T. Debu (corresponding author)
Affiliation: Department of Physics
           226 Physics Building 825 West Dickson Street
           University of Arkansas Fayetteville, AR 72701
Email: dtdebu@uark.edu

Thank you for your time.

Best Regards,
Desalegn T. Debu

Department of Physics
226 Physics Building 825 West Dickson Street
University of Arkansas Fayetteville, AR 72701
dtdebu@uark.edu

Journalpermissions <journalpermissions@springernature.com>   Tue, Jul 24, 2018 at 3:47 AM
To: Desalegn Debu <dtdebu@email.uark.edu>

Dear Desalegn,

Thank you for your email. This work is licensed under a Creative Commons Attribution 4.0 International License, which permits unrestricted use, distribution, and reproduction in any medium, provided you give appropriate credit to the original author(s) and the source, provide a link to the Creative Commons license, and indicate if changes were made. **You are not required to obtain permission to reuse this article.** The images or other third party material in this article are included in the article's Creative Commons license, unless indicated otherwise in the credit line; if the material is not included under the Creative Commons license, users will need to obtain permission from the license holder to reproduce the material. To view a copy of this license, visit http://creativecommons.org/licenses/by/4.0/.

Best wishes,

Oda

Oda Siqveland

Permissions Assistant

SpringerNature

The Campus, 4 Crinan Street, London N1 9XW,

United Kingdom

T +44 (0) 207 014 6851

http://www.nature.com

http://www.springer.com

UNIVERSITY OF ARKANSAS

Desalegn Debu <dtdebu@email.uark.edu>

Inquire for Copyright Permission for Dissertation Submission
3 messages

Desalegn Debu <dtdebu@email.uark.edu>   Mon, Jul 23, 2018 at 10:53 AM
To: copyright@osa.org

Dear Editor,

As copyright rule and requirement of University of Arkansas Dissertation materials, I am writing to request your permission for me to use a published article in Optics Materials Express in which I am author.

I want to use all sections of the article as a chapter and citation of the item to be reproduced in the dissertation as:- D. T. Debu, P. K. Ghosh, D. French, and J. B. Herzog, "Surface plasmon damping effects due to Ti adhesion layer in individual gold nanodisks," Opt. Mater. Express 7(1), 73–84 (2017).

Requester Information:
Name: Desalegn T. Debu (first author of the requested article)
Affiliation: Department of Physics
           226 Physics Building 825 West Dickson Street
           University of Arkansas Fayetteville, AR 72701
Email: dtdebu@uark.edu

Thank you for your time.

Best Regards,
Desalegn T. Debu

Department of Physics
226 Physics Building 825 West Dickson Street
University of Arkansas Fayetteville, AR 72701
dtdebu@uark.edu

pubscopyright <copyright@osa.org>   Thu, Jul 26, 2018 at 1:50 PM
To: Desalegn Debu <dtdebu@email.uark.edu>, pubscopyright <copyright@osa.org>

Dear Desalegn T. Debu,

Thank you for contacting The Optical Society.

For the use of material from Desalegn T. Debu, Pijush K. Ghosh, David French, and Joseph B. Herzog, "Surface plasmon damping effects due to Ti adhesion layer in individual gold nanodisks," Opt. Mater. Express 7, 73-84 (2017):

As long as the copyrighted material is included within the body, section or chapter, of the thesis, and is not posted separate from the thesis, OSA considers your requested use of its copyrighted materials to be permissible within the author rights granted in the Copyright Transfer Agreement submitted by the requester on acceptance for publication of his/her manuscript. If the entire article is being included, it is requested that the **Author Accepted Manuscript** (or preprint) version be the version included within the thesis and that a complete citation of the original material be included in any publication. This permission assumes that the material was not reproduced from another source when published in the original publication.

The **Author Accepted Manuscript** version is the preprint version of the article that was accepted for publication but not yet prepared and/or formatted by The Optical Society or its vendors.

While your publisher should be able to provide additional guidance, OSA prefers the below citation formats:

For citations in figure captions:

[Reprinted/Adapted] with permission from ref [x], [Publisher]. (with full citation in reference list)

---

pubscopyright <copyright@osa.org>   Thu, Jul 26, 2018 at 1:50 PM
To: Desalegn Debu <dtdebu@email.uark.edu>, pubscopyright <copyright@osa.org>

For images without captions:

Journal Vol. #, first page (year published) An example: Opt. Mater. Express 7, 73 (2017)

Please let me know if you have any questions.

Kind Regards,

Rebecca Robinson

Rebecca Robinson

July 26, 2018

Authorized Agent, The Optical Society